UNIVERSITY
OF MICHIGAN
APR 6 1951
ENGINEERING
LIBRARY

JOURNAL OF THE AERONAUTICAL SCIENCES

VOLUME 18 APRIL, 1951 NUMBER 4

CONTENTS

Supersonic Wing-Body Lift.....GEORGE MORIKAWA 217

The Interaction of Shock Waves with Boundary Layers on a Flat Surface.....F. W. BARRY, A. H. SHAPIRO, AND E. P. NEUMANN 229

On the One-Dimensional Theory of Flame Structure.....RAYMOND FRIEDMAN AND EDWARD BURKE 239

The Laminar Boundary Layer on a Rotating Blade..LAURENCE EUGENE FOGARTY 247

A Flexible Nozzle for a Small Supersonic Wind Tunnel.....SATISH DHAWAN AND ANATOL ROSHKO 253

Sphere Drag Data at Supersonic Speeds and Low Reynolds Numbers..E. D. KANE 259

The Secondary Flow in a Cascade of Airfoils in a Nonuniform Stream.....H. B. SQUIRE AND K. G. WINTER 271

Free and Forced Vibrations of Rotating Blades.....ROBERT PLUNKETT 278

Readers' Forum: "On the Theory of Heat Transfer Through a Laminar Boundary Layer," by Arthur N. Tifford; "Calculation of Deflections in Indeterminate Structures," by H. F. Michielsen; "The Calculation of Deflections of Indeterminate Structures," by Bruno A. Boley and Roland H. Moore; "On Plastic Buckling of Plates and a Theory of Plastic Slip," by P. Cicala; "The Effect of Prandtl Number on the Theoretical Shock-Wave Thickness," by Paul A. Libby.....283–287

Published by the

INSTITUTE OF THE AERONAUTICAL SCIENCES, INC.

JOURNAL OF THE AERONAUTICAL SCIENCES

Editor: HUGH L. DRYDEN, *Director, N.A.C.A.*

Associate Editor: ROBERT R. DEXTER *Managing Editor:* BERNEICE H. JARCK

Editorial Committee

Aerodynamics

Francis Clauser
Howard Emmons
R. Paul Harrington
R. T. Jones
Carl Kaplan
W. B. Klemperer
John G. Lee
H. W. Liepmann
C. C. Lin
H. F. Ludloff
John R. Markham
Clark B. Millikan
Shatswell Ober
W. Bailey Oswald
Allen E. Puckett
Elliott G. Reid
H. J. F. Reid
Russell Robinson
G. B. Schubauer
W. R. Sears
John Stack
Theodore von Kármán
Richard von Mises

Flight Testing

W. K. Ebel
R. R. Gilruth
Melvin N. Gough
Robert Stanley
E. G. Stout

Meteorology

C. F. Brooks
D. M. Little
E. J. Minser
F. W. Reichelderfer
H. C. Willett

Structures and Materials

W. B. Bleakney
E. W. Conlon
J. P. Den Hartog
L. H. Donnell
E. C. Hartmann
N. J. Hoff
E. E. Lundquist
C. F. Nagel, Jr.
J. S. Newell
Alfred S. Niles
W. Ramberg
E. Reissner
F. R. Shanley
H. W. Sibert
C. R. Strang
S. Timoshenko
H. S. Tsien
Chi-Teh Wang

Rotating Wing Aircraft

Robert Coleman
K. H. Hohenemser
Bartram Kelley
Ralph McClarren
R. H. Miller
R. H. Prewitt
Igor I. Sikorsky

Physiologic Problems

H. G. Armstrong
Louis H. Bauer
Eugene Du Bois
W. Randolph Lovelace, II
Ross A. MacFarland
A. D. Tuttle

Flight Propulsion

George W. Brady
Frank W. Caldwell
L. S. Hobbs
E. E. Johnson
Joseph Keenan
R. P. Kroon
Arthur Nutt
Hans Reissner
Abe Silverstein
C. Fayette Taylor
E. S. Taylor
P. Taylor
E. S. Thompson
H. S. Tsien

Aircraft Design

W. E. Beall
W. K. Ebel
Hall L. Hibbard
Richard Hutton
C. L. Johnson
I. M. Laddon
C. J. McCarthy
Fred E. Weick
Robert J. Woods

Air Transport

Charles Froesch
J. A. Herlihy
R. D. Kelly
Otto E. Kirchner
Jerome Lederer
John C. Leslie
R. Dixon Speas

Instruments

Allan G. Binnie
W. G. Brombacher
Charles H. Colvin
B. M. Craig
B. Del Mar
C. S. Draper
O. E. Esval
W. L. Howland
J. E. Lindberg
David W. Moore
George H. Purcell
W. A. Reichel
C. F. Savage
O. Hugo Schuck
C. L. Seward, Jr.
R. Sylvander
D. K. Warner
P. F. Weber

Vibration and Flutter

Lee Arnold
M. A. Biot
William Bollay
Chieh-Chien Chang
Martin Goland
J. P. Den Hartog

Fuels and Oils

D. P. Barnard
J. H. Doolittle
Graham Edgar
R. T. Goodwin
S. D. Heron
A. M. Rothrock

SUBSCRIPTION RATES

JOURNAL OF THE AERONAUTICAL SCIENCES, Published Monthly.—United States and Possessions: 1 Year, $12.00; Single Copies, $1.50. Foreign Countries Including Canada (American Currency Rate): 1 Year, $13.00; Single Copies, $1.50.

AERONAUTICAL ENGINEERING REVIEW, Published Monthly.—United States and Possessions: 1 Year, $3.00; Single Copies, $0.50. Foreign Countries Including Canada (American Currency Rates): 1 Year, $3.50; Single Copies, $0.50.

Notices of change of address should be sent to the Institute at least 30 days prior to actual change of address.

Manuscripts for publication, proofs, and all correspondence should be addressed to the Editorial Office of the JOURNAL.

Correspondence regarding subscriptions may be addressed to Publication Office, 20th and Northampton Sts., Easton, Pa., or to the Editorial Office of the JOURNAL OF THE AERONAUTICAL SCIENCES, 2 East 64th Street, New York 21, New York.

Copyright, 1951, by the Institute of the Aeronautical Sciences, Inc.

Entered as Second Class Matter at the Post Office, Easton, Pa., May 1, 1937. Acceptance for mailing at a special rate of Postage provided for in the Act of August 24, 1912. Authorized April 29, 1937.

JOURNAL OF THE AERONAUTICAL SCIENCES

VOLUME 18 APRIL, 1951 NUMBER 4

Supersonic Wing-Body Lift

GEORGE MORIKAWA*

Hughes Aircraft Company

ABSTRACT

The representation of lift for a fairly general family of wing-body configurations (with no afterbody) in a linearized supersonic flow is considered over the entire range of the parameters. The bracketing limits of lift are obtained simply using the most elementary considerations when the interpretation of these limits is recognized. By the proper choice of the independent parameters and the proper representation of the lift, reasonable approximations for the behavior of lift for intermediate values of the parameters are obtained.

Further generalization to other wing plan forms with straight edges and other body shapes and the representation of other aerodynamic variables such as drag, moment, and center of pressure will be evident but not considered in detail

NOTATION

a	= radius of body
a_t	= ratio of tangent of tip trailing-edge angle ω_1 to tangent of Mach angle μ
A.R.	= aspect-ratio of "exposed wing"
c	= root chord
$C_{L\alpha}$	= lift-curve slope for wing-body combination based on "exposed wing" area
$C_{L\alpha}{}^{(B)}$	= lift-curve slope for body portion of combination based on "exposed wing" area
$C_{L\alpha}{}^{(W)}$	= lift-curve slope for wing portion of combination based on "exposed wing" area
$C_{L\alpha_0}$	= lift-curve slope for "exposed wing" alone
C_p	= pressure coefficient
C_{p_l}	= pressure coefficient along centerline of flat delta wing
$E(\sqrt{1-m^2})$	= complete elliptic integral of second kind
K	= $C_{L\alpha}/C_{L\alpha_0}$, total lift ratio
$K^{(B)}$	= $C_{L\alpha}{}^{(B)}/C_{L\alpha_0}$, body lift ratio
$K^{(W)}$	= $C_{L\alpha}{}^{(W)}/C_{L\alpha_0}$, wing lift ratio
m	= ratio of tangent of leading-edge angle ω_0 to tangent of Mach angle μ
M	= free-stream Mach Number
q	= free-stream dynamic pressure
s	= semispan of wing-body combination measured from body centerline
S_B	= projected area onto plane of wing (x-z plane) upon which body lift acts
S_W	= "exposed wing" area
x	= spanwise coordinate
y	= vertical coordinate normal to plane of wing
z	= chordwise coordinate in free-stream direction coincident with body centerline (cf. Fig. 1)
α	= angle of attack
α_0	= geometrical angle of attack of both body and wing of combination
β	= $\sqrt{M^2-1}$ = ctn μ
λ	= a/s, diameter-span ratio
μ	= Mach angle measured from free-stream direction
ω_0	= leading-edge angle measured from free-stream direction
ω_1	= tip trailing-edge angle measured from free-stream direction (cf. Fig. 1)

Presented at the Aerodynamics Session, Annual Summer Meeting, I.A.S., Los Angeles, July 12–14, 1950.

* Missile Aerodynamics Section, Research and Development Laboratories.

INTRODUCTION

IN THE AERODYNAMIC DESIGN of vehicles for supersonic flight, it is essential that the bracketing limits of the important aerodynamic variables—i.e., lift, drag, moment, and center of pressure—as functions of the design parameters be known. Frequently, an "in the large" analysis of this nature may be initiated using the most elementary considerations with the proper choice of the independent parameters and the proper representation of the aerodynamic variables, and from this study some insight is obtained for the more difficult analysis over the entire range of the parameters. The main consideration in the present paper is the representation of lift for a fairly general family of wing-body configurations in a stationary linearized supersonic flow. Further generalization to other wing plan forms and body shapes and the representation of other aerodynamic variables will be evident but not considered in detail.

The considerations of this paper are a natural and direct consequence of previous related work, notably by Beskin,[1] Lagerstrom and Van Dyke,[2] and Spreiter.[3] Grateful acknowledgment is made of helpful discus-

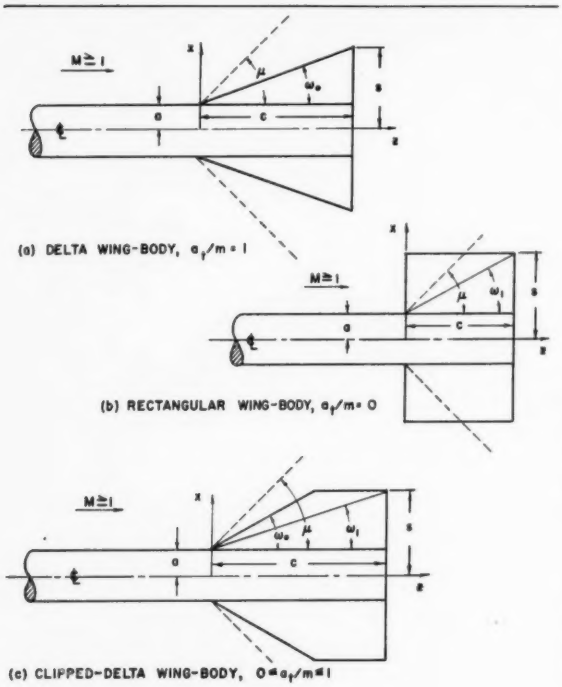

FIGURE 1.
FAMILY OF WING-BODY CONFIGURATIONS WITH NO AFTERBODY

sions with A. E. Puckett, T. F. Coleman, and J. L. Fredrick, of Hughes Aircraft Company; and H. J. Stewart, P. A. Lagerstrom, and C. R. DePrima, of the California Institute of Technology.

Representation of Integrated Values: Lift, Drag, Moment, and Center of Pressure

The principal assumption made in the following discussion, aside from the linearization of the equations of motion, is that the flow field immediately upstream of the wing is cylindrical (independent of the flow direction)—that is, the influence of the nose of the body is assumed to be negligible. In particular, an infinitely long circular cylinder represents the body.[1, 2, 4] Only the lifting problem where both body and wing (flat plate) are at an angle of attack α_0 with respect to the free-stream direction is considered. It is remarked that this problem may be replaced by an equivalent problem[2, 4] where the body angle of attack $\alpha = 0$ and the wing is regarded as twisted with

$$\alpha = \alpha_0[1 + (a^2/x^2)]$$

The coordinates are shown in Fig. 1. The main discussion is confined to an important family of wing plan forms with straight edges and trailing edge normal to the free-stream direction; the body ends at the trailing edge.

Referring to Fig. 1 and using Doris Cohen's notation[5] for wings, the basic parameters for this family of "clipped-delta" wing-body combinations are λ, m, and a_t, where $\lambda \equiv a/s$ is the diameter-span ratio,† m is the ratio of the tangents of the leading edge angle to the Mach angle, and a_t is the ratio of the tangents of the tip trailing-edge angle to the Mach angle. Then

$$m = \tan \omega_0/\tan \mu = \beta \tan \omega_0$$
$$a_t = \tan \omega_1/\tan \mu = \beta \tan \omega_1$$
$$a_t/m = \tan \omega_1/\tan \omega_0$$

where $\beta = \sqrt{M^2 - 1}$. For convenience, the three parameters are taken to be λ, a_t, and a_t/m, where $0 \leq \lambda \leq 1$ and $0 \leq a_t/m \leq 1$. Then, $a_t/m = 1$ defines the particular family of delta wing-body combinations (Fig. 1a), and $a_t/m = 0$ indicates the family of rectangular wing-body combinations (Fig. 1b). Clearly, if the trailing edge is swept (either back or forward), an additional parameter is introduced—namely, the ratio of the tangents of the trailing-edge angle to the Mach angle.

In considering a representation for lift of wing-body configurations, it is reasonable to regard the "exposed wing" as the principal lift-carrying agent and any additional lift (plus or minus) contributed by the body *adjacent* to the wing to be purely supplementary. To regard the "exposed wing" alone as the *basic wing* is the natural consequence of attending to the limiting cases of $\lambda = 0$ and $\lambda = 1$. The boundary conditions on the wing for the wing-body configuration and the "exposed wing" alone are similar—i.e., for $\lambda = 0$ the adjacent body becomes negligible; for $\lambda = 1$, the adjacent body acts as a vertical plane reflector identical to the plane of symmetry of the "exposed wing" alone. Thus, the general point of view is taken that, given the integrated values for wings, the integrated values for wing-body configurations are directly obtainable—exactly for limiting values of the parameters and to good approximation for intermediate cases. A remark is appropriate here concerning Spreiter's representation[3] for lift in the limiting case exhibited by slender body theory, where the basic wing is taken to be a fictitious wing that passes through the body. For a study over the *entire* range of the design parameters, such a representation suppresses and, hence, obscures the behavior of wing-body configurations for values of λ near 1—i.e., for low span-diameter ratio configurations.

Clearly, the preceding discussion holds for the representation of other integrated values such as drag, moment, and center of pressure. In the following section the lift representation for delta wing-body configurations with no afterbody is discussed in detail.

Lift Representation for Delta Wing-Body Configurations

As proposed in the previous section, the lift for the delta wing-body configurations is represented by the

† It should be noted that $\lambda = 0$ defines the *limiting* case of *all* wing and $\lambda = 1$ defines the *limiting* case of *all* body.

ratio of the total lift† of the combination to the lift of the "exposed wing" alone,

$$K = C_{L\alpha}/C_{L\alpha_0} = f(\lambda, m) \tag{1a}$$

a function of the two parameters‡ λ and m. For the basic "exposed wing" alone,

$$\left.\begin{aligned} C_{L\alpha_0} &= \frac{2\pi}{\beta}\frac{m}{E\left(\sqrt{1-m^2}\right)} && (\text{for } 0 \le m \le 1) \\ &= 4/\beta && (\text{for } m \ge 1) \end{aligned}\right\} \tag{1b}$$

where $E\left(\sqrt{1-m^2}\right)$ is the complete elliptic integral of the second kind. It is instructive to separate the total lift $C_{L\alpha}$ into that portion acting on the wing $C_{L\alpha}{}^{(W)}$ and that portion acting on the body $C_{L\alpha}{}^{(B)}$, where

$$C_{L\alpha} = C_{L\alpha}{}^{(W)} + C_{L\alpha}{}^{(B)} \tag{2a}$$

and

$$K = K^{(W)} + K^{(B)} \tag{2b}$$

† To conform to engineering usage, this is expressed as the ratio of lift curve slopes based on the same ("exposed wing") area.

‡ For consistency with the more general clipped-delta wing-body family, the parameter a_t instead of m should be used for the delta wing-body configurations, but m is the more commonly used parameter.

Note that this is an actual experimentally measurable breakdown of lift and generally includes interaction and tip effects. Thus, the wing lift $C_{L\alpha}{}^{(W)}$ generally includes lift due to (A) the angle of attack α_0 of the wing, (B) the upwash $\alpha_0(a^2/x^2)$ of the body upstream of the wing, (C) the reflection off the body and the plane of symmetry (the y-z plane) of the disturbances due to (A) and (B), and (D) the reflection of wing tip disturbances.

The lift for limiting values of the parameter m may be obtained simply when the interpretation of these limits is recognized: (A) $m = 0$ *implies* either that the free-stream Mach Number $M = 1$ ($\omega_0 \neq \pi/2$) or the leading-edge angle $\omega_0 = 0$ ($M \neq \infty$); this is clearly the limiting case of "slender body theory." (B) $m = \infty$ *implies* either that $M = \infty$ ($\omega_0 \neq 0$) or $\omega_0 = \pi/2$ ($M \neq 1$); this is the limiting case** of "strip theory." In both limiting cases, the analysis is simplified by the reduction of the original three-dimensional problem to two dimensions. From Spreiter's results[3] and some elementary integration and algebraic manipulations, the results may be tabulated, letting $a/s \equiv \lambda$ for convenience.

** Note that the body carries no lift for $m = \infty$ (e.g., for fixed λ, the chord approaches zero as ω_0 approaches $\pi/2$); and

$$K = K^{(W)} = (1/S_W)\iint_{S_W}(\alpha/\alpha_0)\,dS$$

(1) *Limiting Total Lift*

$$m = 0: \quad K = (1+\lambda)^2 \tag{3a}$$

$$m = \infty: \quad K = [1/(1-\lambda)^2][(1-\lambda^2) + 2\lambda^2 \ln \lambda] \tag{3b}$$

(2) *Limiting Wing Lift*

$$m = 0: \quad K^{(W)} = \frac{2}{(1-\lambda)^2}\left[\frac{1}{\pi}(1+\lambda^2)^2 \sin^{-1}\left(\frac{1}{\sqrt{1+\lambda^2}}\right) - \frac{\lambda}{\pi}(1-\lambda^2) - \lambda^2\right] \tag{4a}$$

$$m = \infty: \quad K^{(W)} = [1/(1-\lambda)^2][1-\lambda^2) + 2\lambda^2 \ln \lambda] \equiv K \tag{4b}$$

(3) *Limiting Body Lift*

$$m = 0: \quad K^{(B)} = \frac{2}{\pi(1-\lambda)^2}\left[(1+\lambda^4)\sin^{-1}\left(\frac{\lambda}{\sqrt{1+\lambda^2}}\right) - 2\lambda^2 \sin^{-1}\left(\frac{1}{\sqrt{1+\lambda^2}}\right) + \lambda(1-\lambda^2)\right] \tag{5a}$$

$$m = \infty: \quad K^{(B)} \equiv 0 \tag{5b}$$

The lift for $m = \infty$ can also be obtained directly from reference 2 for this configuration. Eqs. (3), (4), and (5) are plotted in Fig. 2.

Some preliminary observations of interest may now be made. (A) The total lift $K(\lambda, m)$ for the limiting cases of $m = 0$ and $m = \infty$ and also the slope $\partial K(\lambda, m) \div \partial\lambda$ are identical at $\lambda = 0$—i.e.,

$$K(0, 0) = K(0, \infty) = 1 \tag{6a}$$

and

$$\partial K(0, 0)/\partial\lambda = \partial K(0, \infty)/\partial\lambda = 2 \tag{6b}$$

and the difference between $K(\lambda, 0)$ and $K(\lambda, \infty)$ increases monotonically with λ to a maximum at $\lambda = 1$, at which

$$K(1, 0) - K(1, \infty) = 2 \tag{7a}$$

The slopes at $\lambda = 1$ are

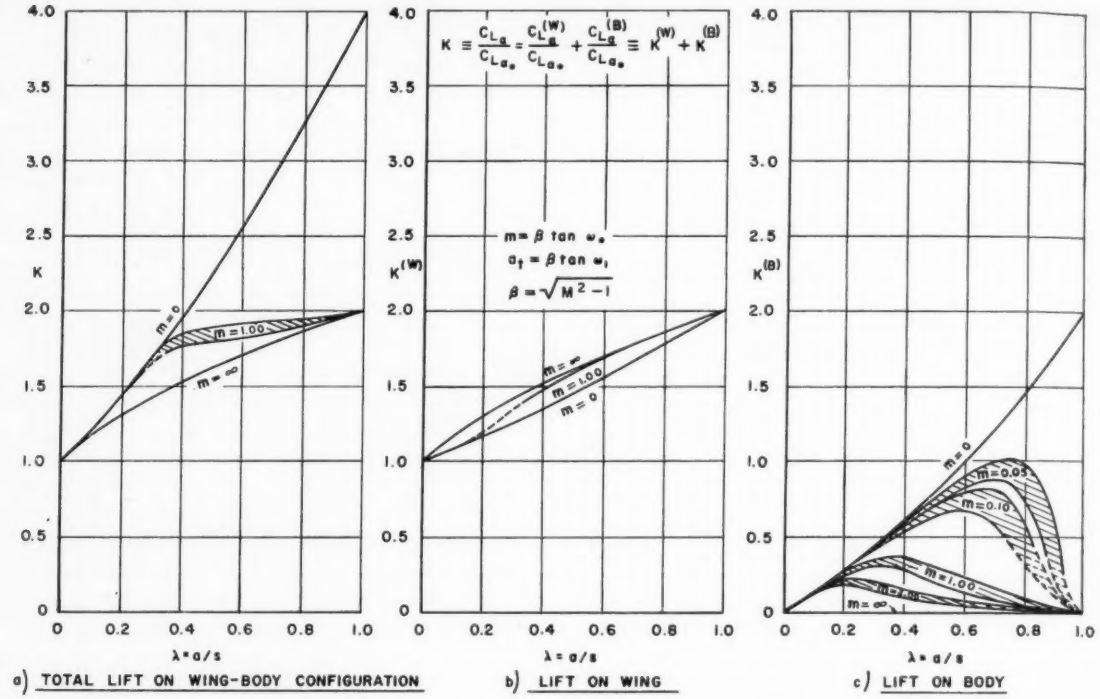

FIGURE 2. DELTA WING-BODY LIFT WITH NO AFTERBODY, $a_1/m = 1.0$

$$\partial K(1, 0)/\partial\lambda = 4 \tag{7b}$$

and

$$\partial K(1, \infty)/\partial\lambda = 2/3 \tag{7c}$$

(B) The difference between the wing lift $K^{(W)}(\lambda, 0)$ and $K^{(W)}(\lambda, \infty)$ for the limiting values of m is small—i.e.,

$$[K^{(W)}(\lambda, \infty) - K^{(W)}(\lambda, 0)] < 0.15K^{(W)}(\lambda, 0) \tag{8a}$$

for all λ and is zero at $\lambda = 0$ and $\lambda = 1$,

$$[K^{(W)}(0, \infty) - K^{(W)}(0, 0)] =$$

$$[K^{(W)}(1, \infty) - K^{(W)}(1, 0)] = 0 \tag{8b}$$

The slopes for $\lambda = 0$ and $\lambda = 1$ are

$$\partial K^{(W)}(0, 0)/\partial\lambda = 2[1 - (2/\pi)] \tag{9a}$$

$$\partial K^{(W)}(0, \infty)/\partial\lambda = 2 \tag{9b}$$

and

$$\partial K^{(W)}(1, 0)/\partial\lambda = 2[1 - (4/3\pi)] \tag{10a}$$

$$\partial K^{(W)}(1, \infty)/\partial\lambda = 2/3 \tag{10b}$$

(C) The body lifts $K^{(B)}(\lambda, m)$ for $m = 0$ and $m = \infty$ are both zero at $\lambda = 0$,

$$K^{(B)}(0, 0) = K^{(B)}(0, \infty) = 0 \tag{11a}$$

the slopes being

$$\partial K^{(B)}(0, 0)/\partial\lambda = 4/\pi \tag{11b}$$

$$\partial K^{(B)}(0, \infty)/\partial\lambda = 0 \tag{11c}$$

and the difference $[K^{(B)}(\lambda, 0) - K^{(B)}(\lambda, \infty)]$ increases monotonically with λ to a maximum at $\lambda = 1$, at which

$$[K^{(B)}(1, 0) - K^{(B)}(1, \infty)] = 2 \tag{12a}$$

The slopes at $\lambda = 1$ are

$$\partial K^{(B)}(1, 0)/\partial\lambda = 2[1 + (4/3\pi)] \tag{12b}$$

$$\partial K^{(B)}(1, \infty)/\partial\lambda = 0 \tag{12c}$$

Thus, it is clear that the large difference between the total lifts, $[K(\lambda, 0) - K(\lambda, \infty)]$, for small span-diameter ratio configurations—i.e., λ near 1—is due primarily to the large differences between the body lifts $[K^{(B)}(\lambda, 0) - K^{(B)}(\lambda, \infty)]$. Initially then, it appears imperative to obtain at least approximate expressions for body lift for intermediate values of m, $0 < m < \infty$.

Approximate Body Lift for $0 < m < \infty$

From previous studies of pressure distributions and lift[2, 4, 7] on wing-body configurations for intermediate supersonic Mach Numbers, it is evident that exact calculations are, at the very least, difficult and probably impractical. Even the approximate calculation of local pressures for $m \geq 1$ (supersonic leading edge) is tedious, the difficulties becoming more apparent on the body and more so for $0 < m < 1$ (subsonic leading edge). However, for $m \geq 1$, the calculations made in reference 4 for the zero leading-edge sweepback case and later unpublished calculations for $m = 1$ and $\sqrt{3}$ indicate that a reasonable approximation for the pres-

sure *on the body* (not influenced by the wing tip) is the asymptotic pressure at a large distance downstream from the leading edge; this approximation as an average value on the body appears reasonable even near the leading edge. The asymptotic pressure is identically the centerline pressure on the corresponding "exposed wing" alone,

$$\frac{C_{p_0}}{\alpha_0} = \frac{4}{\pi}\frac{1}{\beta}\frac{m}{\sqrt{m^2-1}}\sec^{-1} m \tag{13}$$

on the lower surface.

First Approximation for $m \geq 1$.—Assume that the pressure on the body is *constant* (for fixed M and m) and given by Eq. (13). Then,

$$\left.\begin{aligned} C_{L_\alpha}{}^{(B)} &= \frac{2}{S_W}\int\int_{S_B}\left(\frac{C_p}{\alpha_0}\right)dS \\ &= 2(C_{p_0}/\alpha_0)(S_B/S_W) \end{aligned}\right\} \tag{14a}$$

where the integration is performed over an area S_B, which is projected onto the x-z plane, and S_W is the "exposed wing" area. The body area S_B is bounded by (A) the projection onto the plane of the wing of the helices (lead angle equal to the Mach angle) emanating from the leading-edge-body junction, (B) the root chord, c, and (C) the base. For

$$\left.\begin{aligned} &0 \leq \frac{c}{a} \leq \frac{\pi}{2}\beta \quad \text{or} \quad \lambda \equiv \frac{a}{s} \geq \frac{1}{1+(\pi/2)m} \\ &S_B/a^2 = 2\int_0^c \left[1-\cos\left(\frac{z}{\beta a}\right)\right]\frac{dz}{a} \\ &\quad = 2\beta\left[\left(\frac{1-\lambda}{m\lambda}\right) - \sin\left(\frac{1-\lambda}{m\lambda}\right)\right] \end{aligned}\right\} \tag{14b}$$

Since

$$c/a = \beta[(1-\lambda)/m\lambda]$$

and the "exposed wing" area

$$S_W/a^2 = \frac{c}{a}\left(\frac{1-\lambda}{\lambda}\right) = \frac{\beta}{m}\left(\frac{1-\lambda}{\lambda}\right)^2 \tag{14c}$$

then the body lift

$$K^{(B)} = \frac{4}{\pi}\frac{m}{\sqrt{m^2-1}}\sec^{-1} m\left(\frac{\lambda}{1-\lambda}\right)\times \left[1-\left(\frac{m\lambda}{1-\lambda}\right)\cdot\sin\left(\frac{1-\lambda}{m\lambda}\right)\right] \tag{14d}$$

for $m \geq 1$ and $\lambda \geq 1/[1+(\pi/2)m]$.

Similarly, for $c/a \geq (\pi/2)\beta$ or $0 \leq \lambda \leq 1/[1+(\pi/2)m]$,

$$S_B/a^2 = 2\beta\{[(1-\lambda)/m\lambda] - 1\} \tag{14e}$$

and the body lift

$$K^{(B)} = \frac{4}{\pi}\frac{m}{\sqrt{m^2-1}}\sec^{-1} m\left(\frac{\lambda}{1-\lambda}\right)\times \left[1-\left(\frac{m\lambda}{1-\lambda}\right)\right] \tag{14f}$$

The curves represented by Eqs. (14d) and (14f) are shown in Fig. 2c for $m = 1$ and $m = 2$ and define the *lower* bound of the cross-hatched areas in the figure for these particular values of m. The slopes obtained from Eqs. (14d) and (14f) for $\lambda = 0$ and $\lambda = 1$ are

$$\frac{\partial K^{(B)}(0,\, m)}{\partial\lambda} = \frac{4}{\pi}\frac{m}{\sqrt{m^2-1}}\sec^{-1} m \qquad (\text{for } 1 \leq m < \infty) \tag{15a}$$

and

$$\frac{\partial K^{(B)}(1,\, m)}{\partial\lambda} = -\frac{2}{3\pi}\frac{1}{m\sqrt{m^2-1}}\sec^{-1} m \qquad (\text{for } 1 \leq m \leq \infty) \tag{15b}$$

Note from Eq. (15a) that, for $\lambda = 0$ and $m = 1$, the slope is $4/\pi$, which is identical to that for $m = 0$ given by Eq. (11b), but the slope increases with m. Thus, in a small region near $\lambda = 0$, $K^{(B)}(\lambda, m)$ for $1 < m < \infty$ lies slightly outside the region bounded by $m = 0$ and $m = \infty$ in Fig. 2c; this is attributable to the approximation used. In order to have some measure for estimating the possible deviation of this approximation, a second approximation that overestimates the body lift, at least for $1/[1+(\pi/2)m] \leq \lambda \leq 1$ [or $0 \leq c/a \leq (\pi/2)\beta$] is given.

Second Approximation for $m \geq 1$.—Assume that the average pressure on the body varies linearly from $(C_{p_0} \div \alpha_0)$ at the leading-edge-body junction to $(1/2)(C_{p_0} \div \alpha_0)$ at a distance $(\pi/2)\beta a$ downstream and is constant $(1/2)(C_{p_0}/\alpha_0)$ over the remainder of the body [cf. Eq. (13)]. Then,

$$\left(\frac{C_p}{\alpha_0}\right) = 2\left(\frac{C_{p_0}}{\alpha_0}\right)\left(1-\frac{z}{\pi\beta a}\right) \qquad \left(\text{for } 0 \leq \frac{z}{a} \leq \frac{\pi}{2}\beta\right) \tag{16}$$

$$C_{L_\alpha}{}^{(B)} = (2/S_W)\int\int_{S_B}(C_p/\alpha_0)\,dS$$

and for $0 \leq c/a \leq (\pi/2)\beta$ $\left\{\text{or } \frac{1}{[1+(\pi/2)m]} \leq \lambda \leq 1\right\}$,

$$C_{L_\alpha}{}^{(B)}/a^2 = \frac{4}{S_W}\left(\frac{C_{p_0}}{\alpha_0}\right)\int_0^c\left(1-\cos\frac{z}{\beta a}\right)\left(1-\frac{z}{\pi\beta a}\right)\frac{dz}{a} \tag{17a}$$

and

$$K^{(B)} = \frac{8}{\pi}\frac{m^2}{\sqrt{m^2-1}}\sec^{-1} m\left(\frac{\lambda}{1-\lambda}\right)^2\left\{\left(\frac{1-\lambda}{m\lambda}\right)\left[1-\frac{1}{2\pi}\left(\frac{1-\lambda}{m\lambda}\right)\right]-\left[1-\frac{1}{\pi}\left(\frac{1-\lambda}{m\lambda}\right)\right]\sin\left(\frac{1-\lambda}{m\lambda}\right)+\frac{1}{\pi}\cos\left(\frac{1-\lambda}{m\lambda}\right)-\frac{1}{\pi}\right\} \quad (17b)$$

and for $c/a \geq (\pi/2)\beta$ {or $0 \leq \lambda \leq 1/[1+(\pi/2)m]$},

$$K^{(B)} = \frac{8}{\pi}\frac{m^2}{\sqrt{m^2-1}}\sec^{-1} m\left(\frac{\lambda}{1-\lambda}\right)^2\left\{\left(\frac{1-\lambda}{2m\lambda}\right)+\frac{\pi}{8}-\frac{1}{2}-\frac{1}{\pi}\right\} \quad (17c)$$

The curves represented by Eqs. (17b) and (17c) are shown in Fig. 2c for $m = 1$ and $m = 2$ and define the *upper* bound of the cross-hatched areas for these particular values of m. The slopes obtained from Eqs. (17b) and (17c) for $\lambda = 0$ and $\lambda = 1$ are

$$\frac{\partial K^{(B)}(0, m)}{\partial\lambda} = \frac{4}{\pi}\frac{m}{\sqrt{m^2-1}}\sec^{-1} m \quad (\text{for } 1 \leq m < \infty) \quad (18a)$$

which is identical to that obtained by the first approximation [cf., Eq. (15a)], and

$$\frac{\partial K^{(B)}(1, m)}{\partial\lambda} = -\frac{4}{3\pi}\frac{1}{m\sqrt{m^2-1}}\sec^{-1} m \quad (\text{for } 1 \leq m \leq \infty) \quad (18b)$$

which is twice the slope obtained by the first approximation [cf. Eq. (15b)].

Reasonable approximations for the subsonic leading-edge case $0 < m < 1$ are difficult to obtain. However, for m near zero—i.e., either M near 1 or ω_0 near 0—one expects[8] the spanwise pressure distribution over the body to resemble that for $m = 0$ except near the helical boundary—i.e., near the leading-edge-body junction. It appears reasonable then to assume that for *m near zero* the chordwise distribution of pressure may be represented by that for $m = 0$ but with a prescribed linear shift downstream to indicate the formation of the zero pressure region between the x-y plane (the crossflow-plane at $z = 0$) and the helical boundary.

First Approximation for $0 \leq m < 1$.—Assume that the linear shift is of length $(\pi/2)\beta$. Then the body lift $C_{L_\alpha}{}^{(B)}$ may be obtained immediately from the slender body theory result for $m = 0$ by replacing s/a for $m = 0$ by $s_0/a = s/a - (\pi/2)m$ for $0 \leq m < 1$ or

$$\lambda_0 = \frac{\lambda}{1-(\pi/2)m\lambda}, \quad \left[\text{for } 0 \leq m < 1 \text{ and } \lambda < \frac{1}{1+(\pi/2)m}\right] \quad (19a)$$

Note that this approximation is not valid for the chord length

$$\frac{c}{a} < \frac{\pi}{2}\beta \quad \left(\text{or } \lambda > \frac{1}{1+(\pi/2)m}\right)$$

in fact, the approximation states that the body lift is zero for $0 \leq c/a \leq (\pi/2)\beta$. Then, with λ_0 given by Eq. (19a),

$$K^{(B)} = E\left(\sqrt{1-m^2}\right)\left(\frac{\lambda}{\lambda_0}\right)^2\left(\frac{1}{1-\lambda}\right)^2 \times \left[\frac{2}{\pi}(1+\lambda_0{}^4)\sin^{-1}\left(\frac{\lambda_0}{\sqrt{1+\lambda_0{}^2}}\right)-\frac{4\lambda_0{}^2}{\pi}\sin^{-1}\left(\frac{1}{\sqrt{1+\lambda_0{}^2}}\right)+\frac{2}{\pi}\lambda_0(1-\lambda_0{}^2)\right] \quad \left[\text{for } \lambda < \frac{1}{1+(\pi/2)m}\right] \quad (20)$$

The curves represented by Eqs. (19a) and (20) are shown in Fig. 2c for $m = 0.05$ and 0.10 and define the *lower* bound of the cross-hatched areas in the figure for these particular values of m.

Second Approximation for $0 \leq m < 1$.—A second approximation may reasonably be that the linear shift is less than that defined by Eq. (19a) but is a mean distance given by $s_0/a = [(s/a) - m]$ or

$$\lambda_0 = \lambda/(1-m\lambda) \quad (19b)$$

Then the body lift $K^{(B)}$ is given by Eqs. (19b) and (20) for $\lambda < 1/(1+m)$. The curves represented by these equations are shown in Fig. 2c for $m = 0.05$ and 0.10 and define the *upper* bound of the cross-hatched areas for the corresponding values of m. It is noted that for both approximations a definite maximum is found and that this family of curves for $0 \leq m < 1$ resembles the family of curves for $m \geq 1$; the curves for $0 < m < 1$ were propitiously faired to $K^{(B)}(1, m) = 0$ over the small region where Eq. (20) is invalid at and near $\lambda = 1$.

With the approximate representation of the body lift $K^{(B)}$, there remains the representation of wing lift

$K^{(W)}$ for $0 < m < \infty$ before the total lift K for all values of m can be discussed.

(5) *Approximate Wing Lift for* $0 < m < \infty$

Meaningful approximations for the wing lift are difficult to obtain since the difference $[K^{(W)}(\lambda, \infty) - K^{(W)}(\lambda, 0)]$ is uniformly small for all λ, $0 \leq \lambda \leq 1$. However, graphical integrations of the pressure distribution (unpublished) on the wing calculated by the methods of reference 4 yield the curve shown in Fig. 2b for $m = 1$, $\lambda \geq 1/(1 + \pi m)$. Calculations for $m = \sqrt{3}$ give a nearly identical curve.

Some additional observations may be made of the variation of $\partial K^{(W)}/\partial\lambda$ with m at the end points $\lambda = 0$ and $\lambda = 1$. At $\lambda = 1$—i.e., at the limiting case of all body—the effective angle of attack of the wing with the equivalent twist due to body upwash is linear,

$$\alpha/\alpha_0 = 2[2 - (x/a)], \quad [(x/a) - 1] \ll 1 \qquad (21)$$

and the body acts as a vertical plane reflector.† For the supersonic leading edge case $m \geq 1$, the wing lift is simply obtained by Lagerstrom's theorem[2] on the preservation of lift, which has also been given independently by Ward:[6]

$$C_L{}^{(W)} = \frac{4}{\beta}\alpha_{\text{aver.}} = \frac{4}{\beta}\frac{1}{S_W}\int\int_{S_W} \alpha \, dS$$

Then,

$$K^{(W)} = 2\{1 - [(1 - \lambda)/3\lambda]\} \qquad (22a)$$

and

$$\partial K^{(W)}(1, m)/\partial\lambda = 2/3 \qquad (22b)$$

which is identically that for $m = \infty$ [cf. Eq. (10b)]. Thus, for $m \geq 1$, the slope at $\lambda = 1$ is independent of m.

The slope at $\lambda = 1$ for the subsonic leading-edge case $0 \leq m \leq 1$ may be obtained by a somewhat lengthier calculation. However, an approximate calculation of the wing lift slope $\partial K^{(W)}(1, m)/\partial\lambda$ is made using Martha Graham's modified strip method[9] and assuming the twist distribution to be linear [exact at $\lambda = 1$, cf. Eq. (21)]. Then, by a simple integration for λ near 1,

$$K^{(W)}(\lambda, m) = 2\left[1 - \frac{2}{3\pi}\frac{E\left(\sqrt{1 - m^2}\right)}{\sqrt{m}}\left(\frac{1 - \lambda}{\lambda}\right)\right] \qquad (23a)$$

and, at $\lambda = 1$,

$$\partial K^{(W)}(1, m)/\partial\lambda = (4/3\pi)\left[E\left(\sqrt{1 - m^2}\right)/\sqrt{m}\right] \qquad (23b)$$

The strip approximation is exact for $m = 1$ and is invalid at $m = 0$. Fig. 3 shows the variation of the wing lift slope given by Eq. (23b) at $\lambda = 1$; the dashed portion is the interpolation of the expected exact curve to the correct value for $m = 0$ [cf. Eq. (10a)].

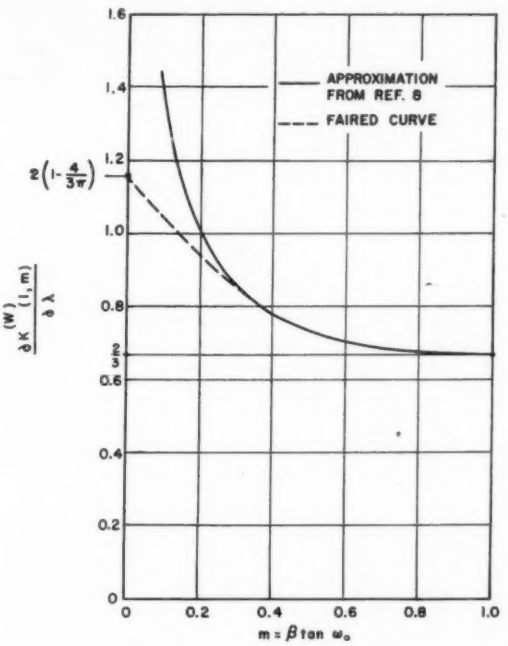

FIGURE 3. WING LIFT SLOPE WITH RESPECT TO λ FOR DELTA WING-BODY AT $\lambda = 1$

At $\lambda = 0$, the wing lift slope $\partial K^{(W)}(0, 1)/\partial\lambda$ may be obtained for the sonic leading-edge case $m = 1$. Assuming that the total lift slope $\partial K(0, m)/\partial\lambda$ is independent of m—i.e., identical to that for $m = 0$ and $m = \infty$ (cf. Eq. (6b)]—and, since the body lift slope

$$\partial K^{(B)}(0, 1)/\partial\lambda = \partial K^{(B)}(0, 0)/\partial\lambda$$

the wing lift slope for $\lambda = 0$, $m = 1$ is necessary identical to the wing slope for $\lambda = 0$, $m = 0$ given by Eq. (9a). This implies that for $\lambda = 0$, $0 \leq m \leq 1$ (subsonic leading edge) the wing lift slope is independent of m. Now with these approximate representations of wing and body lifts for intermediate values of m, $0 < m < \infty$, a basis has been established for representing the total lift for all λ, $0 \leq \lambda \leq 1$ and all m, $0 \leq m \leq \infty$. The calculations indicate that (A) all the total lift curves lie in the region bounded by the total lift curves for $m = 0$ and $m = \infty$; (B) the total lift $K(0, m) = 1$, independent of m; and (C) the total lift $K(1, m) = 2$ at $\lambda = 1$ for $0 < m \leq \infty$. The observation that there does not exist continuous dependence of the lift on the parameters—i.e., dependence of body lift on m at $\lambda = 1$—is not startling, since for $m = 0$ the wave equation is reduced [since the coefficient $(M^2 - 1)$ of the second derivative with respect to the flow direction is zero] to the two-dimensional Laplace's equation. Sometimes this is called, mathematically

† Actually, this last condition is sufficient and implies that, for any $m \geq 1$, the lift $K^{(W)}$ and lift slope $\partial K^{(W)}/\partial\lambda$ at $\lambda = 1$ is precisely that for $m = \infty$.

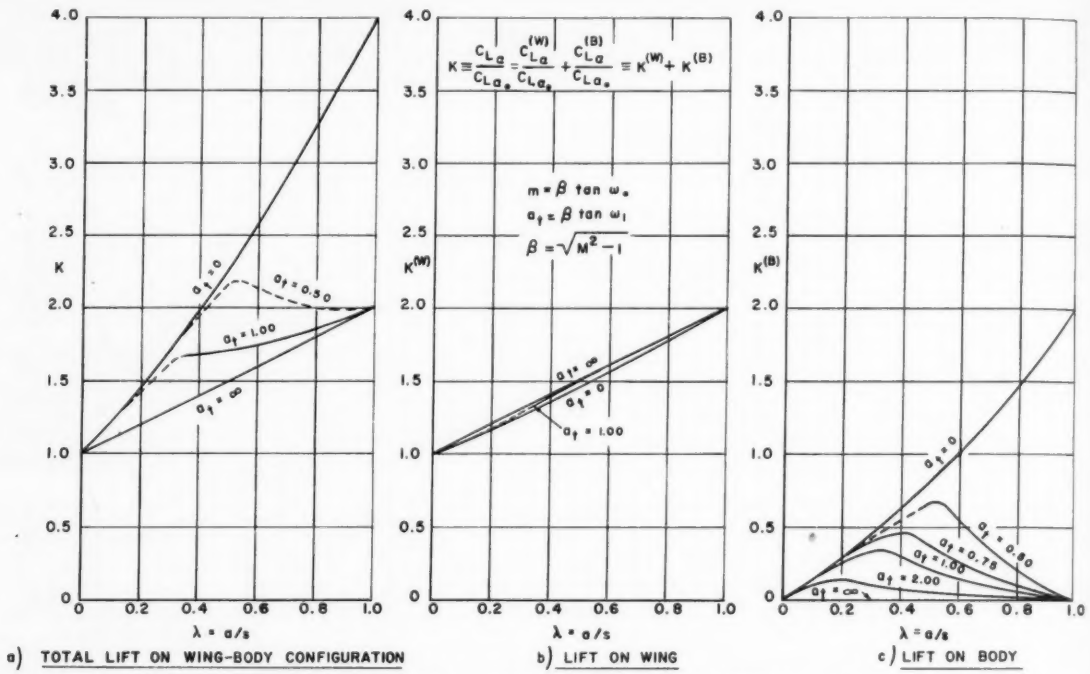

FIGURE 4. RECTANGULAR WING-BODY LIFT WITH NO AFTERBODY, $a_t/m = 0$

speaking, the boundary-layer phenomenon, stretching the concepts a little.

(6) *Remarks on the Analysis*

Evidently in the foregoing analysis, two underlying assumptions are made concerning the behavior of the lift: (A) the lift for all finite m is bounded by the lift for $m = 0$ and $m = \infty$—i.e., all the lift curves lie between the lift curves for $m = 0$ and $m = \infty$—and (B) for fixed λ the variation of lift is monotonic in m. Mathematical verification appears difficult, but there exist strong physical justifications for this behavior. The principal justification, as in many physical problems, seems to lie in experiment.

Lift Representation for Rectangular Wing-Body Configurations

The lift representation for the family of rectangular wing-body configurations with no afterbody may be carried out in a similar fashion to that for the delta wing-body configurations. The two parameters for this case are λ and a_t. The parameter a_t is proportional to the effective aspect ratio[2] of the "exposed wing,"

$$a_t = \frac{\beta \text{A.R.}}{2} = \frac{\beta}{c/a}\left(\frac{1-\lambda}{\lambda}\right) \tag{24}$$

Again, the lifts for the limiting cases of the parameter a_t are easily obtained, since (A) $a_t = 0$ *implies* either $M = 1$ ($\omega_1 \neq \pi/2$) or $\omega_1 = 0$ (this is the case given by slender body theory), and (B) $a_t = \infty$ *implies* either $M = \infty$ or $\omega_1 = \pi/2$ (this is the case given by "strip theory"). Then the lifts for $a_t = 0$ are precisely those given for the delta wing-body configurations for $m = 0$—i.e., given by Eqs. (3a), (4a), and (5a). The lift for $a_t = \infty$ obtained by a simple integration is

$$K = K^{(W)} = (1 + \lambda) \tag{25a}$$

and

$$K^{(B)} = 0 \tag{25b}$$

The total wing and body limiting lifts for $a_t = 0$ and $a_t = \infty$ are shown in Figs. 4a, 4b, and 4c, respectively. The limiting body lifts are identical to those for the delta wing-body configuration, the most evident departure being in Fig. 4b for wing lift; the difference between the limiting wing lifts is uniformly smaller than for the delta case,

$$[K^{(W)}(\lambda, \infty) - K^{(W)}(\lambda, 0)] < 0.05K^{(W)}(\lambda, 0) \tag{26}$$

Hence, just as in the delta case, it is of first importance to obtain approximate representations of the body lift for intermediate values of a_t. Beforehand, it is noted that there are distinct intermediate values of a_t characterized for example by the number of tip leading-edge reflections off the body; for decreasing a_t, the first of these is $a_t = 1$ (the tip Mach element intersects the trailing-edge-body junction), there being an infinite number in a decreasing sequence—i.e., $a_t = 1, 1/2, 1/3, \ldots$. In contrast, there is only one distinct intermediate $a_t(=m)$ for the delta case—namely, $a_t = 1$ (sonic leading edge).

(I) Approximate Body Lift for $0 < a_t < \infty$

For $a_t \geq 1$, assuming as in the *first approximation* for body lift in the delta case that the pressure on the body is constant (equal to the asymptotic value far downstream), the body lifts corresponding to Eqs. (14d) and (14f) are

$$K^{(B)} = \frac{1}{\left(1 - \frac{1}{4a_t}\right)} \left(\frac{\lambda}{1-\lambda}\right) \left[1 - \left(\frac{a_t\lambda}{1-\lambda}\right) \sin\left(\frac{1-\lambda}{a_t\lambda}\right)\right] \quad \left[\text{for } \lambda \geq \frac{1}{1 + (\pi/2)a_t}\right] \tag{27a}$$

and

$$K^{(B)} = \frac{1}{\left(1 - \frac{1}{4a_t}\right)} \left(\frac{\lambda}{1-\lambda}\right) \left[1 - \left(\frac{a_t\lambda}{1-\lambda}\right)\right] \quad \left[\text{for } \lambda \leq \frac{1}{1 + (\pi/2)a_t}\right] \tag{27b}$$

where

$$C_{L_{\alpha_0}} = (4/\beta)[1 - (1/4a_t)] \tag{27c}$$

Fig. 4c shows that the shapes of the curves defined by Eqs. (27a) and (27b) for $a_t = 1$ and 2 are similar to the corresponding curves for the delta case (cf. Fig. 2c). The body lift slopes at $\lambda = 0$ and $\lambda = 1$ are

$$\frac{\partial K^{(B)}(0, a_t)}{\partial \lambda} = \frac{1}{[1 - (1/4a_t)]} \quad (\text{for } a_t \geq 1) \tag{28a}$$

and

$$\frac{\partial K^{(B)}(1, a_t)}{\partial \lambda} = -\frac{1}{2a_t[a_t - (1/4)]} \quad (\text{for } a_t \geq 1) \tag{28b}$$

Foregoing the second approximation for $a_t \geq 1$ because the result is clear (cf. Fig. 2c), an approximation for body lift for $1/2 \leq a_t \leq 1$ is given assuming constant pressure on the body upstream of the boundary defined by the region of influence on the body of the tip leading edge and zero pressure downstream of this boundary. Fig. 5 shows the shape of the projection on the x-z plane of this boundary for $0 \leq \lambda \leq 1$; the boundary projection is given by

$$\frac{x}{a} = \frac{1}{2\lambda}\left[1 + \lambda^2\left(1 - \frac{z^2}{\beta^2 a^2}\right)\right], \quad \left[\text{for}\left(\frac{1-\lambda}{\lambda}\right) \leq \frac{z}{\beta a} \leq \frac{\sqrt{1-\lambda^2}}{\lambda}\right] \tag{29a}$$

and the helical extension of Eq. (29a) is given by

$$\frac{x}{a} = \cos\left(\frac{z}{\beta a} - \sigma_0\right), \quad \left(\text{for } \frac{z}{\beta a} \geq \frac{\sqrt{1-\lambda^2}}{\lambda}\right) \tag{30a}$$

where

$$\sigma_0 = \frac{z_0}{\beta a} = \left(\frac{\sqrt{1-\lambda^2}}{\lambda} - \cos^{-1}\lambda\right) \tag{30b}$$

Thus, in the limit $\lambda = 1$, the boundary is a helix; in the limit $\lambda = 0$, the boundary projection on the x-y plane is the straight-line extension of the Mach element from the tip leading edge—i.e., as the span increases, the body, viewed from the tip leading edge, appears flat. Then the body lift is given by Eqs. (27a) and (27b) *minus* a correction

$$K^{(B^*)} = \frac{1}{[1 - (1/4a_t)]} \left(\frac{S_{B^*}}{S_W}\right) \tag{29b}$$

where

$$\frac{S_{B^*}}{S_W} = \left(\frac{\lambda}{1-\lambda}\right)\left(\left\{1 - \frac{1 + \lambda^2\left[1 - \frac{1}{3}\left(\frac{1-\lambda}{a_t\lambda}\right)^2\right]}{2\lambda}\right\} - a_t\left\{1 - \frac{1 + \lambda^2\left[1 - \frac{1}{3}\left(\frac{1-\lambda}{\lambda}\right)^2\right]}{2\lambda}\right\}\right) \tag{29c}$$

for

$$\left(\frac{1-\lambda}{\lambda}\right) \leq \left(\frac{1-\lambda}{a_t\lambda}\right) \leq \frac{\sqrt{1-\lambda^2}}{\lambda} \left[\text{or } \left(\frac{1-a_t^2}{1+a_t^2}\right) \leq \lambda \leq 1\right]$$

and

$$\frac{S_{B^*}}{S_W} = \left(\frac{\lambda}{1-\lambda}\right)\left(a_t\sqrt{\left(\frac{1+\lambda}{1-\lambda}\right)}\left\{1 - \frac{1+\lambda^2\left[1-\frac{1}{3}\left(\frac{1-\lambda^2}{\lambda^2}\right)\right]}{2\lambda}\right\} - a_t\left\{1 - \frac{1+\lambda^2\left[1-\frac{1}{3}\left(\frac{1-\lambda}{\lambda}\right)^2\right]}{2\lambda}\right\} + \left\{1 - \left(\frac{a_t\lambda}{1-\lambda}\right)\sin\left[\left(\frac{1-\lambda}{a_t\lambda}\right) - \sigma_0\right]\right\} - a_t\sqrt{1-\lambda^2}\right) \quad (30c)$$

$$\sqrt{1-\lambda^2}/\lambda \leq (1 - \lambda/a_t\lambda) \leq [(\sqrt{1-\lambda^2}/\lambda) + \sin^{-1}\lambda]$$

The range of validity is limited by the condition where the boundary defined by Eqs. (29a) and (30a) intersects the body base at the plane of symmetry (y-z plane). For $1/2 \leq a_t \leq 1$, the body lift is plotted for $a_t = 1/2$ and $3/4$ in Fig. 4c. Further approximations along these lines for $0 < a_t < 1/2$ do not appear feasible. Hence, the representation of wing lift for $0 < a_t < \infty$ is next considered.

(2) *Approximate Wing Lift for* $0 < a_t < \infty$

Meaningful approximations for the wing lift are more difficult to obtain for the rectangular case than for the delta case; the difference

$$[K^{(W)}(\lambda, \infty) - K^{(W)}(\lambda, 0)]$$

is uniformly about one-third of that for the delta case. For $a_t \geq 1$, the wing lift can be obtained by graphical integration of the pressure distribution (unpublished). The results of the calculations for $a_t = 1$, $\lambda \geq [1 \div (1 + \pi a_t)]$, are shown in Fig. 4b. By an analysis similar to that for the delta case resulting in Eq. (22b) and the paragraph that follows it, the behavior of wing lift at $\lambda = 0$ and $\lambda = 1$ may be obtained; the results are analogous to the delta case. Thus it is now possible to indicate the approximate behavior of the total lift for intermediate values of a_t. Intermediate curves for $a_t = 1$ and $a_t = 1/2$ are shown in Fig. 4a. For $a_t = 1/2$, the wing lift was assumed to be well approximated by the wing lift for $a_t = 1$. The outstanding feature of the total lift representation for the rectangular case is the marked similarity to that for the delta case (cf. Figs. 2a and 4a): (A) for $a_t = 0$, the lifts are identical; (B) for $a_t = \infty$, the difference in total lift between the two cases is uniformly less than 10 per cent for $0 \leq \lambda \leq 1$, being zero at the end points ($\lambda = 0$ and $\lambda = 1$); and (C) for intermediate values of a_t, the shape of the lift curves are similar for the two cases and the end points are identical. It is emphasized that the similarity lies in the comparison of the *lift ratios*.

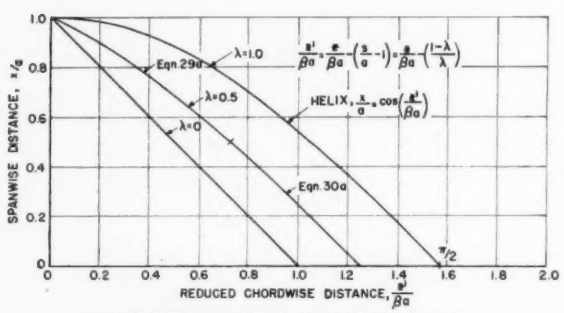

FIGURE 5. COMPARISON OF REGIONS OF INFLUENCE OF TIP LEADING EDGE ON BODY FOR RECTANGULAR WING-BODY

Lift Representation for Clipped-Delta Wing-Body Configurations

The lift representation for the three-parameter family of clipped-delta wing-body configurations, which includes the limiting two-parameter families of delta wing-body ($a_t/m = 1$) and rectangular wing-body ($a_t/m = 0$) configurations, is presented to indicate the generalization possible to other plan forms with straight edges. Again, the details of the analysis are not carried out so completely as for the delta case, but the extension is clear. The three parameters for this case are taken to be a/s ($\equiv\lambda$), a_t, and a_t/m, where $0 \leq a_t/m \leq 1$ (cf. Fig. 1c).

Then the lifts for $a_t = 0$ are precisely† those given for the delta case for $m = 0$ [cf. Eqs. (3a), (4a), and (5a)]. For $a_t = \infty$, the lift obtained by simple integrations is

$$K = K^{(W)} = 1 + \frac{2}{[2-(a_t/m)]}\left[\lambda + \frac{a_t}{m}\left(\frac{\lambda^2}{1-\lambda}\right) + \frac{a_t}{m}\left(\frac{\lambda}{1-\lambda}\right)^2 \ln\lambda\right] \quad (31)$$

and $K^{(B)} \equiv 0$, which reduce to the delta case for $a_t/m = 1$ and to the rectangular case for $a_t/m = 0$. The limiting lift curves are plotted in Fig. 6 for $a_t/m = \sqrt{3}/3$.

(1) *Approximate Body Lift for* $0 < a_t < \infty$

For $a_t \geq 1$ (also implies $m \geq 1$)—i.e., the condition that the Mach element from the leading-edge-body junction intersects the trailing edge—the first approximation for body lift, assuming that the pressure is constant on the body [cf. Eq. (13)], is obtained. Then,

† A recent discussion with Lagerstrom indicates that a proof for more general plan forms including camber exists for this equivalence.[10]

after the procedure following Eq. (14a), the wing area [cf. Eq. (14c)] is

$$S_W/a^2 = (\beta/a_t)[2 - (a_t/m)][(1 - \lambda)/\lambda]^2 \quad (32a)$$

the body area [cf. Eq. (14b)] is

$$S_B/a^2 = 2\beta\left[\left(\frac{1-\lambda}{a_t\lambda}\right) - \sin\left(\frac{1-\lambda}{a_t\lambda}\right)\right] \quad (32b)$$

For

$$\lambda \geq 1/[1 + (\pi/2)a_t] \quad \text{and}$$

$$C_{L\alpha}{}^{(B)} = \frac{4}{\beta}\left[\frac{4}{\pi}\frac{a_t}{\sqrt{a_t^2 - (a_t/m)^2}}\sec^{-1}\left(\frac{a_t}{a_t/m}\right)\right]\frac{1}{[2 - (a_t/m)]}\left(\frac{\lambda}{1-\lambda}\right)\left[1 - \left(\frac{a_t\lambda}{1-\lambda}\right)\sin\left(\frac{1-\lambda}{a_t\lambda}\right)\right] \quad (32c)$$

For $\lambda \leq 1/[1 + (\pi/2)a_t]$, the body area [cf. Eq. (14e)] is

$$S_B/a^2 = 2\beta\{[(1 - \lambda)/a_t\lambda] - 1\} \quad (32d)$$

and

$$C_{L\alpha}{}^{(B)} = \frac{4}{\beta}\left[\frac{4}{\pi}\frac{a_t}{\sqrt{a_t^2 - (a_t/m)^2}}\sec^{-1}\left(\frac{a_t}{a_t/m}\right)\right]\frac{1}{[2 - (a_t/m)]}\left(\frac{\lambda}{1-\lambda}\right)\left[1 - \left(\frac{a_t\lambda}{1-\lambda}\right)\right] \quad (32e)$$

where the basic lift of the "exposed wing" alone[11] is

$$C_{L\alpha} = \frac{4}{\beta}\frac{1}{a_t/m[2 - (a_t/m)]}\left\{1 - [1 - (a_t/m)]^2\sqrt{\frac{a_t}{a_t - (a_t/m)}}\right\} \quad (\text{for } a_t \geq 1) \quad (32f)$$

For $m \geq 1$ (supersonic leading edge) and $1/2 \leq [1 - (a_t/m)] \leq a_t \leq 1$ (for $a_t/m \leq 1/2$) or $1/2 \leq a_t \leq 1$ (for $a_t/m \geq 1/2$)—i.e., the condition that neither the Mach element from the tip leading edge *nor* the side-edge reflection of the Mach element from the leading-edge-body junction hits the body—the body lifts $C_{L\alpha}{}^{(B)}$ are given by Eqs. (32c) and (32e), but the basic lift is

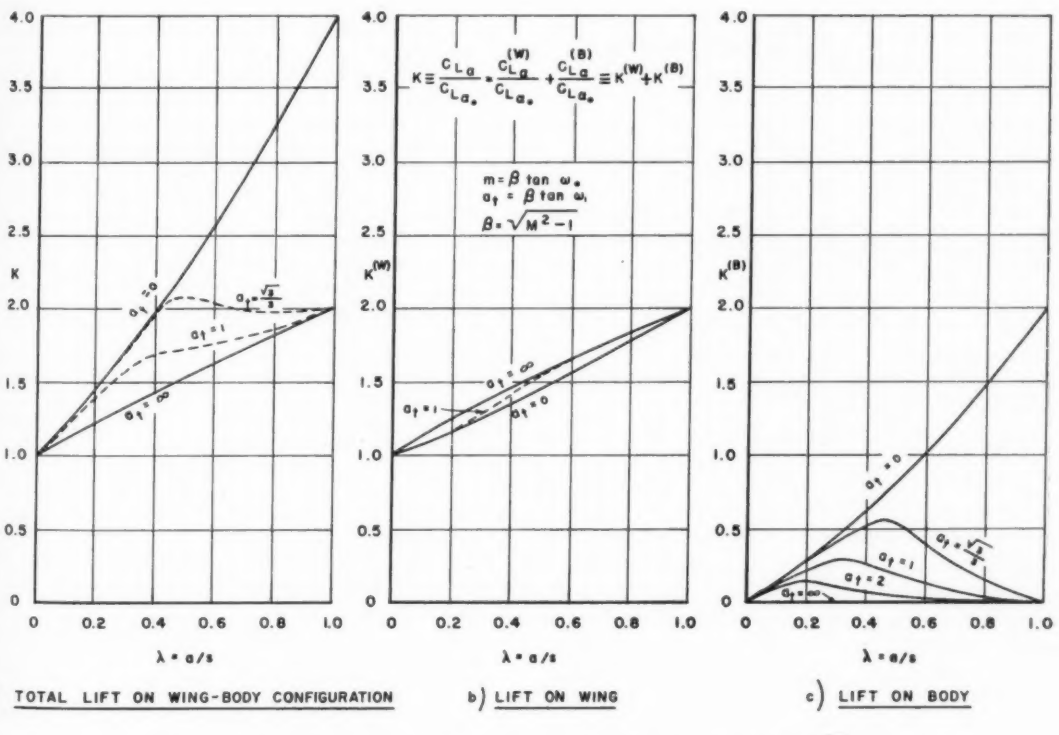
K ≡ C_Lα/C_Lα* = C_Lα^(W)/C_Lα* + C_Lα^(B)/C_Lα* ≡ K^(W) + K^(B)
m = β tan ω*
a_t = β tan ω_t
β = √(M² − 1)
K
K^(W)
K^(B)
λ = a/s
a) TOTAL LIFT ON WING-BODY CONFIGURATION
b) LIFT ON WING
c) LIFT ON BODY

FIGURE 6. CLIPPED-DELTA WING-BODY LIFT WITH NO AFTERBODY, $a_t/m = \frac{\sqrt{3}}{3}$

$$C_{L\alpha_0} = \frac{4}{\beta}\frac{1}{a_t/m[2-(a_t/m)]}\left\{\left[1-\frac{2}{\pi}\cos^{-1}(2a_t-1)\right]+\frac{[1+(a_t/m)]^2}{\pi}\sqrt{\frac{a_t}{a_t+(a_t/m)}}\times\right.$$
$$\left.\cos^{-1}\left[\frac{(a_t/m)+2a_t-1}{1+(a_t/m)}\right]-\frac{[1-(a_t/m)]^2}{\pi}\sqrt{\frac{a_t}{a_t-(a_t/m)}}\cos^{-1}\left[\frac{(a_t/m)-2a_t+1}{1-(a_t/m)}\right]\right\} \quad (32g)$$

for $m \geq 1$ and $a_t \leq 1$. The body lifts from Eqs. (32c), (32e), (32f), and (32g) are plotted in Fig. 6c for $a_t = 2$, 1, and $\sqrt{3}/3$. A second approximation for body lift may be made similar to the delta case [cf. Eqs. (17b) and (17c)], and an approximation for body lift for $m \geq 1$ and $1/2 \leq a_t \leq [1-(a_t/m)]$ (for $0 \leq a_t/m \leq 1/2$) may be made similar to the rectangular case [cf. Eqs. (29b), (29c), and (30c)]; but, since nothing essentially new is contributed, these approximations are not presented.

Also, for $0 \leq m < 1$ (subsonic leading edge), approximate expressions for body lift similar to those given for the delta case [cf. Eqs. (19a), (19b), and (20)] can be obtained but are not presented here.

(2) *Approximate Wing Lift for* $0 < a_t < \infty$

For $a_t \geq 1$, the wing lift can be obtained by graphical integration of the pressure distribution; but, since the calculations are more tedious than for either the delta or rectangular cases, a faired curve for $a_t = 1$ is shown in Fig. 6b. The behavior of the wing lift and slope at $\lambda = 0$ and $\lambda = 1$ can be investigated as in the delta case, but the results are clear and the details are not presented here.

The representation of the total lift is now possible for the clipped-delta case over the entire range of the parameters. Curves for two intermediate values of $a_t = 1$ and $\sqrt{3}/3$ are shown in Fig. 6a, where the faired wing lift for $a_t = 1$ is taken for both values of a_t.

The extension of the analysis to other cylindrical body shapes (e.g., elliptical bodies) and to other wing plan forms with straight edges (e.g., swept trailing edge and/or inclined side edge) is now clear. Also, the representation of drag, moment, and center of pressure may be initiated along lines similar to those presented in this paper for lift.

Experimental Verification

Some experimental results that verify the present analysis in part are available, but the data do not cover a sufficiently large range of the parameters in order to determine completely the behavior of the lift ratio. Suggestions for future experimental work include the following: (A) Reliable measurements of the basic wing lift curve slope $C_{L\alpha_0}$. A fairly extensive series of tests on delta wings have been carried out.[12] (B) A systematic series of tests on delta wing-body configurations without afterbody with particular attention to the validity of the parameter $m = \beta \tan \omega_0$. (C) Independent measurement of the body (or wing) lift, and (D) measurement of afterbody lift. Also, since the theoretical calculations are difficult, pressure measurements on the body adjacent to the wing are of particular interest.

References

[1] Beskin, L., *Determination of Upwash Around a Body of Revolution at Supersonic Velocities*, Applied Physics Laboratory, The Johns Hopkins University, Report No. CM-251, May 27, 1946.

[2] Lagerstrom, P. A., and Van Dyke, M. D., *General Considerations About Planar and Non-Planar Lifting Systems*, Douglas Report No. SM-13432, Santa Monica, June, 1949.

[3] Spreiter, J. R., *Aerodynamic Properties of Slender Wing-Body Combinations at Subsonic, Transonic, and Supersonic Speeds*, N.A.C.A. T.N. No. 1662, July, 1948.

[4] Morikawa, G. K., *The Wing-Body Problem for Linearized Supersonic Flow*, California Institute of Technology (Thesis), Pasadena, Calif., June, 1949; or Jet Propulsion Laboratory, California Institute of Technology, Progress Report 4-116, December, 1949.

[5] Cohen, Doris, *The Theoretical Lift of Flat Swept-Back Wings at Supersonic Speeds*, N.A.C.A. T.N. No. 1555, March, 1948.

[6] Ward, G. N., *Supersonic Flow Past Thin Wings. II—Flow-Reversal Theorems*, Quarterly Journal of Mechanics and Applied Mathematics, Vol. II, Part 3, 1949.

[7] Ferrari, C., *Interference Between Wing and Body at Supersonic Speeds—Theory and Numerical Applications*, Journal of the Aeronautical Sciences, Vol. 15, No. 6, pp. 317–336, June, 1948; and *Interference Between Wing and Body at Supersonic Speeds—Note on Wind Tunnel Results and Addendum to Calculations*, Journal of the Aeronautical Sciences, Vol. 16, No. 9, pp. 542–546, September, 1949.

[8] Lomax, Harvard, and Heaslet, Max. A., *Linearized Lifting-Surface Theory for Swept-Back Wings with Slender Planforms*, N.A.C.A. T.N. No. 1992, December, 1949.

[9] Graham, Martha E., *Some Linearized Computations of Supersonic Wing-Tail Interference*, Douglas Report No. SM-13430, Santa Monica, December 23, 1948.

[10] Lagerstrom, P. A., and Graham, Martha E., *Remarks on Low-Aspect-Ratio Configurations in Supersonic Flow*, Journal of the Aeronautical Sciences, Vol. 18, No. 2, pp. 91–96, 100, 1951.

[11] Lapin, Ellis, *Formulas for the Theoretical Lift of Flat Wings at Supersonic Speeds*, Journal of the Aeronautical Sciences, Vol. 16, No. 6, pp. 381–383, June, 1949.

[12] Ellis, M. C., and Hasel, L. E., *Preliminary Investigation at Supersonic Speeds of Triangular and Sweptback Wings*, N.A.C.A. T.N. No. 1955, October, 1949.

The Interaction of Shock Waves with Boundary Layers on a Flat Surface*

F. W. BARRY,† A. H. SHAPIRO,‡ AND E. P. NEUMANN**

Massachusetts Institute of Technology

SUMMARY

The development of supersonic compressors, supersonic diffusers, and high-speed aircraft points to the increasing importance of the interaction between shock waves and boundary layers.

The experimental work reported here is intended to (1) provide a better understanding of the nature of the shock-boundary-layer interaction, (2) serve as a guide and stimulus to theoretical work, and (3) develop an empirical method for predicting the effects of the interaction.

Experiments were performed on the reflection of an oblique shock from a boundary layer on a flat surface at a Mach Number of 2.05. The effects of shock strength and boundary-layer régime (laminar, transition, or turbulent) on the interaction phenomena were explored.

The results are in the form of schlieren photographs, constant-density contours found from interferometer photographs, and static pressure distributions at the plate surface.

NOMENCLATURE

Fig. 1 shows the meaning of some of the symbols and the regions to which the numerical subscripts refer.

L_t = see Fig. 1
M = Mach Number
p = pressure
R_i = Reynolds Number = $V_1 x_i \rho_1/\mu_1$
R_t = Reynolds Number = $V_1 x_t \rho_1/\mu_1$
V_1 = free-stream velocity
x = horizontal distance from leading edge of plate, in. (see Fig. 1)
δ_t = boundary-layer displacement thickness = $3.83 x_t/\sqrt{R_t}$
ϵ = angle between stream line and plate surface, negative if flow is toward plate, deg.
ϵ_t = angular deflection of apparent edge of boundary layer (see Fig. 1), as measured from photographs, deg.
θ = shock generator angle (positive as shown in Fig. 1), deg., used as a measure of shock strength
μ = free-stream viscosity
ρ = density

The flow is from left to right in all figures and photographs.

Received May 18, 1950.

* This work was carried out as part of the Guided Missiles Program (Project Meteor) at the Massachusetts Institute of Technology and was sponsored by the Bureau of Ordnance of the Navy Department.

The staff of the Gas Turbine Laboratory have contributed to this report in discussions, in constructing and operating the equipment, and in reducing the data. Their help is acknowledged with thanks.

† Research Associate, Department of Mechanical Engineering.

‡ Associate Professor of Mechanical Engineering.

** Associate Professor of Mechanical Engineering.

INTRODUCTION

General Considerations

EXPERIMENTAL WORK WITH subsonic flows has justified the assumption that one may usually analyze a boundary layer independently of the main flow. Experimental work with transonic and supersonic flows, on the other hand, has shown that for such flows one may not analyze a boundary layer inde-

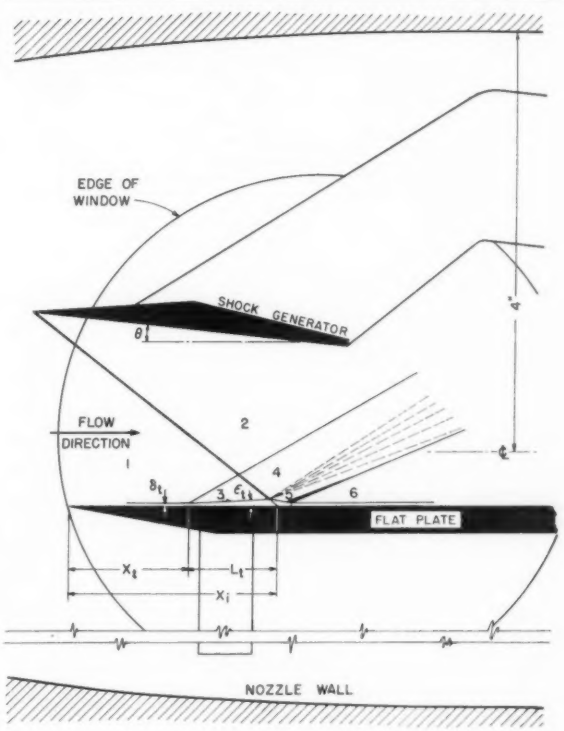

FIG. 1. Cross section through apparatus and tunnel. Illustrates nomenclature.

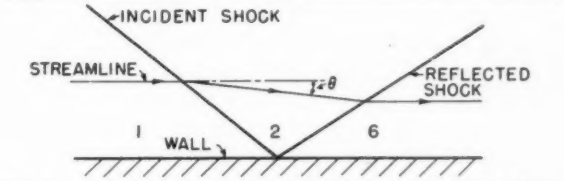

FIG. 2. Theoretical "regular reflection" of a shock from a plane wall.

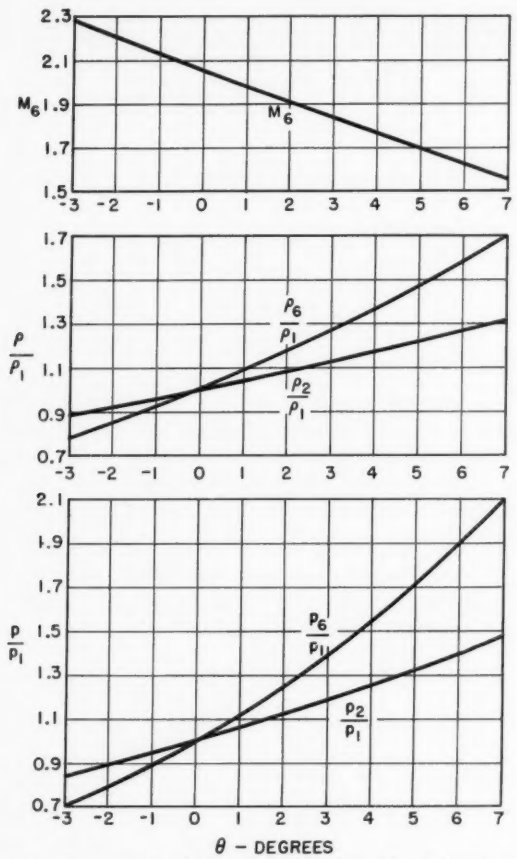

FIG. 3. Theoretical relations for "regular reflection" from a plane wall at a Mach Number of 2.05.

pendently of the main flow, except for those few cases where shock waves do not meet a boundary layer. That is, shock waves have been found to interact with boundary layers to cause significant departures from the theoretical flow, both in the boundary layer and in the main flow outside of it.

The simple theoretical solutions for the reflection of a shock in a parallel, uniform, supersonic flow are too well known to need more than brief mention.

A weak oblique shock reflects from a plane wall as an oblique shock that turns the flow parallel to the wall (Fig. 2). The overall pressure rise is about twice that of the incident shock. Fig. 3 shows some theoretical relations for this type of reflection at a Mach Number of 2.05.

An oblique shock reflects from a surface of constant pressure as an expansion wedge to preserve uniform pressure at the surface (Fig. 4). The overall deflection of the flow is about twice that across the shock.

No account is taken of the boundary layer in the simple cases mentioned above. However, the subsonic layer next to the wall has a marked effect on the flow because pressure disturbances, which cannot propagate upstream in a supersonic flow, do propagate upstream in a subsonic flow. Furthermore, the enormous pressure gradient that occurs in the incident shock in the supersonic part of the flow cannot occur in a subsonic flow. Therefore, near the wall, the region in which the pressure rises will extend both upstream and downstream of the point of incidence. As a result, the subsonic layer will thicken and deflect the stream lines in the supersonic region away from the wall. This deflection will give rise to "reflected" compression waves that originate upstream of the point of incidence, as shown in Fig. 5. These waves cross, and thereby modify, the incident shock.

The incident shock will become more nearly normal as it traverses the supersonic portion of the boundary layer and will produce a series of reflected waves.[1, 2] If the boundary layer thickens considerably or separates, there will be a thick subsonic layer next to the wall. Hence, the incident shock must reflect substantially as an expansion wave (Figs. 4 and 5), since the subsonic layer cannot support a large longitudinal pressure gradient. The flow following the expansion will, in general, be inclined toward the wall. As the boundary-layer flow turns parallel to the wall, a series of compression wavelets are propagated into the main stream (Fig. 5).

The system of reflected expansion and compression waves coalesces into a single oblique shock at some distance from the point of incidence. If the flow after this reflected shock is parallel to the wall, the reflected shock will be identical to the theoretical reflected shock of a "regular reflection." Therefore, the overall pressure rise should be nearly the same as the theoretical rise (Fig. 3), even near the wall, because the differences in entropy increase for different parts of the shock system are not large.

As a result of all these effects, it is evident that the shock modifies considerably the flow in the boundary

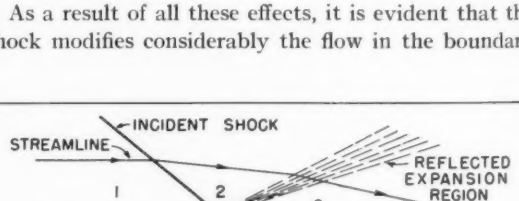

FIG. 4. Theoretical reflection of a shock from a constant-pressure surface.

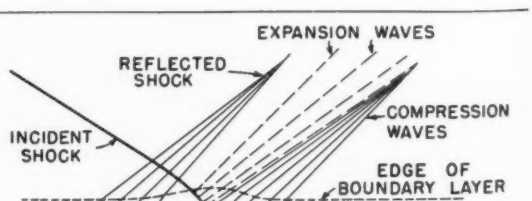

FIG. 5. Reflection of a shock from a plane wall with a boundary layer.

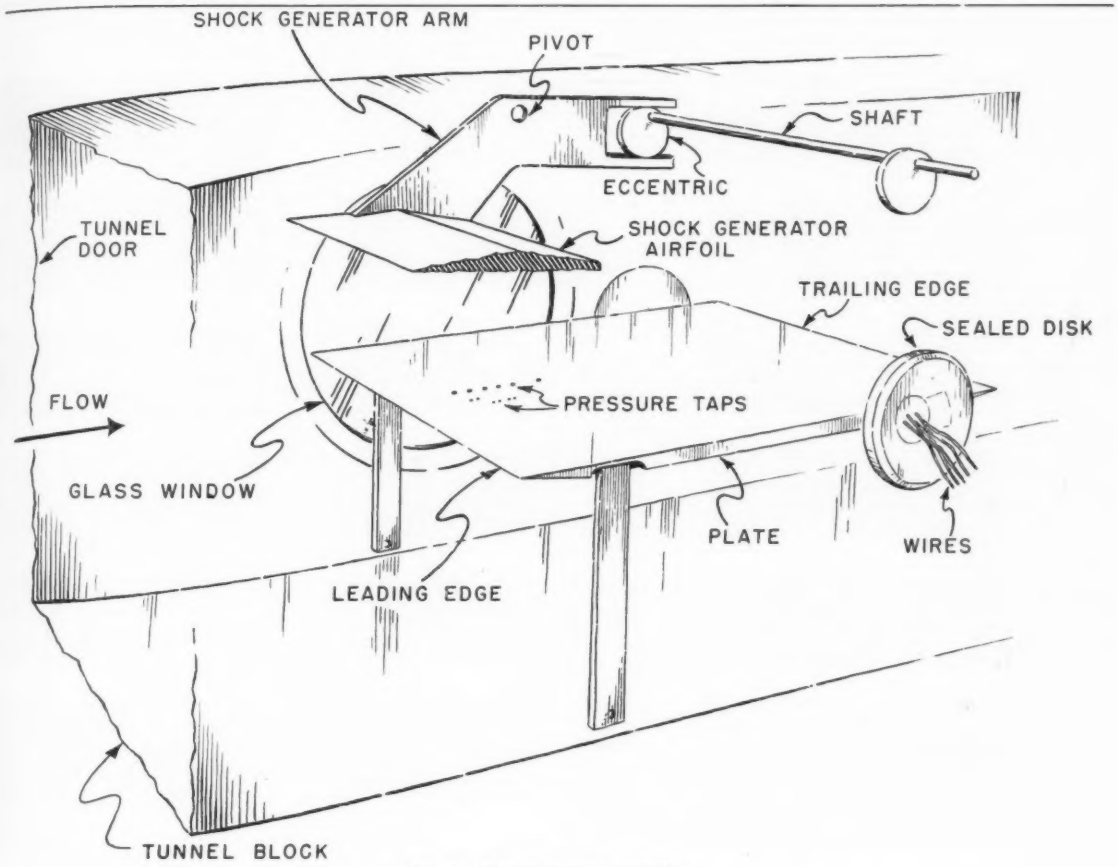

FIG. 6. Sketch of the apparatus.

layer and that the changes in boundary-layer flow not only alter the incident shock but also give rise to a reflected wave system far more complex than the "regular reflection" from a plane wall illustrated in Fig. 2. The essence of the process, therefore, is a mutual interaction between the shock and the boundary layer.

Previous Work

The quantitative results of the present report are an extension of the qualitative investigations by the same authors[1] and contain the principal results of the investigation that is reported in detail in a thesis by Barry.[3]

Fage and Sargent[4] studied the interaction of normal and oblique shocks with a *turbulent* boundary layer on a flat wall at Mach Numbers up to 1.47. They present impact and static pressure surveys in the stream, wall-surface-pressure traverses and wall-friction traverses below the shock waves, and schlieren and shadow photographs. They found that the shock bifurcates near the boundary layer when its strength exceeds a definite value, that the surface drag coefficient falls rapidly between the two bifurcated limbs, and that the shock-wave angles are influenced by interaction with the boundary layer.

Liepmann, Ashkenas, and Cole,[5] * in an investigation at a Mach Number of 1.25, found that a weak shock reflects from a laminar boundary layer on a flat surface as a combination of shocks and expansion waves and from a turbulent layer as an oblique shock.

A few analytical studies have been published. Tsien and Finston[7] applied linearized potential flow theory to a model that consists of a uniform subsonic stream bounded on one side by a wall and on the other side by a uniform semi-infinite supersonic stream. They found that the distance that pressure disturbances (caused by a weak wave in the supersonic stream) are transmitted upstream is proportional to the thickness of the subsonic layer and is a function of the Mach Numbers of the subsonic and supersonic streams. Their results can hardly be compared with the present experimental results because of the simplicity of their model.

Lees[8] predicted the effects of Reynolds Number, shock strength, and Mach Number on the surface pressure distribution and on the location of the point of separation of a laminar boundary layer. He cal-

* Further experimental data will presumably be given in reference 6.

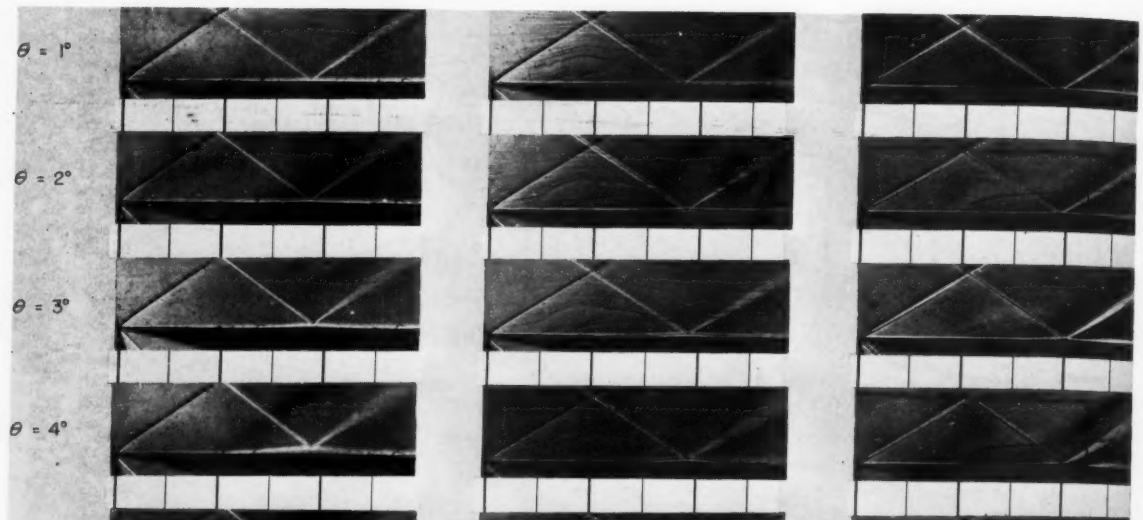

FIG. 7. Schlieren photographs, arranged in columns of constant Reynolds Number and in rows of constant shock strength; knife-edge parallel to plate; exposure: 1 microsec.; $M = 2.05$.

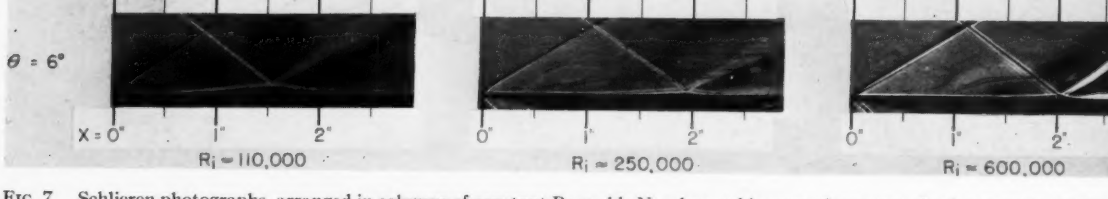

FIG. 8a (*top*). Illustrates effect of shock strength on the thickness of the boundary layer for $R_i = 600{,}000$, traced from schlieren photographs. FIG. 8b (*bottom*). Illustrates effect of Reynolds Number on the thickness of the boundary layer for $\theta = 6°$, traced from schlieren photographs.

culated the growth of the boundary layer up to the separation point by means of a modified Pohlhausen method and assumed a somewhat arbitrary pressure distribution to calculate the remainder of the flow. The experimental results of the present investigation are only in partial agreement with the theoretical prediction of Lees.

Experimental Procedure

The investigation was conducted in the 8- by 8-in. tunnel of the M.I.T. Gas Turbine Laboratory at a Mach Number of 2.05. Fig. 1 is a cross section through the tunnel showing the shock generator and leading part of the flat plate, and Fig. 6 is a schematic view of the apparatus in the tunnel.

Experiments were performed at four Reynolds Numbers—namely, about 110,000, 250,000, 600,000, and 1,200,000. For the highest Reynolds Number the boundary layer seems to be in the transition region. In one run, discussed separately, a wire was glued to the plate near the leading edge to trip the boundary layer. Shock deflection angles up to 7° were employed. Schlieren photographs were taken for every combination of variables, and interferometer photographs were taken at the two intermediate Reynolds Numbers. Pressures along the plate surface near the mid-plane of the tunnel were measured for the three lowest Reynolds Numbers and for the tripped turbulent boundary layer.

The boundary layer was formed on a flat plate that spanned the tunnel at zero angle of attack near the center of the tunnel. The foremost $4^1/_2$ in. of the plate were visible through the optical flats set into the tunnel sidewalls.

The shock-generator airfoil could be adjusted through a range of positive and negative angles of attack while the tunnel was running. Most of the data were taken with the generator arms shown in Figs. 1 and 6 where x_i was about 1.9 in. By means of a second set of arms it was possible to make x_i about 3.8 in., thus permitting runs at Reynolds Numbers up to 1,200,000 and also a pair of runs with the same Reynolds Number (600,000) but different values of x_i. With each set of arms the Reynolds Number was altered by changing the tunnel pressure.

Because it was impossible to keep the leading edge of the shock generator extremely sharp and because of boundary-layer formation on its surface, the generator produced a compression wave followed by a rarefaction wave even when it was set at zero or negative angles. Therefore, for angles less than 1.5°, the nominal angular setting of the shock generator is an unreliable measure of shock strength.

The schlieren photographs were taken with a 5-in. schlieren apparatus[9] at an exposure time of less than 1 microsec. The knife-edge was parallel to the plate for all the photographs, which means that the photographs show density gradients normal to the plate surface. Because of the large length of light path through the tunnel (8 in.), refraction at high tunnel pressures produced such optical illusions as an apparent bending of the plate surface and an apparent kinking of a wire outside the tunnel (see Fig. 7). In some of the photographs the incident shock appears to be composed of as many as six parallel shocks. This, of course, is not possible. The departures from two-dimensional flow due to an observable oscillation of the shock and the boundary layers on the sidewalls account for at least part of this effect. Streaks of oil on the tunnel glass walls may also be seen in some of the photographs.

The interferograms are time exposures taken with a Mach-Zehnder interferometer.[10]

Results with Laminar Boundary Layers

Qualitative Results

The qualitative results obtained with the large tunnel described in this report are in accord with the results obtained previously with a 1.3- by 1.3-in. tunnel[1] and are summarized below.

The schlieren photographs of Fig. 7 illustrate the remarks of this section.

The reflected wave system is seen to comprise a series of compression waves caused by the thickening of the boundary layer upstream of the point of incidence, an expansion region originating at the point of incidence, and a downstream compression region. Thus, the observed flow pattern is qualitatively similar to that predicted analytically and shown in Fig. 5.

Consider any column of photographs in Fig. 7. For a small shock strength—i.e., for photographs near the top—the components of the reflected wave system are spaced closely together. The boundary layer seems to thicken slightly near the point of incidence and to become turbulent downstream of the region of interaction.

As the shock strength is increased—i.e., for photographs near the bottom of the column—the first reflected shock and the point at which the boundary layer begins to thicken move upstream. The downstream boundary layer becomes much thicker and highly turbulent. The zone of interaction therefore spreads both upstream and downstream as the shock strength increases. The reflected expansion wave and subsequent shock still occur.

The effects of a change in Reynolds Number, on the other hand, may be seen by considering any particular row. A decrease in Reynolds Number spreads out the region of interaction along the plate but does not alter the reflected wave pattern appreciably.

Fig. 8 shows the effects of Reynolds Number and shock strength on the boundary-layer thickness to scale. Quantitative data on the behavior of the boundary layer are discussed below.

Effect on Boundary Layer

Inspection of the schlieren photographs (Fig. 7) shows that the boundary layer begins to thicken at a rather well-defined point. The location of this point, as measured on the schlieren photographs, is given in Figs. 9 and 10.

Fig. 9, for example, shows that L_t/x_t increases rapidly with shock strength at first and less rapidly as the shock strength becomes large. The ratio L_t/x_t increases with decreasing Reynolds Number, thus showing that the effect of the shock is felt farther upstream as the boundary-layer thickness increases. Increasing x_t, without altering R_t, seems to increase both L_t/x_t and L_t/δ_t slightly. The curves for the highest Reynolds Number (1,200,000) are dissimilar to the other curves, especially in Fig. 10, probably because the boundary layer has entered the transition region before the region of interaction.

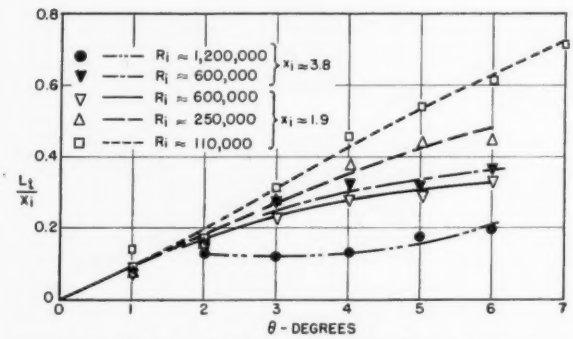

FIG. 9. Plot of the ratio L_t/x_t as a function of shock strength for various values of Reynolds Number.

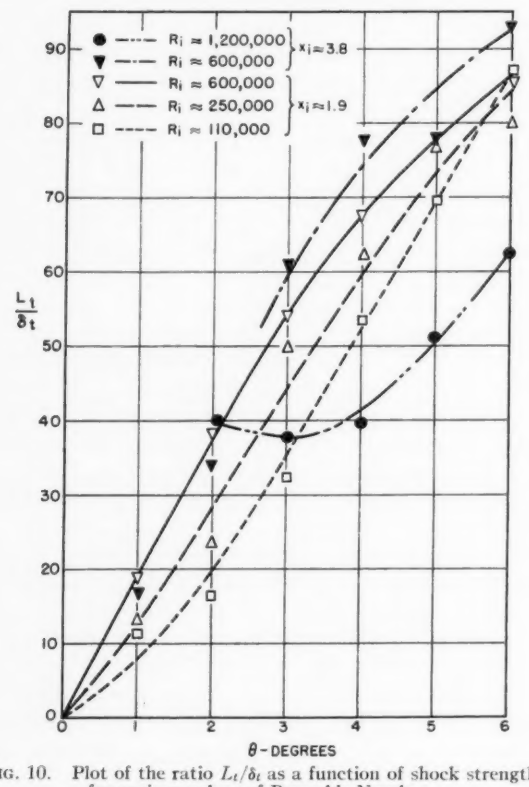

FIG. 10. Plot of the ratio L_t/δ_t as a function of shock strength for various values of Reynolds Number.

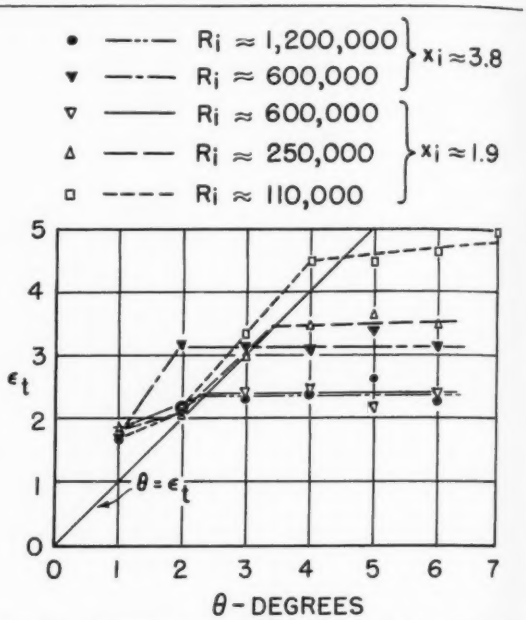

FIG. 11. Apparent angular deflection (ϵ_t) of the edge of the boundary layer upstream of the point of incidence as a function of shock strength for various values of Reynolds Number.

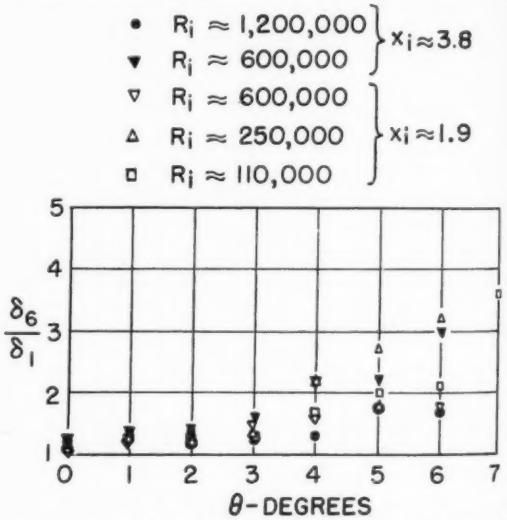

FIG. 12. Ratio of the thickness of the boundary layer after and before the region of interaction as a function of shock strength for various values of Reynolds Number; measured from photographs.

In Fig. 11 it is shown that for weak shocks the angular deflection of the apparent edge of the boundary layer seems to be approximately equal to the deflection of the flow through the incident shock (θ); but for values of θ above a certain critical value, the boundary-

layer deflection angle remains substantially constant. The maximum value of ϵ_t increases with decreasing Reynolds Number and, for a Reynolds Number of 600,000, increases as x_1 increases. This interesting phenomenon of a maximum value of boundary-layer deflection is probably associated with the maximum pressure gradient that a boundary layer in supersonic flow can tolerate.

Fig. 12 indicates the increase in boundary-layer thickness through the region of interaction as a function of shock strength. This figure should be regarded as only qualitative, because the measurements from the photographs are subject to errors due to refraction and to uncertainty regarding the position of the edge of the turbulent boundary layer after the interaction.

Pressure on Plate Surface

Some selected pressure distributions measured at the plate surface are shown in Fig. 13. The short horizontal lines on the right indicate the theoretical pressure rise for a "regular reflection" (Fig. 3). In every case the measured pressure rise is close to the theoretical one.

The short vertical dashes on the curves indicate the location of the point where the boundary layer begins to thicken (x_t) and of the point of incidence (x_i), both as measured on the schlieren photographs. The pressure rise begins close to the point of thickening (x_t), thus showing good correlation between the two methods of determining the extent of the influence of the shock on the boundary layer.

For the lowest shock strength ($\theta = 1°$), the pressure rises and then falls slightly to a uniform value. The slight drop is caused by the expansion that follows the incident shock at this low shock strength.

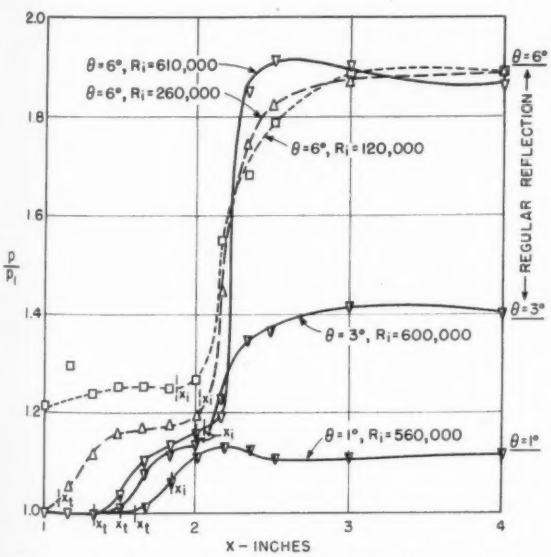

FIG. 13. Static pressure distribution on the plate surface for selected values of shock strength and Reynolds Number; the measured values of x_i and x_t are shown by vertical lines; the theoretical downstream pressures for "regular reflection" are shown on the right; p_1 is free-stream static pressure.

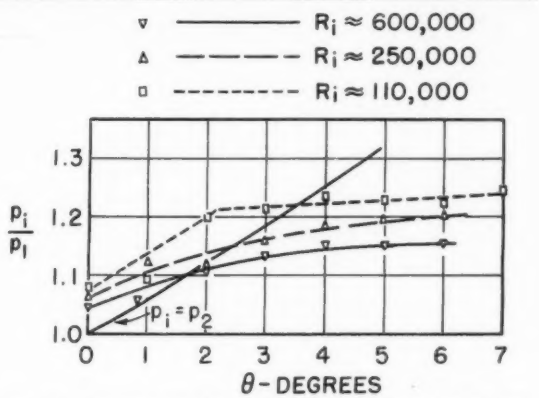

FIG. 14. Pressure on the plate surface at the point of incidence as a function of shock strength for three Reynolds Numbers; p_1 is free-stream static pressure.

For the larger shock strengths, the pressure rises for a short distance and then tends to level off at a value that depends on the Reynolds Number. The remainder, and indeed the largest part, of the pressure rise occurs after the point of incidence and is presumably associated with the downstream reflected compression waves.

Fig. 14 shows that the measured pressure at the point of incidence is fairly constant for the larger shock strengths and increases with decreasing Reynolds Number. This result is in accord with the variation of boundary-layer deflection angle shown in Fig. 11.

By plotting p_i/p_1 against R_t for the regions of Fig. 14 where the curves are substantially flat, it is found that the measured pressure rise to the point of incidence for large shock strengths varies approximately as $1/(R_t)^{1/4}$, in accord with Lees' theory.

Density Fields

Figs. 15a, 16, 17b, and 18 show the contours of constant density for four combinations of R_t and θ. The constant-density lines are labeled with the corresponding density ratio, referred to the free-stream density. A band shift to the left in the interferograms indicates a decrease in density.

The overall density ratio (ρ_6/ρ_1) and the density ratio across the incident shock (ρ_2/ρ_1) agree to within 3 per cent of the theoretical values for "regular reflection" (Fig. 3), except for Fig. 17b, where the interferogram does not extend far enough downstream to include the region where the flow is parallel to the wall.

Fig. 17a was taken at a low tunnel density to ensure that refraction would not be troublesome. This interferogram, like the schlieren photographs, shows that a region of low density gradient lies next to the surface. It is believed that the boundary layer has separated from the plate, although there is insufficient

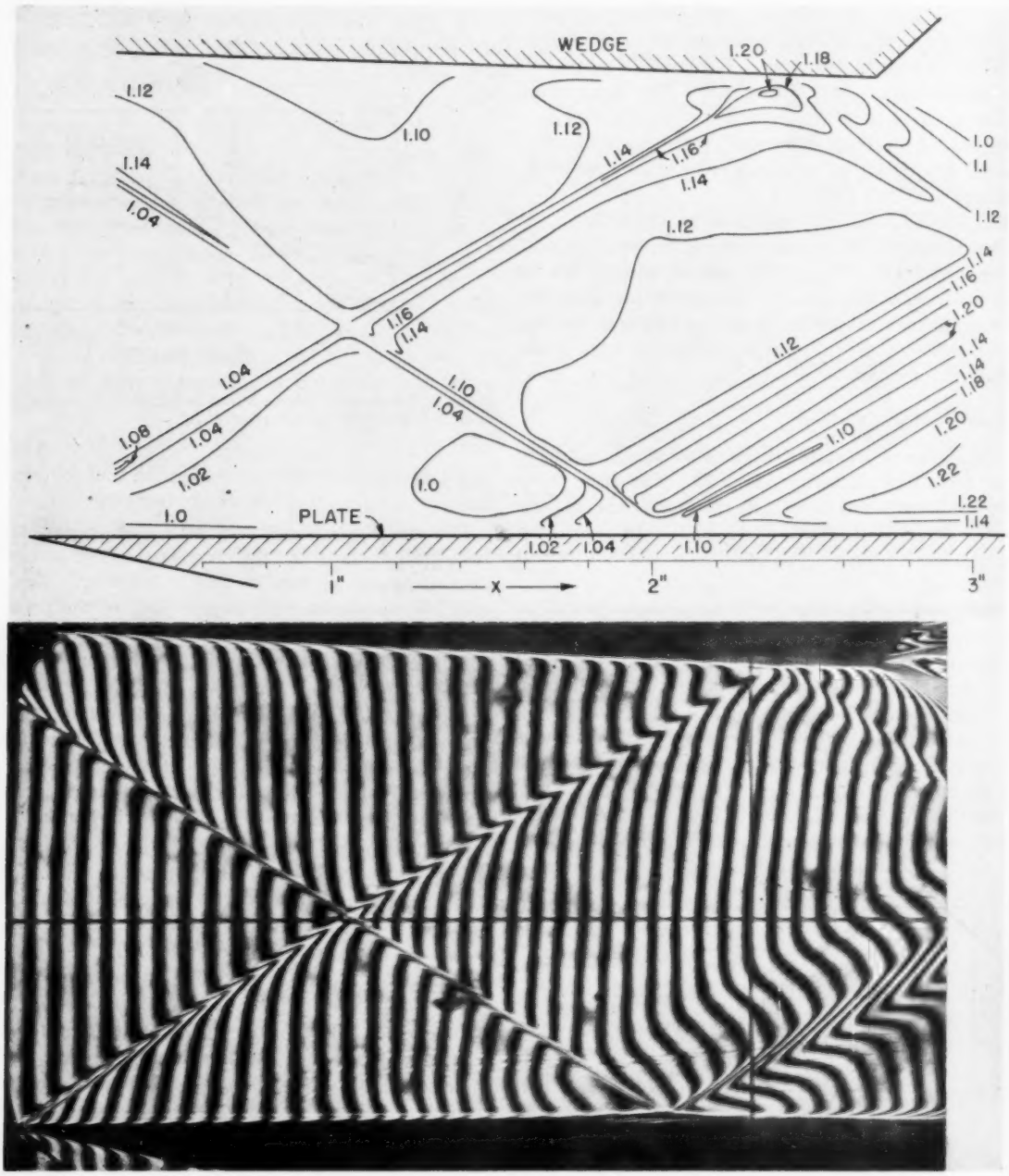

FIG. 15a (*top*). Lines of constant density ratio (referred to free-stream density) obtained from Fig. 15b; $\theta = 3°$; $R_i = 610{,}000$.
FIG. 15b (*bottom*). Interferogram; $\theta = 3°$; $R_i = 610{,}000$; $M = 2.05$; 1-sec. exposure.

experimental evidence to show whether backflow exists at the surface.

A Simple Model of the Wave Pattern

The simplified model of the wave pattern discussed in this section is of interest for two reasons. First, the flow field of the model is at least a first step toward a means for predicting the effects of the interaction and is also suggestive for further theoretical work.

Second, it was desired to obtain information about the flow which could not be obtained directly from an experiment. In particular, the flow directions in the reflected wave system cannot be measured directly by any available technique but may be found from the model. The accuracy of the model cannot be determined from experimental data on flow directions but must be determined from other data, such as densities. However, if the model is accurate with respect to

densities, it is also accurate with respect to flow directions because waves of only one family, except the incident shock, exist, and, therefore, the density is related to the flow direction. If the shocks are extremely weak, the flow is essentially isentropic and this relationship is unique.

The method described here is not intended to be correct in details, since the compression regions are replaced by single oblique shocks for simplicity; nor is the method intended to describe the flow in the boundary layer where the assumption of a relationship between flow properties is invalid. Furthermore, the method is restricted to cases within the range of the experiments with laminar boundary layers, since it requires the use of experimental data.

The following procedure is used to calculate a wave pattern (e.g., Fig. 19) for chosen values of shock strength and Reynolds Number. The location of the point where the boundary layer begins to thicken, t, is obtained from Fig. 9. A single oblique shock, a, is assumed to originate at this point and to have a deflection angle equal to the measured deflection angle of the edge of the boundary layer, ϵ_t (Fig. 11). The properties of the flow in region 4 may be calculated by assuming that the overall deflection angle and pressure ratio of shocks a and d equal those of shocks c and b. The flow in region 5 is found by assuming that the incident shock d reflects as an expansion wave to make $p_3 = p_5$. The properties of the downstream shock e and of the flow in region 6 may be found by making the deflection angle of this shock equal to $-\epsilon_5$, and thus the downstream flow will be parallel to the wall. The thickness of the boundary layer upstream of the interaction (δ_1) may be found from R_t and x_t, and the thickness downstream (δ_6) may be estimated with the aid of Fig. 12. In the region of interaction the edge of the boundary layer is assumed to be formed of straight lines, and thus the geometry of the figure is completely determined through a combination of model assumptions and experimental data.

Except for small differences due to irreversibilities in the shocks, the flow conditions behind the region of interaction, as calculated by this method, should be the same as those for a "regular reflection" (Fig. 3).

Table 1 lists some pertinent flow parameters of four typical wave-pattern models, together with corresponding experimental data. Fig. 19 is a sketch to scale of the model whose parameters are listed in the right-hand column ($\theta = 6°$, $R_t = 120{,}000$) and for which the actual wave pattern is shown in Fig. 7, bottom left.

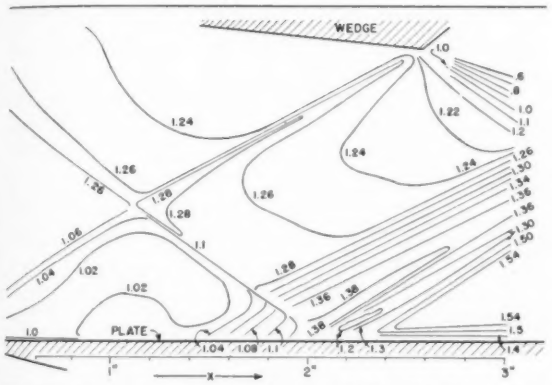

FIG. 16. Lines of constant density ratio (referred to free-stream density); $\theta = 6°$; $R_i = 610{,}000$.

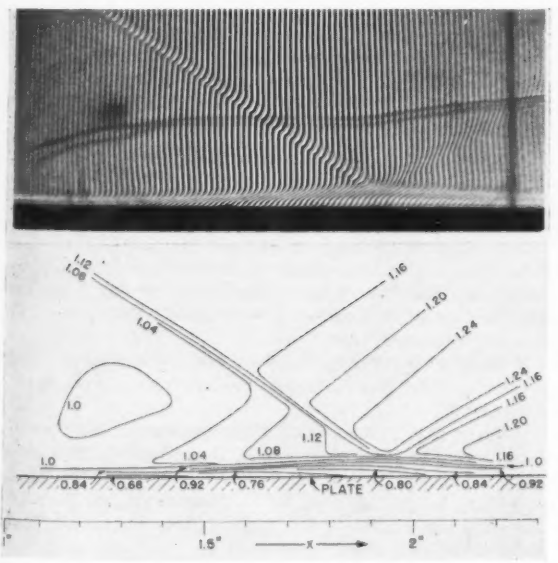

FIG. 17a (*top*). Interferogram; $\theta = 3°$; $R_i = 270{,}000$; $M = 2.05$. FIG. 17b(*bottom*). Lines of constant density ratio (referred to free-stream density) obtained from Fig. 17a; $\theta = 3°$; $R_i = 270{,}000$.

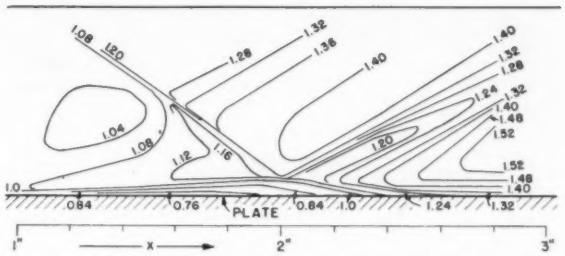

FIG. 18. Lines of constant density ratio (referred to free-stream density); $\theta = 6°$; $R_i = 270{,}000$.

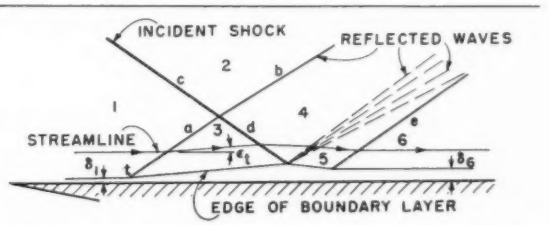

FIG. 19. Model wave pattern for $\theta = 6°$, $R_i = 120{,}000$; shows regions and waves referred to in explanation of calculation procedure.

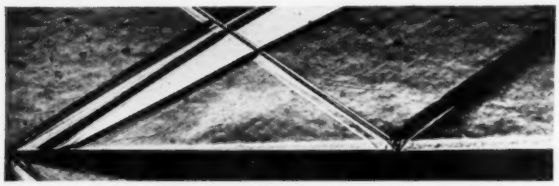

FIG. 20. Schlieren photograph; turbulent boundary layer with trip wire near leading edge; $\theta = 6°$; knife-edge parallel to plate; exposure: 1 microsec.; $M = 2.05$.

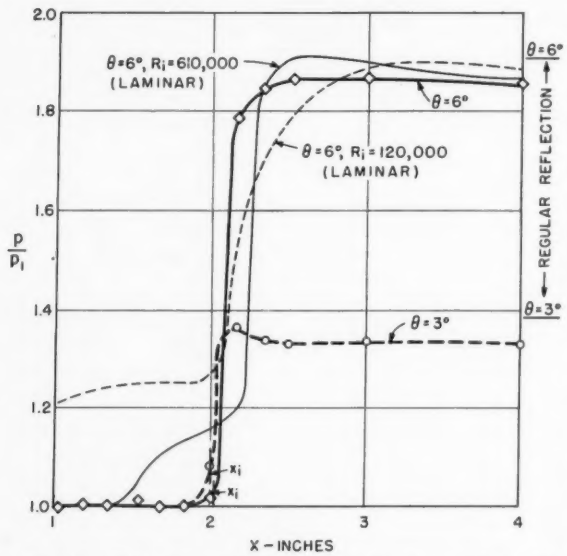

FIG. 21. Static pressure distribution on the plate surface with a tripped turbulent boundary layer for two shock strengths. Two curves for a laminar boundary layer taken from Fig. 13 are shown for comparison; the values of the measured x_i are shown by vertical lines. The theoretical downstream pressures for "regular reflection" are shown on the right; p_1 is free-stream static pressure.

TABLE 1

θ	3°		6°		6°		6°
	600,000		630,000		260,000		120,000
R_i	Model	Exp.	Model	Exp.	Model	Exp.	Model
p_3/p_1	1.10	1.06	1.10	1.12	1.14	1.16	1.20
ϵ_3	2° 22′		2°22′		3°28′		4° 38′
p_4/p_1	1.22	1.20	1.39	1.38	1.43	1.41	1.46
ϵ_4	−1° 5′		−3° 38′		−2° 40′		−2°
M_4	1.84	1.82	1.75		1.67		1.61
p_5/p_1	1.10	1.10	1.10	1.20	1.14	1.16	1.19
ϵ_5	−3° 38′		−9° 36′		−8° 42′		−7° 26′
M_5	1.93	1.90	1.96		1.88		1.80
p_6/p_1	1.27	1.22	1.59	1.54	1.57	1.53	1.57

By and large, the agreement between the parameters calculated according to the model wave pattern and the experimental values suggests that the calculated flow directions of Table 1 are reliable.

Results with Tripped Turbulent Boundary Layer

The results presented in the preceding section were obtained with boundary layers that had formed in a normal manner and which extended into the transition régime (for the highest Reynolds Number). In order to extend the investigation to include turbulent boundary layers, the boundary layer was tripped by a wire glued to the plate surface near the leading edge. The data for this turbulent boundary layer were obtained at a tunnel density equal to that used previously for the case $R_i = 600{,}000$ and $x_i = 1.9$ in.

Fig. 20 is a typical schlieren photograph. The reflected wave consists of a single shock rather than the complicated pattern shown in Fig. 7 for laminar boundary layers. The boundary layer does not thicken appreciably in passing through the interaction region.

The pressure on the plate surface is shown in Fig. 21, together with two curves for a laminar boundary layer for comparison. A single, abrupt rise in pressure is observed at the point of incidence rather than the two successive increments in pressure observed with laminar boundary layers. If the data for laminar boundary layers are extrapolated to higher Reynolds Numbers, they approach the curve observed for a turbulent boundary layer.

Thus, there is a significant difference between the interaction phenomena associated with laminar boundary layers and those associated with turbulent boundary layers. It is not clear whether this difference is due mainly to the fact that the thickness of the subsonic layer is probably less in a turbulent boundary layer than in a laminar boundary layer or whether it is due chiefly to the different shear stress distributions in laminar and turbulent boundary layers.

Conclusions

The experiments described provide insight into the nature of the interaction process. This understanding should be helpful to the designer of supersonic flow equipment.

Since none of the available theories adequately explains the complex shock-boundary-layer interaction, further theoretical work is necessary. The results presented here may serve as a guide to such work.

References

[1] Barry, F. W., Shapiro, A. H., and Neumann, E. P., *Some Experiments on the Interaction of Shock Waves with Boundary Layers on a Flat Plate*, J. Appl. Mech., Vol. 17, No. 2, pp. 126–131, June, 1950. Discussion, J. Appl. Mech., Vol. 17, No. 4, pp. 461–462, December, 1950.

[2] Barry, F. W., *Reflection and Refraction of a Wave in a Mach Number Gradient*, Gas Turbine Laboratory Report No. 7, M.I.T., April, 1950.

[3] Barry, F. W., *Interaction of an Oblique Shock with a Boundary Layer on a Flat Plate*, Sc.D. thesis, Department of Mechanical Engineering, M.I.T., January 7, 1950.

[4] Fage, A., and Sargent, R. F., *Shock-Wave and Boundary-Layer Phenomena Near a Flat Surface*, Proceedings of the Royal Society, Vol. 190, Series A, No. 1020, pp. 1–20, June 17, 1947.

[5] Liepmann, H. W., Ashkenas, H., and Cole, J. D., *Experiments in Transonic Flow*, U.S.A.F. Technical Report 5667, Air Materiel Command, February 9, 1948.

(*Continued on page 270*)

On the One-Dimensional Theory of Flame Structure

RAYMOND FRIEDMAN* AND EDWARD BURKE*

Westinghouse Electric Corporation

ABSTRACT

The dependence of the temperature distribution in a premixed gas flame on burning velocity, flame thickness, heat-release pattern, and the physical properties of the mixture is calculated from the fundamental equations. By an analogous procedure, the local concentration of a chemical species created in the flame is obtained; both distributions are shown to be of the same form. The general equations are solved for a variety of heat-release patterns (or species formation patterns), and numerical values are presented over a wide range of parameters, so that the influence of the pattern on the distributions may be seen. Solutions are obtained both under the assumption of constant transport coefficients—i.e., thermal conductivity and diffusion coefficient—and under the assumption that these coefficients vary with temperature. The results, presented in tabular and graphical form, may be used directly to relate experimental information of reaction-zone thickness, burning velocity, species concentrations, and temperatures in the flame zone. The flame measurements of Wolfhard are discussed in relation to the equations developed in this paper.

NOMENCLATURE

γ = position parameter (dimensionless)
θ = temperature parameter for preheat zone (dimensionless)
λ = thermal conductivity (cal. cm.$^{-1}$ sec.$^{-1}$ °K.$^{-1}$)
ρ = density (Gm. cm.$^{-3}$)
σ = concentration parameter (dimensionless)
τ = temperature parameter (dimensionless)
φ = flame parameter (dimensionless)
Ω = number of collisions per molecule in reaction zone (dimensionless)
C = weight fraction of a species (dimensionless)
C_1, C_2 = constants of integration
D = coefficient of diffusion (cm.^{2} sec.$^{-1}$)
L = reaction zone width (cm.)
$\mathfrak{L}$ = mean free path (cm.)
M = local Mach Number (dimensionless)
Q = heat release rate (cal. cm.$^{-3}$ sec.$^{-1}$)
T = absolute temperature (°K.)
W = rate of species formation (Gm. cm.$^{-3}$ sec.$^{-1}$)
c = mean specific heat at constant pressure (cal. Gm.$^{-1}$ °K.$^{-1}$)
m = temperature exponent of transport coefficient (dimensionless)
s = gas velocity (cm. sec.$^{-1}$)
$\bar{v}$ = mean molecular velocity (cm. sec.$^{-1}$)
x = distance (cm.)

Subscripts

a = average
b = completely burned gas
c = constant transport coefficients
D = concentration gradients and diffusion flow
0 = plane in which reaction commences (except for Case IV)
T = temperature gradients and heat flow
u = unburned gas
v = variable transport coefficients

Received June 1, 1950.

* Research Engineers, Thermodynamics Section, Westinghouse Research Laboratories.

INTRODUCTION

UP TO THE PRESENT, the equations for the structure of one-dimensional, steady-state, premixed gas flames have been derived in four ways:

(A) Rigorous simultaneous differential equations for heat flow and for diffusion flow of each component are formulated.[1]

(B) Heat flow is assumed to be the limiting process, and diffusion is ignored.[2–4]

(C) Diffusion, particularly of free radicals, is assumed to be the limiting process, and heat flow is ignored.[5–8]

(D) Both heat flow and diffusion are considered, but assumptions are made which restrict the generality of the treatment.[9–12]

No one of these approaches has yet been conclusively demonstrated to be applicable to flames of practical interest, although approach (A) offers the most promise of leading to an ultimate solution. For flames such as the hydrogen-bromine and hydrogen-oxygen systems, where the chemical kinetics is moderately well understood, application of this rigorous approach may demonstrate that either heat flow or diffusion can be ignored under certain conditions. However, for hydrocarbon flames even a qualitative knowledge of the chemical mechanisms is lacking, whereas the theory requires quantitative values for the reaction rate constants, as well as for their temperature coefficients. Since an immediate application of the rigorous approach to hydrocarbon flames cannot be expected, it is of interest to develop approaches (B) and (C) as far as possible.

In this paper, approaches (B) and (C) are used to derive the relations between the flame variables in such a way as to be applicable to models based either on heat flow or on diffusion while investigating the influence of various patterns of heat release or of active species formation. Furthermore, solutions are obtained both for the usual assumption of temperature-independent transport properties—e.g., thermal conductivities and

diffusion coefficients—and for a more realistic assumption wherein these coefficients vary with temperature. The results, presented in tabular and graphical form, may be used directly to relate experimental information on reaction-zone thickness, burning velocity, and temperatures and species concentrations in the flame zone.

The following dimensionless parameters will be used:

$$\begin{aligned} \tau &= (T - T_u)/(T_b - T_u) \\ \sigma &= (C - C_u)/(C_b - C_u) \\ \gamma &= x/L \\ \varphi_T &= s_u L c \rho_u/\lambda_0 \\ \varphi_D &= s_u L \rho_u/D_0\rho_0 \\ h &= QL/[s_u\rho_u c\,(T_b - T_u)] \\ j &= WL/[s_u\rho_u\,(C_b - C_u)] \end{aligned}$$

Here, the subscript u refers to the unburned and b to the burned gas; T is temperature; C is weight fraction of a particular species; x is distance (gas flow being in positive x-direction); L is reaction-zone thickness; s_u is burning velocity; λ is thermal conductivity; c is average specific heat at constant pressure; ρ is density; and D is diffusion coefficient of a particular species in the mixture. The reaction is considered to take place between $x = 0$ and $x = L$. If Q denotes the local heat-release rate per unit volume and W the local rate of species formation per unit volume, then the variation of Q with x between $x = 0$ and $x = L$ will be referred to as "the heat-release pattern," appearing in dimensionless form as h, while the variation of W with x in the same region will be referred to as "the species-formation pattern" and appears in dimensionless form as j. The subscript 0 in the definitions refers to the plane $x = 0$.

The steady-state equations for conservation of energy and of mass may be formulated, and explicit solutions may be obtained by assuming an arbitrary dependence of Q or W upon x between 0 and L. When transposed to the dimensionless groups, such solutions will be of the form

$$F(\varphi_T, \tau, \gamma) = 0 \tag{1}$$
$$G(\varphi_D, \sigma, \gamma) = 0 \tag{2}$$

φ, which contains the burning velocity, may be computed only when some value of τ (or σ) other than zero and unity is known. As an example, the τ-value corresponding to $\gamma = 0$, written τ_0, is the temperature at which reaction is represented as beginning, σ_0 being an analogous critical concentration of free radicals or other species required for reaction. Substituting $\gamma = 0$ into the pair of Eqs. (1) and (2) gives

$$F(\varphi_T, \tau_0) = 0 \tag{3}$$
$$G(\varphi_D, \sigma_0) = 0 \tag{4}$$

The Mallard-le Chatelier equation[2] is an example of Eq. (3), while the Gaydon-Wolfhard equation[3] may be shown to be an instance of Eq. (4), when it is recognized that their assumptions are equivalent to $\sigma_0 = 1/e$.

Equations of the forms represented in Eqs. (1) to (4) are obtained in this paper for four heat-release and species-formation patterns. The effect of temperature dependence of λ and $(D\rho)$ is investigated for two of these cases.

General Equations and Boundary Conditions

The steady-state, one-dimensional heat balance may be written

$$\frac{d}{dx}\left(\lambda\frac{dT}{dx}\right) - s\rho c\frac{dT}{dx} + Q = 0 \tag{5}$$

Here, specific heat is assumed constant. The product $s\rho$ is constant by the equation of continuity

$$s\rho = s_u\rho_u = s_b\rho_b \tag{6}$$

The equation for conservation of a particular species may be written[1]

$$\frac{d}{dx}\left(D\rho\frac{dC}{dx}\right) - s\rho\frac{dC}{dx} + W = 0 \tag{7}$$

This equation would be rigorous only if partial pressure were used instead of weight fraction C in the first term, but no appreciable error is introduced if either of the following conditions is fulfilled: (1) if the concentration of the species is small, or (2) if the molecular weight of the species is not far different from the average molecular weight of the mixture.

The following pair of conditions on Q and W may be obtained by integrating Eqs. (5) and (7) between minus infinity and plus infinity and by noting that the first derivatives vanish at these limits:

$$\int_{-\infty}^{\infty} Q\,dx = \int_0^L Q\,dx = s_u\rho_u c\,(T_b - T_u) \tag{8}$$

$$\int_{-\infty}^{\infty} W\,dx = \int_0^L W\,dx = s_u\rho_u(C_b - C_u) \tag{9}$$

These equations may be transformed to a dimensionless basis, yielding

$$\frac{d}{d\gamma}\left(\frac{\lambda}{\lambda_0}\frac{d\tau}{d\gamma}\right) - \varphi_T\frac{d\tau}{d\gamma} + \varphi_T h = 0 \tag{10}$$

$$\frac{d}{d\gamma}\left(\frac{D\rho}{D_0\rho_0}\frac{d\sigma}{d\gamma}\right) - \varphi_D\frac{d\sigma}{d\gamma} + \varphi_D j = 0 \tag{11}$$

$$\int_0^1 h\,d\gamma = 1 \tag{12}$$

$$\int_0^1 j\,d\gamma = 1 \tag{13}$$

Since Eqs. (10) and (12) are strictly analogous to Eqs. (11) and (13), only the equations of heat flow will be carried through from this point. Eq. (10) may be integrated directly to give

$$\frac{\lambda}{\lambda_0}\frac{d\tau}{d\gamma} - \varphi_T\tau + \varphi_T\int h\,d\gamma = C_1 \tag{14}$$

The boundary condition required to evaluate the constant of integration C_1 is obtained from the heat balance across the plane $x = 0$,

$$[\lambda(dT/dx)]_{x=0} = s_u\rho_u c(T_0 - T_u) \tag{15}$$

or, in dimensionless form,

$$(d\tau/d\gamma)_{\gamma=0} = \varphi_T\tau_0 \tag{16}$$

The integration constant is then found from Eqs. (14) and (16) to be given by

$$C_1 = \varphi_T(\int h\, d\gamma)_{\gamma=0} \tag{17}$$

It will be assumed that the transport coefficients in the region where γ is between 0 and 1 may be represented by the relations

$$\lambda/\lambda_0 = 1 + \gamma[(\lambda_b/\lambda_0) - 1] \tag{18}$$

$$D\rho/D_0\rho_0 = 1 + \gamma[(D_b\rho_b/D_0\rho_0) - 1] \tag{19}$$

Upon substitution of Eq. (18) into Eq. (14), the latter may be integrated a second time, yielding

$$\tau = \left(1 + \gamma\frac{\lambda_b}{\lambda_0} - \gamma\right)^{\varphi_T\lambda_0/(\lambda_b-\lambda_0)}\left\{\int \frac{(C_1 - \varphi_T \int h\, d\gamma)d\gamma}{[1 + \gamma\,(\lambda_b/\lambda_0) - \gamma]^{(\lambda_b-\lambda_0+\varphi_T\lambda_0)/(\lambda_b-\lambda_0)}} + C_2\right\} \tag{20}$$

The new constant of integration C_2 is obtained from the boundary condition that $\tau = 1$ at $\gamma = 1$. A strictly analogous equation may be written exhibiting σ as a function of γ, φ_D, j, $D_0\rho_0$, and $D_b\rho_b$.

For the simpler case where the transport coefficient is taken as independent of temperature, Eq. (14) leads to

$$\tau = \exp(\varphi_T\gamma)\left[\int\left(C_1 - \varphi_T\int h\, d\gamma\right)\exp(-\varphi_T\gamma)d\gamma + C_2\right] \tag{21}$$

with an analogous equation for σ.

Equations for Preheat Zone

In the preheat zone ($\gamma < 0$), h and j are defined equal to zero, so that the terms in Eqs. (10) and (11) containing these variables drop out, and solutions are therefore independent of the pattern of heat release or species formation.

When λ is treated as constant, another term drops out of Eq. (10), and the resulting equation is readily integrated, with the boundary conditions $\tau = \tau_0$ at $\gamma = 0$ and $d\tau/d\gamma = \tau = 0$ at $\gamma = -\infty$, to yield

$$d\tau/d\gamma = \varphi_T\tau \tag{22}$$

$$\tau = \tau_0 \exp(\varphi_T\gamma) \tag{23}$$

Similarly,

$$\sigma = \sigma_0 \exp(\varphi_D\gamma) \tag{24}$$

When λ is treated as variable, the first integration of Eq. (10) gives

$$(\lambda/\lambda_0)\,(d\tau/d\gamma) = \varphi_T\tau \tag{25}$$

Similarly,

$$(D\rho/D_0\rho_0)\,(d\sigma/d\gamma) = \varphi_D\sigma \tag{26}$$

In order to integrate Eq. (25), it is necessary to assume a relation between thermal conductivity and temperature. Experimental data for air indicate that the following relation would be satisfactory:

$$\lambda/\lambda_0 = D\rho/D_0\rho_0 = (T/T_0)^{3/4} \tag{27}$$

In Eq. (27), T and T_0 denote absolute temperatures. When Eq. (25) is integrated using the three-quarter power law, it is found that

$$-\varphi_T\gamma = \frac{4}{3}\left[1 - \left(\frac{\theta}{\theta_0}\right)^{3/4}\right] + 2\theta_0^{-3/4}\left\{\tan^{-1}\theta_0^{1/4} - \tan^{-1}\theta^{1/4} + \frac{1}{2}\log\left[\left(\frac{\theta^{1/4}+1}{\theta^{1/4}-1}\right)\left(\frac{\theta_0^{1/4}-1}{\theta_0^{1/4}+1}\right)\right]\right\} \tag{28}$$

where

$$\theta = \frac{\tau(T_b - T_u)}{T_u} + 1 \quad (= T/T_u)$$

$$\theta_0 = \frac{\tau_0(T_b - T_u)}{T_u} + 1 \quad (= T_0/T_u)$$

An analogous solution for Eq. (26) is obtained upon replacement of τ and φ_T in Eq. (28) by σ and φ_D. The latter solution is valid, however, only insofar as the approximation

$$\frac{\tau + [T_u/(T_b - T_u)]}{\tau_0 + [T_u/(T_b - T_u)]} = \frac{\sigma + [T_u/(T_b - T_u)]}{\sigma_0 + [T_u/(T_b - T_u)]} \tag{29}$$

is satisfactory. This approximation is necessary because $D\rho$ is, in a physical sense, a function of temperature, whereas concentration appears as the dependent variable in Eq. (26). The magnitude of the error involved in Eq. (29) may be seen from the following expression obtained from Eqs. (23) and (24), which is valid only for constant λ and $D\rho$:

$$\tau/\tau_0 = (\sigma/\sigma_0)\exp[(\varphi_D - \varphi_T)\gamma] \tag{30}$$

The approximation is seen to be good as long as either $(\varphi_D - \varphi_T)$ or γ is small.

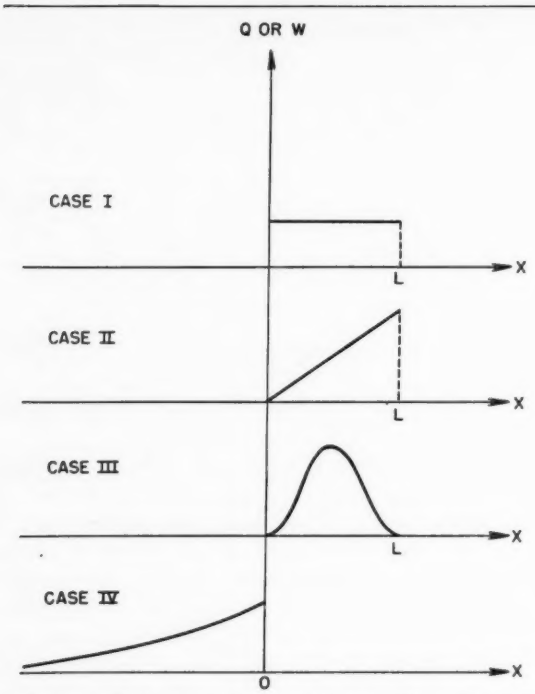

FIG. 1. Heat-release and species formation patterns.

SOLUTIONS FOR VARIOUS HEAT-RELEASE AND SPECIES-FORMATION PATTERNS IN REACTION ZONE

Any analysis of the heat-release pattern demands consideration of the exponential temperature dependence of chemical reaction rates; this suggests an exponentially increasing heat-release pattern in the region $0 < x < L$. However, interdiffusion modifies this distribution, making it less steep. Finally, the heat release would tend to decrease in the downstream portion of the flame, as the reactant concentrations become depleted—i.e., the function must possess a maximum.

The free radical formation pattern is more difficult to predict, since it depends on the specific chain mechanism that is effective. It is even possible that the free radical concentration goes through a maximum because the rate of recombination might exceed the rate of formation in the downstream part of the flame.

The procedure in this paper will be to choose arbitrarily certain forms for the heat-release and species-formation patterns and then to investigate the corresponding relations between the variables. The following cases were chosen and are sketched in Fig. 1:

(I) Q (or W) constant for $0 < x < L$ and zero for $x < 0$ and $x > L$.

(II) Q (or W) directly proportional to x for $0 < x < L$ and zero for $x < 0$ and $x > L$.

(III) Q (or W) directly proportional to $[1 - \cos(2\pi x/L)]$ for $0 < x < L$ and zero for $x < 0$ and $x > L$.

(IV) Q (or W) directly proportional to $\exp(x/L)$ for $-\infty < x < 0$ and zero for $x > 0$.

The symbols Ic, IIc, IIIc, and IVc are used for those cases in which λ or $D\rho$ is assumed to be constant, and the symbols Iv and IIv are used for those cases in which they are assumed to vary with temperature. The proportionality constants introduced in each of these four cases are evaluated from Eqs. (8) and (9). It must be noted that one of the boundary conditions for Case IV is different from the other cases, so that certain minor modifications must be made in the previously derived equations in order to treat this exponential case.

Solutions for the various cases in the reaction zone are listed below. In every case, it is necessary only to replace τ and φ_T by σ and φ_D in order to transform an equation for temperature distribution into the corresponding one for species distribution.

Case Ic.—The general solution of Eq. (21) is found to be

$$\tau = \{1 + \varphi_T\gamma - \exp[-\varphi_T(1 - \gamma)]\}/\varphi_T \quad (31)$$

for $0 < \gamma < 1$, and the solution for $\gamma = 0$ is

$$\tau_0 = [1 - \exp(-\varphi_T)]/\varphi_T \quad (32)$$

It is interesting to compare Eq. (32) with the Mallard-le Chatelier equation,[2] which is, when written in terms of τ_0 and φ_T,

$$\tau_0 = \frac{1}{\varphi_T + 1} = \frac{1 - [1/(\varphi_T + 1)]}{\varphi_T} \quad (33)$$

Case IIc.—The general solution for $0 < \gamma < 1$ is

$$\tau = \frac{2}{\varphi_T^2}\left\{1 + \varphi_T\gamma + \frac{\varphi_T^2\gamma^2}{2} - (\varphi_T + 1)\exp[-\varphi_T(1 - \gamma)]\right\} \quad (34)$$

and the solution for $\gamma = 0$ is

$$\tau_0 = (2/\varphi_T^2)[1 - (\varphi_T + 1)\exp(-\varphi_T)] \quad (35)$$

Case IIIc.—The general solution for $0 < \gamma < 1$ is

$$\tau = \frac{1}{\varphi_T} + \gamma + \left[\frac{\varphi_T}{\varphi_T^2 + 4\pi^2} - \frac{1}{\varphi_T}\right]\exp[-\varphi_T(1 - \gamma)] - \frac{(\varphi_T^2/2\pi)\sin(2\pi\gamma) + \varphi_T\cos(2\pi\gamma)}{\varphi_T^2 + 4\pi^2} \quad (36)$$

and the solution for $\gamma = 0$ is

$$\tau_0 = \left[\frac{\varphi_T}{\varphi_T^2 + 4\pi^2} - \frac{1}{\varphi_T}\right]\left[\exp(-\varphi_T) - 1\right] \quad (37)$$

Case IVc.—Since in this case the reaction zone is infinitely wide, L is defined as the distance in which the function Q (or W) decreases to $1/e$ of its maximum value. The solution for $-\infty < \gamma < 0$ is

$$\tau = \frac{\varphi_T}{\varphi_T - 1}\left[\exp(\gamma) - \frac{1}{\varphi_T}\exp(\varphi_T\gamma)\right] \quad (38)$$

and

$$\tau_{(\gamma=-1)} = \frac{\varphi_T \exp(\varphi_T - 1) - 1}{(\varphi_T - 1)\exp(\varphi_T)} \tag{39}$$

Case Iv.—In the cases where λ varies, a new variable λ_b/λ_0 is involved. The solution of Eq. (20) for $0 < \gamma < 1$ is

$$\tau = \frac{1 + \varphi_T\gamma - \frac{\lambda_b}{\lambda_0}\left[\frac{1 + (\lambda_b/\lambda_0)\gamma - \gamma}{\lambda_b/\lambda_0}\right]^{\varphi_T/[(\lambda_b/\lambda_0)-1]}}{1 + \varphi_T - (\lambda_b/\lambda_0)} \tag{40}$$

and the solution for $\gamma = 0$ is

$$\tau_0 = \frac{1 - (\lambda_b/\lambda_0)^{[(\lambda_b/\lambda_0)-1-\varphi_T]/[(\lambda_b/\lambda_0)-1]}}{1 + \varphi_T - (\lambda_b/\lambda_0)} \tag{41}$$

The ratio λ_b/λ_0 may be expressed in terms of τ_0 as follows:

$$\frac{\lambda_b}{\lambda_0} = \frac{D_b\rho_b}{D_0\rho_0} = \left(\frac{T_b}{T_0}\right)^{2/4} = \left\{\frac{[T_u/(T_b - T_u)] + 1}{[T_u/(T_b - T_u)] + \tau_0}\right\}^{2/4} \tag{42}$$

Plotting Eqs. (41) and (42) over the range of the variables makes it possible to eliminate λ_b/λ_0 between the two plots by preparing a third plot relating φ_T, τ_0, and $T_u/(T_b - T_u)$. It may be noted that, for actual flames, $T_u/(T_b - T_u)$ is almost always between 0.075 and 0.5.

The corresponding relations between φ_D, σ, and $D_b\rho_b \div D_0\rho_0$ are seen to be rigorous only when $\tau_0 = \sigma_0$ because of the dependence of $D\rho$ on τ_0 instead of on σ_0 in Eq. (42); fortunately, only small errors are introduced when σ_0 differs moderately from τ_0.

Case IIv.—The solution for $0 < \gamma < 1$ is

$$\tau = \left(\frac{1 + \gamma\frac{\lambda_b}{\lambda_0} - \gamma}{\lambda_b/\lambda_0}\right)^{\varphi_T/[(\lambda_b/\lambda_0)-1]}\left\{1 - \frac{1}{\left(\frac{\lambda_b}{\lambda_0} - 1\right)^2}\left[1 + \frac{2\frac{\lambda_b}{\lambda_0}\varphi_T}{\frac{\lambda_b}{\lambda_0} - 1 - \varphi_T} - \frac{\left(\frac{\lambda_b}{\lambda_0}\right)^2\varphi_T}{2\frac{\lambda_b}{\lambda_0} - 2 - \varphi_T}\right]\right\} + \frac{1}{\left(\frac{\lambda_b}{\lambda_0} - 1\right)^2}\left\{1 + \frac{2\left(1 + \gamma\frac{\lambda_b}{\lambda_0} - \gamma\right)\varphi_T}{\frac{\lambda_b}{\lambda_0} - 1 - \varphi_T} - \frac{\left(1 + \gamma\frac{\lambda_b}{\lambda_0} - \gamma\right)^2\varphi_T}{2\frac{\lambda_b}{\lambda_0} - 2 - \varphi_T}\right\} \tag{43}$$

and, when $\gamma = 0$,

$$\tau_0 = \left(\frac{\lambda_0}{\lambda_b}\right)^{\varphi_T/[(\lambda_b/\lambda_0)-1]}\left\{1 - \frac{1}{\left(\frac{\lambda_b}{\lambda_0} - 1\right)^2}\left[1 + \frac{2\frac{\lambda_b}{\lambda_0}\varphi_T}{\frac{\lambda_b}{\lambda_0} - 1 - \varphi_T} - \frac{\left(\frac{\lambda_b}{\lambda_0}\right)^2\varphi_T}{2\frac{\lambda_b}{\lambda_0} - 2 - \varphi_T}\right]\right\} + \frac{1}{\left(\frac{\lambda_b}{\lambda_0} - 1\right)^2}\left\{1 + \frac{2\varphi_T}{\frac{\lambda_b}{\lambda_0} - 1 - \varphi_T} - \frac{\varphi_T}{2\frac{\lambda_b}{\lambda_0} - 2 - \varphi_T}\right\} \tag{44}$$

The comments concerning Case Iv also apply here.

Discussion of Results

Numerical values have been computed over a wide range of the variables for each of the above equations and are given in Table 1. It may be noted that the equations generally become indeterminate at $\varphi_T = 0$. However, in each case, by a suitable expansion in series, it may be shown that the limit of τ_0 as φ_T approaches 0 is 1. The details will not be presented.

Fig. 2 shows the solution for Case Ic; all of the other cases possess solutions of this same general form. The shape of the curve for $\gamma = 0$ reveals the inverse nature of the relation between τ_0 and φ_T. As previously noted, the curves in Fig. 2 also express the relation between σ and φ_D.

The solution is again shown in Fig. 3, where curves of constant φ are plotted instead of constant γ; this plot shows the gradient through the flame. Figs. 4 through 8 are analogous to Fig. 3, except that they represent Cases IIc, IIIc, IVc, Iv, and IIv, respectively.

A comparison of Cases Ic, IIc, and IIIc is given in Fig. 9 showing φ_T vs. τ_0 at $\gamma = 0$. For a given value of φ_T, it may be seen that Case Ic yields the highest, and Case IIc the lowest, value of τ_0. The solution of the

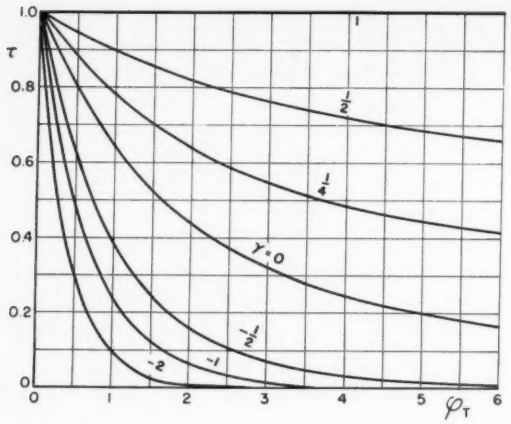

FIG. 2. Case Ic. Plot of τ vs. φ_T for various values of γ.

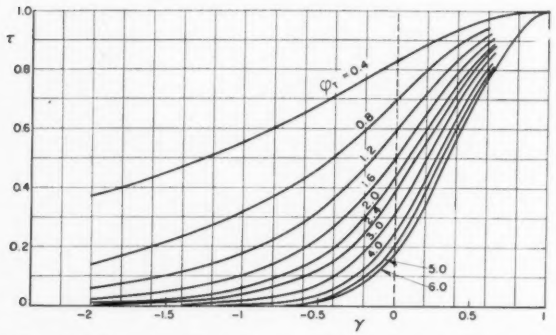

FIG. 3. Case Ic. Plot of τ vs. γ for various values of φ_T.

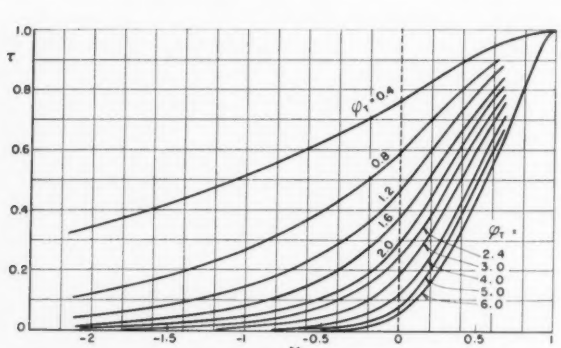

FIG. 4. Case IIc. Plot of τ vs. γ for various values of φ_T.

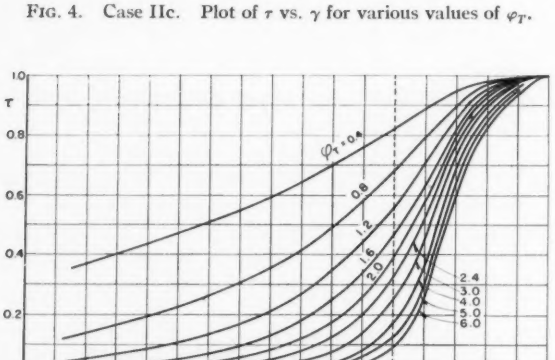

FIG. 5. Case IIIc. Plot of τ vs. γ for various values of φ_T.

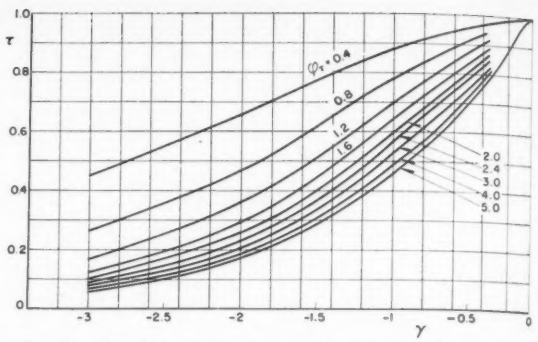

FIG. 6. Case IVc. Plot of τ vs. γ for various values of φ_T.

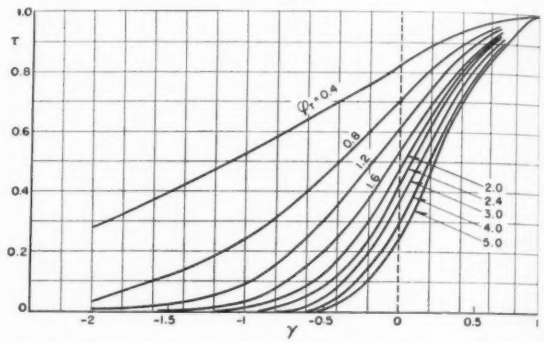

FIG. 7. Case Iv. Plot of τ vs. γ for various values of φ_T. $T_w(T_b - T_w) = 0.14$.

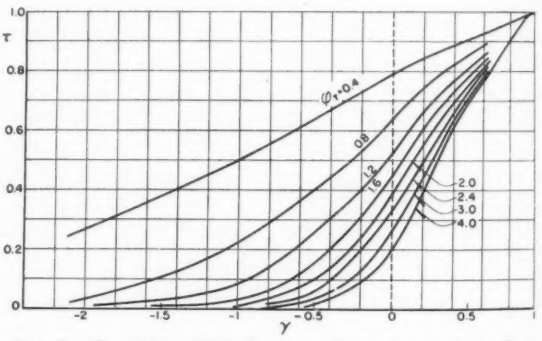

FIG. 8. Case IIv. Plot of τ vs. γ for various values of φ_T. $T_w/(T_b - T_w) = 0.14$.

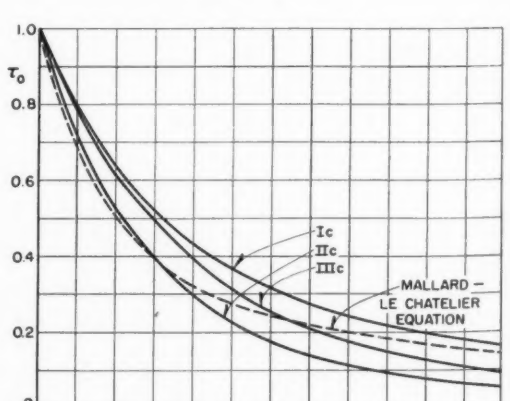

FIG. 9. Comparison of Cases Ic, IIc, and IIIc at $\gamma = 0$.

TABLE 1
Values of τ for the Various Cases

Case	$\frac{T_u}{T_b - T_u}$	γ \ φ_T	0	0.4	0.8	1.2	1.6	2.0	2.4	3.0	4.0	5.0	6.0
Ic	...	−2	1.000	0.371	0.140	0.053	0.020	0.008	0.003	0.001	0.000	0.000	0.000
		−1	1.000	0.555	0.312	0.176	0.100	0.059	0.035	0.016	0.004	0.001	0.000
		−0.5	1.000	0.678	0.465	0.320	0.223	0.160	0.115	0.070	0.033	0.016	0.008
		0	1.000	0.828	0.695	0.584	0.497	0.434	0.382	0.317	0.243	0.197	0.163
		0.25	1.000	0.904	0.818	0.744	0.688	0.638	0.593	0.543	0.482	0.442	0.414
		0.5	1.000	0.956	0.915	0.879	0.846	0.816	0.790	0.758	0.719	0.686	0.659
IIc	...	−2	1.000	0.342	0.120	0.042	0.015	0.005	0.002	0.000	0.000	0.000	0.000
		−1	1.000	0.511	0.267	0.140	0.075	0.040	0.022	0.009	0.002	0.001	0.000
		−0.5	1.000	0.625	0.398	0.256	0.166	0.109	0.073	0.040	0.015	0.006	0.003
		0	1.000	0.763	0.595	0.466	0.371	0.297	0.242	0.179	0.114	0.077	0.054
		0.25	1.000	0.844	0.726	0.632	0.551	0.480	0.422	0.358	0.285	0.234	0.198
		0.5	1.000	0.924	0.857	0.796	0.744	0.701	0.658	0.605	0.540	0.491	0.451
IIIc	...	−2	1.000	0.369	0.137	0.051	0.019	0.007	0.003	0.001	0.000	0.000	0.000
		−1	1.000	0.551	0.304	0.169	0.095	0.053	0.030	0.013	0.003	0.001	0.000
		−0.5	1.000	0.674	0.454	0.307	0.211	0.144	0.098	0.057	0.023	0.010	0.005
		0	1.000	0.823	0.677	0.560	0.470	0.392	0.327	0.256	0.174	0.126	0.093
		0.25	1.000	0.904	0.820	0.751	0.679	0.638	0.588	0.528	0.444	0.386	0.339
		0.5	1.000	0.970	0.943	0.920	0.898	0.879	0.860	0.836	0.798	0.763	0.735
IVc	...	−3	1.000	0.455	0.265	0.166	0.121	0.103	0.090	0.077	0.063	0.060	...
		−2	1.000	0.658	0.469	0.360	0.291	0.253	0.228	0.200	0.180	0.169	...
		−1	1.000	0.881	0.781	0.701	0.643	0.599	0.565	0.530	0.489	0.460	...
		−0.5	1.000	0.967	0.936	0.904	0.876	0.849	0.824	0.792	0.752	0.730	...
Iv	0.14	−2	1.000	0.280	0.021	...	...	...	...	...	...	...	...
	0.14	−1	1.000	0.518	0.239	0.093	0.031	...	...	...	...	...	...
	0.14	−0.5	1.000	0.666	0.438	0.291	0.188	0.119	0.072	0.038	...	...	...
	0.1	0	1.000	0.824	0.700	0.611	0.540	0.476	0.428	0.370	0.300	0.249	...
	0.3	0	1.000	0.821	0.694	0.605	0.531	0.468	0.418	0.359	0.288	0.236	...
	0.5	0	1.000	0.818	0.688	0.599	0.522	0.460	0.408	0.349	0.276	0.223	...
	0.14	0.25	1.000	0.908	0.832	0.776	0.730	0.691	0.658	0.621	0.570	0.532	...
	0.14	0.5	1.000	0.960	0.927	0.900	0.876	0.858	0.841	0.819	0.792	0.780	...
IIv	0.14	−2	1.000	0.267	0.028	...	...	...	...	...	...	...	...
	0.14	−1	1.000	0.492	0.218	0.081	0.031	...	...	...	...	...	...
	0.14	−0.5	1.000	0.633	0.398	0.248	0.157	0.101	0.060	0.031	...	...	...
	0.1	0	1.000	0.790	0.635	0.521	0.439	0.378	0.328	0.269	0.196	...	...
	0.3	0	1.000	0.784	0.625	0.509	0.427	0.365	0.314	0.251	0.173	...	...
	0.5	0	1.000	0.778	0.615	0.497	0.415	0.353	0.300	0.234	0.151	...	...
	0.14	0.25	1.000	0.870	0.779	0.708	0.644	0.589	0.533	0.482	0.434	...	...
	0.14	0.5	1.000	0.910	0.850	0.809	0.779	0.752	0.733	0.713	0.700	...	...

Mallard-le Chatelier equation is shown to be reasonably close to that of Case IIc for φ_T less than 2.

Figs. 10 and 11 show comparisons of the results obtained according to assumptions of constant and variable transport properties for τ_0 as a function of φ_T; Case I is treated in Fig. 10 and Case II in Fig. 11. It will be observed that a family of curves appears for each of the variable cases corresponding to the previously discussed parameter $T_u/(T_b - T_u)$. The curves are seen to be insensitive to the value of $T_u \div (T_b - T_u)$. For a given φ, an increase in this parameter corresponds to a slight decrease in τ_0.

Of the various flame parameters occurring in the treatment, fairly good experimental data are available for s_u, λ, ρ_u, c, and T_b. However, few values, and these of uncertain reliability, have been reported for L and T_0 and none at all for concentrations of active species except in the region $\gamma > 1$.

Values for L and T_0 are given by Wolfhard, et al.,[8, 13] for a lean acetylene-oxygen flame at 4.3 mm. Hg. The consistency of these measurements may be determined by comparison with the previously developed relations between φ_T and τ_0. From Wolfhard's results, T_0 = 800°C., T_b = 2,950°C., and T_u = 30°C., so that τ_0 is found to be 0.26. To compute φ_T, values must be obtained for λ_0, ρ_u, c, L, and s_u. The first three quantities were computed by averaging published data for acetylene and oxygen. L is taken to be 12 mm., the value given for the total thickness of the luminous zone. The value of s_u was estimated as recommended by Wolfhard[14] by considering the flame to be flat and equal in diameter to the burner tube; since the volumetric flow is given, s_u may be computed then to be

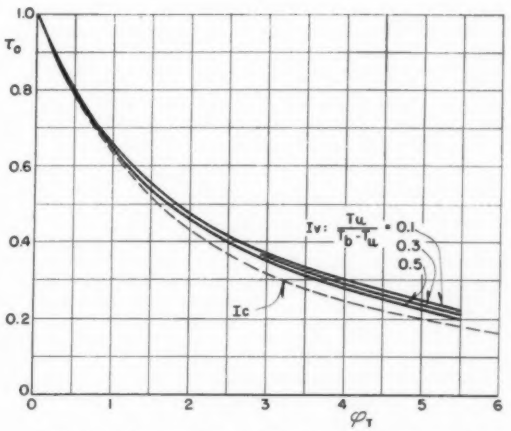

FIG. 10. Comparison of Cases Ic and Iv at $\gamma = 0$.

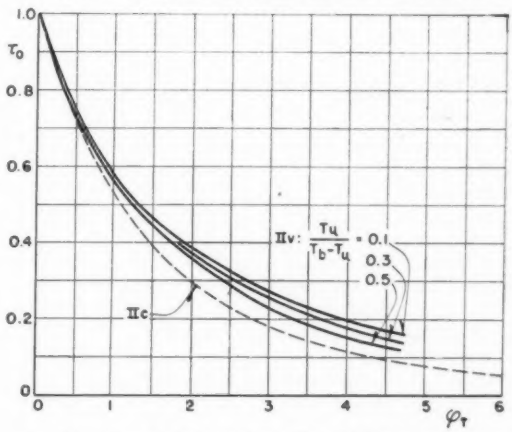

FIG. 11. Comparison of Cases IIc and IIv at $\gamma = 0$.

260 cm. per sec. Utilizing these values, φ_T is found to be 3.8.

From Figs. 10 and 11, corresponding to Cases Iv and IIv, values of τ_0 corresponding to the above φ_T are found to be 0.31 and 0.21, respectively, with $T_u/(T_b - T_u) = 0.10$. The values of $\tau_0 = 0.31$ for Case Iv and $\tau_0 = 0.21$ for Case IIv may be compared with the experimental value of $\tau_0 = 0.26$. Since Cases Iv and IIv probably represent two extreme forms for the heat release, the values of T_0 and L given by Wolfhard, et al., seem to be mutually consistent.

Values of T_0 and reaction zone thickness have been determined from spark ignition energies by Lewis and von Elbe.[15] This topic has been discussed in a previous note by the writers.[16]

When more precise measurements are made for a variety of flames, the relations developed in this paper will aid in the understanding of the mechanism of combustion.

References

[1] Hirschfelder, J. O., and Curtiss, C. F., *The Theory of Flame Propagation*, J. Chem. Physics, Vol. 17, pp. 1076–1081, 1949.

[2] Lewis, B., and von Elbe, G., *Combustion, Flames and Explosions of Gases;* Cambridge, 1938.

[3] Jost, W., *Explosion and Combustion Processes in Gases;* McGraw-Hill Book Company, Inc., New York, 1946.

[4] Boys, S. F., and Corner, J., *The Structure of the Reaction Zone in a Flame*, Proc. Royal Soc., Vol. A197, pp. 90–106, 1949.

[5] Jost, W., and von Muffling, L., *Flame Velocity. I. The Possibility of Theoretically Calculating Flame Velocities*, Z. physik. Chem., Vol. A181, pp. 208–214, 1938.

[6] Tanford, C., and Pease, R. N., *Theory of Burning Velocity. II. The Square Root Law for Burning Velocity*, J. Chem. Physics, Vol. 15, pp. 861–865, 1947.

[7] Hoare, M. F., and Linnett, J. W., *The Mechanism of Flame Propagation*, J. Chem. Physics, Vol. 16, pp. 747–749, 1948.

[8] Gaydon, A. G., and Wolfhard, H. G., *The Influence of Diffusion on Flame Propagation*, Proc. Royal Soc., Vol. A196, pp. 105–113, 1949.

[9] Lewis, B., and von Elbe, G., *On the Theory of Flame Propagation*, J. Chem. Physics, Vol. 2, pp. 537–546, 1934.

[10] Zeldovich, Y. B., and Frank-Kamenetsky, D. A., *A Theory of Thermal Propagation of Flame*, Acta Physicochim U.R.S.S., Vol. 9, pp. 341–350; 1938. Also see Semenov, N., *Thermal Theory of Combustion and Explosion. III. Theory of Normal Flame Propagation*, N.A.C.A. T.M. No. 1026, September, 1942.

[11] Corner, J., *The Effect of Diffusion of the Main Reactants on Flame Speeds in Gases*, Proc. Royal Soc., Vol. A198, pp. 388–406, 1949.

[12] Bechert, K., *On the Theory of Burning Velocity, with an Application to Ozone Combustion*, Ann. der Physik, Vol. 4, pp. 191–230, 1949.

[13] Klaukens, H., and Wolfhard, H. G., *Measurements in the Reaction Zone of a Bunsen Flame*, Proc. Royal Soc., Vol. A193, pp. 512–524, 1948.

[14] Wolfhard, H. G., private communication, September, 1949.

[15] Lewis, B., and von Elbe, G., *Ignition of Explosive Gas Mixtures by Electric Sparks. II. Theory of the Propagation of Flame from an Instantaneous Point Source of Ignition*, J. Chem. Physics, Vol. 15, pp. 803–808, 1947.

[16] Friedman, R., and Burke, E., *Spark Ignition of Gas Mixtures*, J. Chem. Physics, Vol. 17, p. 667, 1949.

Appendix

Molecular Interpretation of the Results

From the kinetic theory of gases,

$$\lambda/c\rho_a \simeq D \simeq \bar{v}\mathfrak{L} \tag{45}$$

where ρ_a is an average density, $\mathfrak{L}$ is mean free path, and $\bar{v}$ is mean molecular speed. From Eq. (45) and the relation $s_a\rho_a = s_u\rho_u$, it follows that

$$s_a/\bar{v} \simeq \varphi\ (\mathfrak{L}/L) \tag{46}$$

But $s_a/\bar{v} \simeq M$, so that

$$M \simeq \varphi(\mathfrak{L}/L) \tag{47}$$

This interesting equation states that the local Mach Number M of a flame is always far below unity, since the mean free path is small compared with the flame thickness—i.e., only a small fraction of the molecular collisions in a flame lead to reaction. This concept may be developed further: The number of collisions undergone by a molecule traversing the reaction zone, to be denoted by Ω, is given by the product of collision rate $(\bar{v}/\mathfrak{L})$ and residence time (L/s_a). Thus,

$$\Omega = \bar{v}L/s_a\mathfrak{L} \tag{48}$$

A combination of Eqs. (45), (47), and (48) yields

$$M \simeq \sqrt{\varphi/\Omega} \tag{49}$$

The term $1/\Omega$ is a measure of the probability that any particular collision of a reactant molecule with any other molecule will be the critical collision producing reaction. The term φ is seen from Figs. 10 and 11 to be near unity as long as τ_0 is near 0.5. Thus, the Mach Number of the flame is of the same magnitude as the square root of the reaction probability.

It must be noted that the residence time upon which Eq (49) is based is no longer accurately given by L/s_a when the molecule in question is consumed by reaction. The following reasons are given for this: (1) The molecule will react before traveling the entire distance L, so that $L/2$ should be used for Case I and Case III flames and $L/\sqrt{2}$ for Case II flames. (2) The reactant molecule will possess a diffusion velocity in the downstream direction superimposed upon the gas velocity. The magnitude of this latter effect may be estimated. Such an estimate, based on Case I, shows that, for $\varphi_T = 1$, the velocity of reactant molecules is about three times the average velocity. Thus, both of these effects act to make the originally calculated residence time and, therefore, Ω too large. More refined calculations would give further insight into the physical processes taking place.

The Laminar Boundary Layer on a Rotating Blade*

LAURENCE EUGENE FOGARTY†
Cornell University

SUMMARY

Boundary-layer equations of motion for a blade rotating steadily in an incompressible fluid are developed. The equations show that, at stations several chord lengths from the axis of rotation of a thin blade, the chordwise velocity is independent of the spanwise velocity due to rotation; hence, the separation line is unaffected by rotation. The detailed calculation of the spanwise velocity distribution in the boundary layer is carried out for two examples. Spanwise velocities in the boundary layer are found to be small compared with chordwise velocities. No large effects of rotation are found.

INTRODUCTION

ALTHOUGH THE BOUNDARY-LAYER THEORY formulated by L. Prandtl in 1904 is of great importance in practical aerodynamics, the difficulties presented by the nonlinear boundary-layer equations have limited the classes of solutions to flows of special symmetry. Most of the cases that have been treated to date are two-dimensional in character; solutions of three-dimensional boundary-layer flows are rare.

One of the practically important types of three-dimensional boundary-layer flows is the flow on rotating blades, such as turbine, helicopter, and propeller blades. In this case, the centrifugal and Coriolis forces due to rotation, combined with the pressure gradients and viscous forces, cause the flow to be three-dimensional even in the absence of effects of finite span. von Kármán's solution of the problem of an infinite rotating disc[1] is probably the only solution of a problem of this type.

As part of a program of investigation of three-dimensional boundary-layer flows, the laminar flow over a rotating cylindrical blade is treated here. Although the present investigation deals only with that portion of a blade of infinite span which is several chord lengths from the axis of rotation, it is believed that the results are of considerable interest. The results should be directly applicable, to good approximation, over a large portion of the span of high-aspect-ratio blades. Furthermore, it appears that treatment of the problem of a finite blade, or of a blade in the presence of a wall, for example, will make use of the results of the present investigation.

Received July 31, 1950.

* Based on a Ph.D. thesis presented to the Graduate School of Cornell University in July, 1950. The author acknowledges the guidance and assistance of Prof. W. R. Sears, of the Graduate School of Aeronautical Engineering, Cornell University.

† Now, Aerodynamicist, Aerophysics Laboratory, North American Aviation, Inc.

(I) BOUNDARY-LAYER EQUATIONS

The time variation can be eliminated from the Navier-Stokes equations by fixing the axes with respect to the rotating blade. Let the Z axis be taken along the axis of rotation, the Y axis along the span of the blade, and the X axis so as to form a right-handed Cartesian system (see Fig. 1). The Navier-Stokes equations for steady motion referred to the rotating reference frame are[2]

$$u'u_X' + v'u_Y' + w'u_Z' - 2v'R - XR^2 = -(1/\rho)p_X + \nu(u_{XX}' + u_{YY}' + u_{ZZ}') \quad (1)$$

$$u'v_X' + v'v_Y' + w'v_Z' + 2u'R - YR^2 = -(1/\rho)p_Y + \nu(v_{XX}' + v_{YY}' + v_{ZZ}') \quad (2)$$

$$u'w_X' + v'w_Y' + w'w_Z' = -(1/\rho)p_Z + \nu(w_{XX}' + w_{YY}' + w_{ZZ}') \quad (3)$$

$$u_X' + v_Y' + w_Z' = 0 \quad (4)$$

Here, u', v', and w' are the velocity components in the directions of the rotating axes, X, Y, and Z, respectively; R is the angular velocity of the blade; ρ is the density; p is the pressure; and ν is the kinematic viscosity.

Following Goldstein,[3] one introduces boundary-layer coordinates (Fig. 1) in which x is a curvilinear coordinate parallel to the blade surface, z is normal to the blade surface, and the x-z plane is normal to the blade leading edge, which is taken as the y axis. For those parts of the blade where the radius of curvature is large and nearly constant and where the angle between the z axis and the axis of rotation is small, the equations of motion are

$$uu_x + vu_y + wu_z - 2vR - xR^2 = -(1/\rho)p_x + \nu(u_{xx} + u_{yy} + u_{zz}) \quad (5)$$

$$uv_x + vv_y + wv_z + 2uR - yR^2 = -(1/\rho)p_y + \nu(v_{xx} + v_{yy} + v_{zz}) \quad (6)$$

$$uw_x + vw_y + ww_z = -(1/\rho)\,p_z + \nu(w_{xx} + w_{yy} + w_{zz}) \quad (7)$$

$$u_x + v_y + w_z = 0 \quad (8)$$

If the usual boundary-layer approximations for fluids of small viscosity are made in these equations, the boundary-layer equations of motion referred to the

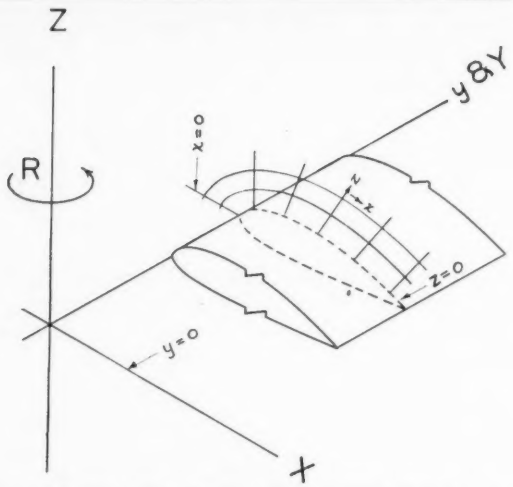

FIG. 1. Sketch showing boundary-layer coordinate system on rotating blade.

rotating coordinate system result:

$$uu_x + vu_y + wu_z - 2vR - xR^2 = -(1/\rho)p_x + \nu u_{zz} \quad (9)$$

$$uv_x + vv_y + wv_z + 2uR - yR^2 = -(1/\rho)p_y + \nu v_{zz} \quad (10)$$

$$p_z = 0 \quad (11)$$

$$u_x + v_y + w_z = 0 \quad (12)$$

The boundary conditions are that there be no fluid velocity relative to the surface at the surface and that the flow approach the potential flow far from the surface.

$$\left.\begin{array}{ll} u = v = w = 0, & z = 0 \\ \left.\begin{array}{l} u \to u_1 \\ v \to v_1 \\ w \to w_1 \end{array}\right\} & z \to \infty \end{array}\right\} \quad (13)$$

where u_1, v_1, w_1 are the velocities in the potential flow.

It has been shown by Sears[4] that the external flow over a rotating cylindrical blade is given by

$$\left.\begin{array}{l} u_1 = YR\varphi_{1X}(X, Z) \\ v_1 = R[\varphi_1(X, Z) - 2X] \\ w_1 = YR\varphi_{1Z}(X, Z) \end{array}\right\} \quad (14)$$

where $\varphi_1(X, Z)$ denotes the potential for plane, steady flow past the cylinder placed in a parallel stream of unit speed in the X direction. The assumption is made that the relative orders of magnitude of the spanwise and chordwise velocities in the boundary layer are determined by the external flow. For example, since the blade was assumed to be thin when Eqs. (5), (6), (7), and (8) were obtained, the potential velocities can be written:

$$u_1 = yR + u_1'', \quad v_1 = -xR + v_1''$$

where the perturbation velocities u_1'' and v_1'' are small in comparison with yR. Therefore, $v_1/u_1 = O(x/y)$, or, taking the maximum value of x to be the chord, c,

$$v_1/u_1 = O(c/y)$$

The assumption mentioned above is that

$$v/u = O(v_1/u_1) = O(c/y)$$

Similarly, by examining the potential velocities (14), it is seen that

$$u_y = O(u/y), \quad u_x = O(u/c), \quad \text{etc.}$$

The relative orders of magnitude of the terms of the boundary-layer Eqs. (9), (10), and (12) have been examined and are shown in the following scheme. The term uu_x is arbitrarily taken to be of unit order of magnitude.

$$\underset{(1)}{uu_x} + \underset{(c/y)^2}{vu_y} + \underset{(1)}{wu_z} - \underset{(c/y)^2}{2vR} - \underset{(c/y)^2}{xR^2} = -\underset{(1)}{(1/\rho)P_x} + \underset{(1)}{\nu u_{zz}} \quad (15)$$

$$\underset{(c/y)}{uv_x} + \underset{(c/y)^3}{vv_y} + \underset{(c/y)}{wv_z} + \underset{(c/y)}{2uR} - \underset{(c/y)}{yR^2} = -\underset{(c/y)}{(1/\rho)p_y} + \underset{(c/y)}{\nu v_{zz}} \quad (16)$$

$$\underset{(1)}{u_x} + \underset{(c/y)^2}{v_y} + \underset{(1)}{w_z} = 0 \quad (17)$$

For stations far out on the blade such that $(c/y)^2 \ll 1$, the approximation is made that terms of relative order of magnitude $(c/y)^2$ can be neglected.

$$uu_x + wu_z = -(1/\rho)p_x + \nu u_{zz} \quad (18)$$

$$uv_x + wv_z + 2uR - yR^2 = -(1/\rho)p_y + \nu v_{zz} \quad (19)$$

$$p_z = 0 \quad (20)$$

$$u_x + w_z = 0 \quad (21)$$

The pressure gradients p_x, p_y, are calculated from the Bernoulli equation for this case:[4]

$$(p/\rho) + (1/2)(u_1^2 + v_1^2) = (R^2/2)(x^2 + y^2) + \text{const.} \quad (22)$$

(w_1 vanishes in this coordinate system.)

$$p_x/\rho = xR^2 - u_1u_{1x} - v_1v_{1x} \tag{23}$$

$$p_y/\rho = yR^2 - u_1u_{1y} \tag{24}$$

The term v_1v_{1x} is of relative order of magnitude $(c/y)^2$, as is the term xR^2, which would cancel the similar term in Eq. (15) in any case.

The equations of motion now read

$$uu_x + wu_z = u_1u_{1x} + \nu u_{zz} \tag{25}$$

$$uv_x + wv_z + 2uR = u_1u_{1y} + \nu v_{zz} \tag{26}$$

$$u_x + w_z = 0 \tag{27}$$

The boundary conditions are

$$\left.\begin{aligned} &u = v = w = 0, && z = 0 \\ &u \to yR\varphi_{1x}(x) \\ &v \to R[\varphi_1(x) - 2x] && z \to \infty \\ &w \to 0 \end{aligned}\right\} \tag{28}$$

Notice that Eqs. (25) and (27), together with the boundary conditions (28) on u and w, are precisely the same as if the flow were two-dimensional with free-stream velocity yR in the positive X direction. Therefore, Eqs. (25) and (27) and their boundary conditions can be solved by any of the methods available for solving two-dimensional laminar boundary-layer problems, and, with u and w known, the linear equation for v can be solved separately.

This behavior of the flow is similar to that found by Prandtl,[5] Jones,[6] and Sears[7] for the case of the yawed infinite wing. In particular, as for the case of the yawed wing, it is clear that rotation of the blade does not affect the position of the line of separation of the chordwise flow component from the surface.

Notice also that, if the blade is being translated along the axis of rotation, the equations of motion are not changed, and the translation appears only in the boundary conditions. It has been shown by Fogarty and Sears[8] that the potential flow over a rotating cylindrical blade that is being translated along the axis of rotation with speed W is given by

$$\left.\begin{aligned} u_1 &= YR\varphi_{1X} + W\varphi_{2X} \\ v_1 &= R(\varphi_1 - 2X) \\ w_1 &= YR\varphi_{1Z} + W\varphi_{2Z} \end{aligned}\right\} \tag{29}$$

where $\varphi_1(X, Z)$ and $\varphi_2(X, Z)$ are the potentials for plane steady flow past the cylinder in a parallel stream of unit speed in the positive X and negative Z directions, respectively. If $W/yR \ll 1$, $W/yR = O(c/y)^2$ say, the effect of the translation may be neglected in this approximation. Thus, the solutions of Eqs. (25)–(27) will apply to rotating cylindrical blades and also to blades of constant cross section lying in the helix generated by steady rotation and translation of the blade, provided that $W/yR = O(c/y)^2$.

In this paper, the application of the theory to the calculation of spanwise flow in the boundary layer will first be illustrated by means of two cases for which the two-dimensional boundary-layer flow is known. These are, respectively, the flat plate and a certain symmetrical cylinder. For these cases, the solutions of Eqs. (25) and (27) are available, and it remains only to construct solutions to Eq. (26). Following this, the treatment of more general cases will be discussed briefly.

(II) The Rotating Plate

Consider a flat plate of chord c and infinite span rotating steadily with angular velocity R about the Z axis. For this case, the potential flow is

$$u_1 = yR, \quad v_1 = -xR, \quad w_1 = 0 \tag{30}$$

The equations of motion are

$$uu_x + wu_z = \nu u_{zz} \tag{31}$$

$$uv_x + wv_z + 2uR - yR^2 = \nu v_{zz} \tag{32}$$

$$u_x + w_z = 0 \tag{33}$$

and the boundary conditions are

$$\left.\begin{aligned} &u \to yR \\ &v \to -xR && z \to \infty \\ &w \to 0 \\ &u = v = w = 0, && z = 0 \end{aligned}\right\} \tag{34}$$

Eqs. (31) and (33) and the boundary conditions (34) on u and w were solved by Blasius,[9] who introduced a function $F(\tau)$ such that

$$\left.\begin{aligned} u &= yR[F'(\tau)/2] \\ w &= (Re)^{-1/2}yR\left[\frac{-F(\tau)}{2\sigma^{1/2}} + \frac{\tau F'(\tau)}{2\sigma^{1/2}}\right] \end{aligned}\right\} \tag{35}$$

where

$$\left.\begin{aligned} \tau &= (1/2)[(Re)^{1/2}(z/c)/(x/c)^{1/2}] \\ Re &= yRc/\nu \\ \sigma &= x/c \end{aligned}\right\} \tag{36}$$

If the above expressions are substituted for u and w in Eq. (32) and the assumption is made that

$$v = xRG(\tau) \tag{37}$$

the following ordinary differential equation for G results:

$$G'' + FG' - 2F'G = 4(F' - 1) \tag{38}$$

The boundary conditions are

$$\left.\begin{aligned} G &= 0, && \tau = 0 \\ G &\to -1, && \tau \to \infty \end{aligned}\right\} \tag{39}$$

Only tabular values of F and F' are known, so it is necessary to solve Eq. (38) numerically over the range $0 \leq \tau \leq \infty$. The tabular values of F' show $F' \backsimeq 2$, $4 \leq \tau \leq \infty$. We see that the solution of Eq. (38) which satisfies the boundary condition $G \to -1$, $\tau \to \infty$ is

$$G = -1, \qquad 4 \leq \tau \leq \infty \tag{40}$$

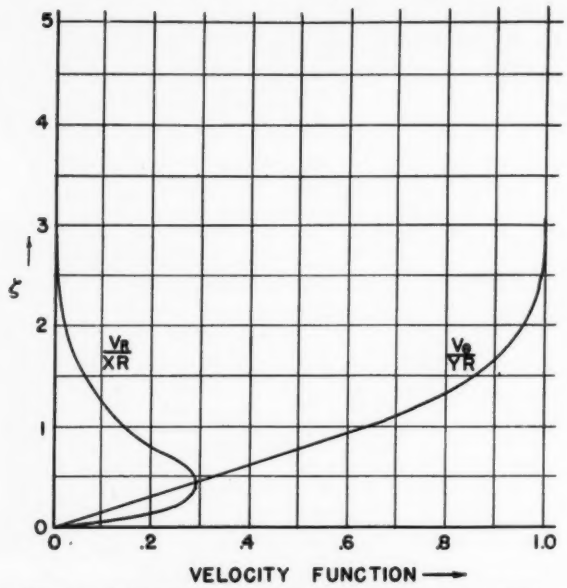

FIG. 2. Velocity profiles in the boundary layer of a rotating flat plate. v_r and v_θ denote the radial and tangential components of the velocity relative to the plate. x denotes the distance from the leading edge, y the radius, and R the angular velocity. ζ is the dimensionless distance from the plate, defined in Eq. (49). NOTE: For V_R/XR and V_θ/YR in this figure, read v_r/xR and v_θ/yR, respectively.

We therefore approximate to the actual boundary condition $G \to -1$, $\tau \to \infty$ by taking $G = -1$, $\tau \geq 4$, and solve Eq. (38) numerically over the range $0 \leq \tau \leq 4$.

The equation for G was integrated numerically over the range $0 \leq \tau \leq 4$. Since the calculated velocities are referred to the rotating Cartesian coordinate system, the results are apt to be confusing to an unwary reader. For greater ease of interpretation, plots of radial and tangential velocities, rather than spanwise and chordwise velocities, are presented. If the angle between the y axis and the radius vector to the point x, y on the blade is small,

$$v_r \approx v + (x/y)u$$
$$v_\theta \approx u$$

The quantities v_r/xR and v_θ/yR are plotted in Fig. 2.

Also of interest is the direction of the flow near the surface. If θ is the angle of the limiting streamline with the x direction,

$$\tan\theta = \lim_{z \to 0} \frac{v}{u} = \lim_{\tau \to 0} \frac{xRG}{yRF'/2}$$

This limit has been evaluated numerically.

$$\tan\theta = (2x/y)\ (1.323/1.328) \qquad (41)$$

The writer suggests that it is more than a numerical coincidence that

$$\lim_{\tau \to 0} (G/F') = 1.00\ldots$$

however, he has not yet been able to demonstrate that this fact has any significance.

(III) Flow over a Blade with Thickness

The boundary-layer flow over a certain class of cylindrical blades of chord c whose two-dimensional potential flow velocity is of the form

$$u_1 = \beta yR\left(\frac{x}{c} - \frac{x^3}{c^3}\right), \qquad 0 \leq x \leq c$$

is next considered. Here, β is a parameter related to the thickness of the blade. This external velocity distribution produces a "separation" type of profile of the chordwise velocity component in the boundary layer—that is, a profile having negative values of u_z at the blade surface downstream of the separation line.[10]

The boundary-layer equations for this case are

$$uu_x + wu_z = \frac{\beta^2 y^2 R^2}{c}\left(\frac{x}{c} - \frac{x^3}{c^3}\right)\left(1 - 3\frac{x^2}{c^2}\right) + \nu u_{zz} \qquad (42)$$

$$uv_x + wv_z + 2uR = \beta^2 yR^2\left(\frac{x}{c} - \frac{x^3}{c^3}\right)^2 + \nu v_{zz} \qquad (43)$$

$$u_x + w_z = 0 \qquad (44)$$

The boundary conditions are computed by the method given in reference 4.

$$u_1 = yR\,\varphi_{1x} = \beta yR\left(\frac{x}{c} - \frac{x^3}{c^3}\right) \qquad (45)$$

$$v_1 = R(\varphi_1 - 2x) = R\left(\frac{\beta x^2}{2c} - \frac{\beta x^4}{4c^3} - 2x\right) \qquad (46)$$

The boundary conditions are

$$\left.\begin{aligned} &u = v = w = 0, && z = 0 \\ &u \to \beta yR\left(\frac{x}{c} - \frac{x^3}{c^3}\right) \\ &v \to cR\left(\frac{\beta x^2}{2c^2} - \frac{\beta x^4}{4c^4} - \frac{2x}{c}\right) && z \to \infty \\ &w \to 0 \end{aligned}\right\} \qquad (47)$$

The two-dimensional problem represented by Eqs. (42) and (44) and the boundary conditions (47) on u and w was originally solved by Blasius,[9] who introduced the stream function Ψ to satisfy Eq. (44) and obtained a power series solution of Eq. (42). Following Goldstein,[3] let

$$\left.\begin{aligned} u_1 &= \beta_1 x + \beta_3 x^3 + \beta_5 x^5 + \ldots \\ \Psi &= F_1 x + F_3 x^3 + F_5 x^5 + \ldots \end{aligned}\right\} \qquad (48)$$

where, in this case,

$$\beta_1 = \frac{\beta yR}{c}, \quad \beta_3 = \frac{\beta yR}{c^3}, \quad \beta_5 = \beta_7 = \ldots = 0$$

and the F's are functions of z.

One substitutes $u = \Psi_z$, $w = -\Psi_x$ in Eq. (42) and equates coefficients of powers of x. The resulting set of ordinary differential equations for the F's has been solved, and the results are tabulated in reference 3.

The solution of Eq. (43) for v is conveniently carried out in nondimensional form.

Let

$$\left.\begin{aligned} \xi &= \frac{x}{c}, \quad \eta = \frac{y}{c}, \quad \zeta = Re^{1/2}\frac{z}{c} \\ f &= \frac{u}{\beta y R}, \quad g = \frac{v}{\beta c R}, \quad h = Re^{1/2}\frac{w}{\beta y R} \end{aligned}\right\} \tag{49}$$

where $Re = \beta y R c/\nu$. Eq. (43) becomes

$$fg_\xi + hg_\zeta + \frac{2f}{\beta} = (\xi - \xi^3)^2 + g_{\zeta\zeta} \tag{50}$$

and

$$\left.\begin{aligned} f &= f_1'\xi - 4f_3'\xi^3 + 6h_5'\xi^5 - + \ldots \\ h &= -f_1 + 12f_3\xi^2 - 30h_5\xi^4 + - \ldots \end{aligned}\right\} \tag{51}$$

The functions f_1, f_1', f_3, f_3' . . . are tabulated as functions of ζ in reference 3. A power series expansion for $g(\xi, \zeta)$ is assumed:

$$g(\xi, \zeta) = \sum_{n=0}^{\infty} \xi^n G_n(\zeta) \tag{52}$$

Substitution of expressions (51) and (52) for f, h, and g in Eq. (50) yields an equation in powers of ξ. Equating coefficients of powers of ξ,

$$\begin{aligned} G_n'' + f_1 G_n' - nf_1' G_n - 12f_3 G_{n-2}' + \\ 4(n-2)f_3' G_{n-2} + 30h_5 G_{n-4}' - \\ 6(n-4)h_5' G_{n-4} + \ldots = Q_n \end{aligned} \tag{53}$$

where

$$\begin{aligned} Q_0 &= 0 & Q_4 &= 2 \\ Q_1 &= 2f_1'/\beta & Q_5 &= 12h_5'/\beta \\ Q_2 &= -1 & Q_6 &= -1 \\ Q_3 &= -8f_3'/\beta & &\vdots \end{aligned}$$

The boundary conditions are

$$\left.\begin{aligned} G_n &= 0 \quad \text{all } n, & \zeta &= 0 \\ G_0 &\to 0 \quad G_3 \to 0 & \zeta &\to \infty \\ G_1 &\to -2/\beta \quad G_4 \to -1/4 & & \\ G_2 &\to 1/2 \quad \vdots & & \end{aligned}\right\} \tag{54}$$

The tabular values of f_1', f_3', h_5', . . . show that these quantities are nearly constant and the quantities f_1, f_3, h_5, . . . are linear functions of ζ for $\zeta \geq 4$. If these approximate expressions are inserted in Eqs. (53), it is possible to obtain analytical solutions for the quantities G_n, which are valid $\zeta \geq 4$. The results are

$$\left.\begin{aligned} G_0 &= 0 & G_4 &= -1/4 \\ G_1 &= -2/\beta & G_5 &= 0 \\ G_2 &= 1/2 & G_6 &= 0 \\ G_3 &= 0 & &\vdots \end{aligned}\right\} \tag{55}$$

Eqs. (53) can now be integrated numerically over the finite range $0 \leq \zeta \leq 4$. The integration has been carried out for G_0 through G_6.

The profile of the spanwise flow was calculated for $\beta = 3$, which gives a maximum value of u_1/yR of 1.155.

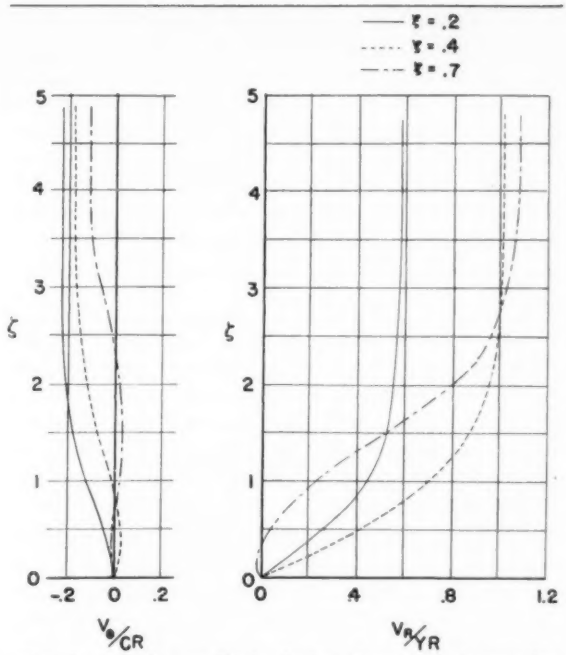

FIG. 3. Velocity profiles in the boundary layer of a rotating symmetrical cylinder for which $u_1 = 3yR(\xi - \xi^3)$. Here, ξ denotes x/c, c is a reference chord, and other notations are the same as in Fig. 2. NOTE: For V_θ/CR and V_R/YR in this figure, read v_r/cR and v_θ/yR, respectively.

The corresponding value for an NACA 0010 airfoil is about 1.158. The potential speed, according to the formula used here,

$$u_1 = \beta y R(\xi - \xi^3)$$

exhibits a stagnation point at $\xi = 0$, rises to the maximum value, and decelerates. Thus, it is typical of the flow around the forepart of an airfoil at small or zero incidence. Curves of radial and tangential velocity profiles are presented in Fig. 3.

It is seen that there is no appreciable radial flow near the separation line for this case. For larger values of β, there would be a larger pressure gradient along the line of chordwise flow separation, and greater spanwise flow in the boundary layer might occur. One must remember, however, that the present theory is limited to slender shapes.

(IV) PROCEDURE FOR ARBITRARY CYLINDERS

The method of solution used here—namely, expansion in powers of x—has been particularly convenient because the two-dimensional solution was available in that form. This will not be the case in general, and a more convenient procedure will be needed for calculation of both u and v for arbitrary $u_1(x)$.

One of the practical methods of approximate solutions of the boundary-layer equations is that of von Kármán and Pohlhausen.[10] A simpleex tension of this method can be used in the present case. If an

analysis similar to that of reference 11 is made, a first-order ordinary differential equation is obtained for the ratio of the spanwise and chordwise boundary-layer thicknesses. While this method is simple in theory, it becomes laborious in practice, because of the large number of terms in the differential equation which must be solved. An approximate check of the validity of the method for the case of the blade with thickness treated above has been made. It is concluded that the method should yield a good approximation in this typical case.

(V) Conclusions

The striking feature of the results of the two cases investigated is that the effects of rotation as calculated are small. This is in disagreement with the engineer's common expression that three-dimensional effects on rotating blades are large. Possible explanations of this disagreement are:

(1) The engineer's impression may be derived from observation of what happens after separation of the flow from the surface. The theory presented here is not valid beyond the separation line and so cannot predict such effects.

(2) The profiles treated have weak pressure gradients. Comparison of the results of references 7 and 11 shows that, for these two cases of yawed wings, the profile with strong pressure gradient had much stronger spanwise flow than the profile with weak pressure gradient. It is reasonable to assume that some such effect would be obtained with rotating blades.

(3) It is possible that the effect of finite span—that is, of a tip or wall—is to accentuate the effects of blade rotation locally.

(4) Only the laminar boundary layer is considered here. It is possible that the effects of rotation on the turbulent boundary layer are more profound.

References

[1] von Kármán, Theodore, *Über laminare und turbulente Reibung*, Zeitschr. f. angew. Math. u. Mech., Vol. 1, pp. 244–247, 1921.

[2] Lamb, H., *Hydrodynamics*, p. 20, Eq. (8); Cambridge, 1932.

[3] Goldstein, S., *et al.*, *Modern Developments in Fluid Dynamics*, Vol. I; Oxford, 1938.

[4] Sears, W. R., *Potential Flow Around a Rotating Cylindrical Blade* (Readers' Forum), Journal of the Aeronautical Sciences, Vol. 17, No. 3, p. 183, March, 1950.

[5] Prandtl, L., *On Boundary Layers in Three-Dimensional Flow*, R. & T. No. 64 British M.A.P. Volkerode, May 1, 1946.

[6] Jones, R. T., *Effects of Sweepback on Boundary Layer and Separation*, N.A.C.A. T.N. No. 1402, July, 1947.

[7] Sears, W. R., *The Boundary Layer of Yawed Cylinders*, Journal of the Aeronautical Sciences, Vol. 15, No. 1, p. 49, January, 1948.

[8] Fogarty, L. E., and Sears, W. R., *Potential Flow Around a Rotating Advancing Cylindrical Blade* (Readers' Forum), Journal of the Aeronautical Sciences, Vol. 17, No. 9, p. 599, September, 1950.

[9] Blasius, H., *Grenzschichten in Flüssigkeiten mit kleiner Reibung.*, Zs. Math. u. Phys., Bd. 56, p. 1, 1908. (Also available in English as N.A.C.A. T.M. No. 1256.)

[10] Prandtl, L., *The Mechanics of Viscous Fluids*, Division G of *Aerodynamic Theory*, Vol. III, Durand, W. F., Ed., pp. 93–94.

[11] Wild, J. M., *The Boundary Layer of Yawed Infinite Wings*, Journal of the Aeronautical Sciences, Vol. 16, No. 1, pp. 41–45, January, 1949.

First U. S. National Congress of Applied Mechanics

Plans have been formulated to hold the First U.S. National Congress of Applied Mechanics on June 11–16, 1951, at Chicago, Ill. The Illinois Institute of Technology will be host to the Congress.

Members of the Institute, one of the sponsoring societies, are cordially invited to submit papers, which should constitute original research in applied mechanics. (Their length must not exceed 5,000 words or the equivalent in equations, tables, and diagrams.) Abstracts must be submitted to the Chairman of the Editorial Committee before April 14, 1951; complete papers must be submitted prior to June 11, 1951.

Additional information about the Congress may be obtained by writing to N. M. Newmark, Secretary of the Congress, University of Illinois, Urbana, Ill. All members are invited to attend.

A Flexible Nozzle for a Small Supersonic Wind Tunnel*

SATISH DHAWAN† AND ANATOL ROSHKO†
California Institute of Technology

SUMMARY

The design of a small supersonic wind-tunnel test section (4 by 10 in.) incorporating a flexible nozzle is outlined. The flexible nozzle consists of a high-strength stepped steel plate. Two screw jacks provide an easy means of continuously changing the nozzle's shape according to the aerodynamic requirements. The boundary-layer compensation can also be varied during operation. Pressure surveys, together with schlieren and interferometric analysis of the test section, show the flow to be uniform over the operating range (M = 1.1 to 1.5).

INTRODUCTION

THE DEVELOPMENT OF experimental research in transonic and supersonic flow has increasingly demanded the use of a wind tunnel with continuous control over the flow parameters. Since the air speed in a supersonic wind tunnel is determined completely by the geometry of the nozzle, it is necessary to provide a different nozzle shape for each different required speed. The use of a flexible nozzle permits a continuous change in the flow Mach Number and constitutes a considerable advantage and improvement over the alternative of using a series of fixed geometry nozzles. The idea of using a flexible nozzle is not new, and there are in existence and operation in this country several supersonic wind tunnels incorporating the device. However, as far as can be determined from published descriptions of these wind tunnels, the flexible nozzle with its shape-changing mechanism is rendered complex by the range and accuracy requirements. For instance, in order to change the nozzle shape the wind tunnel has to be shut down and the required changes made in small degrees of adjustment. During the past year or so there has been in use a flexible nozzle of exceptionally simple design in the 4- by 10-in. Transonic Tunnel at the California Institute of Technology.‡ The supersonic range of the tunnel is limited from approximately M = 1.1 to 1.5, and this fact is fully exploited in the interests of simplicity to achieve a design that permits continuous shape changes in the nozzle during operation while retaining accuracy and uniformity of flow. Over the major portion of the operating range, the only operation required to change the flow Mach Number is the turning of a single jackscrew. This paper briefly outlines the interesting features of this tunnel with special attention to the design, construction, and use of the flexible nozzle.

Received March 22, 1950.

* The authors wish to acknowledge the supervision and help of Dr. Hans Wolfgang Liepmann, under whose direction the design was executed. Harry Ashkenas rendered valuable assistance in the mechanical design.

† Guggenheim Aeronautical Laboratory.

‡ The test section described here is a modification on the original test section of the 2- by 20-in. high subsonic tunnel built in 1944 under A.A.F. contract for high-speed flow investigations. A study of boundary-layer and shock-wave phenomena is at present in progress under N.A.C.A. sponsorship; the design presented here was executed in the course of this work. Results of recent research in the tunnel are being published elsewhere by the N.A.C.A.

DESCRIPTION OF TEST SECTION

The working section of the GALCIT 4- by 10- by 48-in. transonic tunnel is sketched in Fig. 1 showing the essential features of the design. The floor block of the test section carries the one-wall flexible nozzle plate, together with the swiveling jackscrew controls. The floor is hinged just downstream of the main jack, and its downstream end can be raised or lowered by means of a screw jack. This allows alterations in boundary-layer compensation during operation. The ceiling block of the tunnel supports the traversing mechanism and contains a narrow slot for operation of the traversing arm. A pressure box, with access panels mounted on the ceiling block, encloses the traversing mechanism and seals it to the test section. Pressure-sealing of the test section is secured by means of rubber tube-in-groove seals between the sidewalls and floor and the ceiling blocks. The sidewalls are made in panels and allow the window to be located anywhere in the 48-in. length of the test section. The main flexible nozzle consists of a continuous spring steel plate $45^1/_4$ in. long of varying thickness, of which 36 in. forms the flexible nozzle and the remainder is the floor of the test section (see Fig. 1). It is anchored in the contraction with the downstream end also direction-fixed, but it is free to move horizontally on rollers when deflected by the jacks. A second flexible nozzle plate begins where the primary nozzle ends. The flexible second throat acts as a speed control during subsonic operation of the tunnel and may be used as an adjustable supersonic diffuser during supersonic runs.

DESIGN CONSIDERATIONS

(1) *Aerodynamic Nozzle Shapes*

The supersonic range of Mach Numbers in the tunnel is from M = 1.1 to 1.5. Fig. 2 shows the theoretical

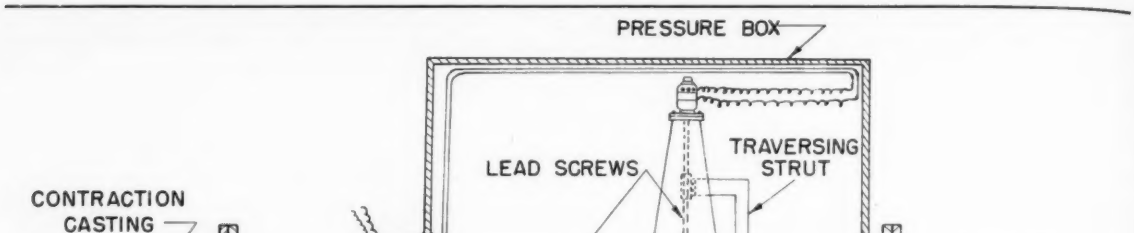

FIG. 1. Sketch of the GALCIT 4- by 10- by 48-in. transonic-tunnel test section.

nozzle shapes covering this range. These shapes were obtained graphically by the well-known method of two-dimensional characteristics.[1] The fundamental procedure in this method consists of assuming an initial expansion curve starting from zero inclination at the throat up to the nozzle expansion angle Θ (Fig. 3), which must be less than, or at most equal to, half the Prandtl-Meyer angle associated with the final Mach Number. The initial expansion curve is then divided into suitable straight segments. The expansion wavelets generated by this convex initial curve determine uniquely the subsequent form of the nozzle for parallel flow at the exit. For a required Mach Number in the test section, there is thus an infinity of possible initial curve and expansion angle Θ combinations. Theoretically, the shortest length nozzle would be obtained by using the maximum value of Θ (equal to half the Prandtl-Meyer angle) and an initial expansion of infinite curvature—i.e., a sharp corner at the throat. Actually, however, the presence of boundary layer limits the rate of expansion. For design purposes, a radius of curvature at the throat of approximately two to four times the test-section height may be used. In choosing the aerodynamic shapes shown in Fig. 2, the initial expansion wave and the nozzle slope Θ were so adjusted as to give constant length nozzles (throat to exit) for the various design Mach Numbers. This permitted the use of a constant length flexible plate for the supersonic nozzle and simplified the mechanical design considerably.

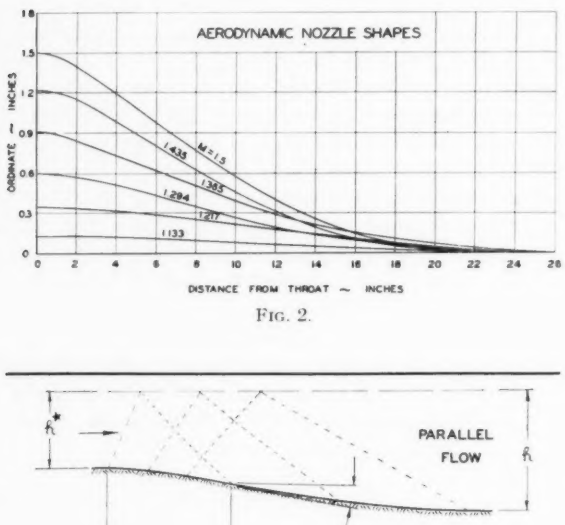

FIG. 2.

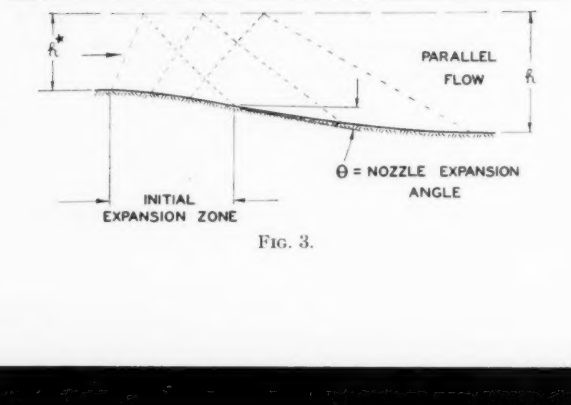

FIG. 3.

(2) *Boundary-Layer Compensation*

The theoretically obtained nozzle shapes do not take into account the growth of the boundary layer on the walls of the tunnel. In order to allow for this, it is usual to displace the physical walls at each point by the "displacement thickness" of the boundary layer at that point. One method of obtaining approximate estimates of the boundary-layer growth is to assume the pressure gradient on the walls as obtained by the in-

viscid flow computation and, then, to use boundary-layer theory to calculate the displacement thickness. In the design under discussion, the compensation for boundary layer was taken into account in a more elementary fashion. Experience in the previous test section of the wind tunnel had shown that a linear correction of 0.021 in. per in. in the walls was sufficient to allow for the boundary-layer growth. In addition, the present design includes provision for alterations in the allowance with the tunnel in operation. Subsequent results justified the estimates used.

The Nozzle Plate

(1) *Requirements*

(a) The nozzle plate should be able to reproduce, during operation, any aerodynamic nozzle shape in the required range.

(b) The shape-changing mechanism should be simple and nozzle settings accurately repeatable.

(c) The plate must be free from local distortion and vibrationally stable during operation of the wind tunnel.

(2) *Plate Shape and Control Configuration*

Study of the aerodynamic shapes (Fig. 2) to be reproduced by the nozzle plate shows that, in general, the aerodynamic shapes have an initial region of relatively high curvature followed by an almost straight portion containing an inflexion point (reversal in sign of the curvature). The terminal section of the shapes is seen to have relatively the largest length and a uniformly decreasing curvature. Fig. 4 shows the curvatures of various configurations of a plate represented as an elastic beam in relation to the curvatures of a representative aerodynamic shape. It is clear that a minimum of two controls is required to produce the required change in sign of curvature in the plate. Fig. 4 also shows how the jacks for changing the shape of the nozzle should be located. Since the greatest curvature in the plate is produced in the vicinity of the main jack, this must be situated close to the throat of the nozzle. It is also evident that it is impossible exactly to reproduce the required curvatures with a continuous plate of constant thickness. Fig. 4d shows the manner in which a variation in moment of inertia of the plate cross section may be used to advantage in bringing the elastic and aerodynamic shape curvatures closer together. The second integrals of these curves—i.e., the actual shapes—would then be still closer. In order to secure smooth entrance and exit conditions at all Mach Numbers, it is highly desirable to have the ends of the nozzle plate fixed in direction. A comparative study of several configurations along the lines indicated above led to the adoption of the configuration schematically represented in Fig. 5. The nozzle plate consists of a stepped beam loaded at two points by screw jacks

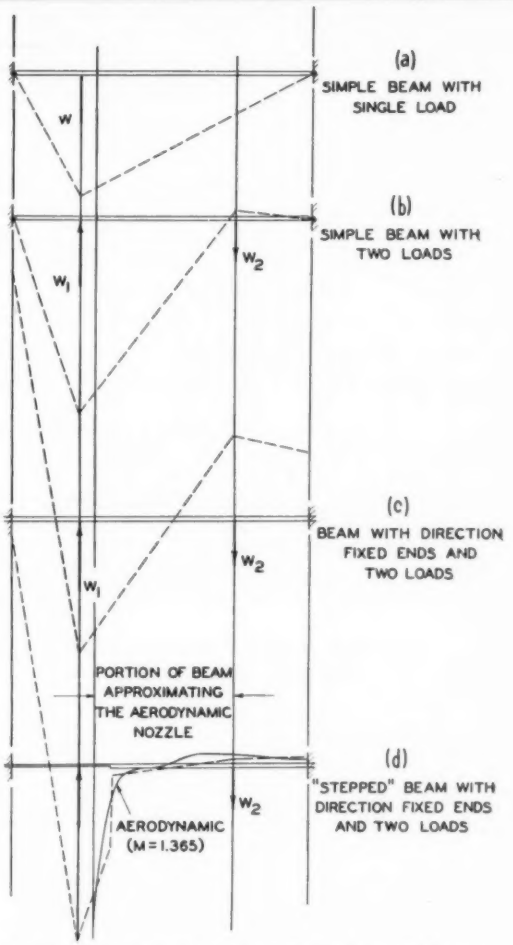

Fig. 4. Curvatures of elastic and aerodynamic shapes.

and having direction-fixed ends. The location of the jacks and the step in the plate was determined by trial to give the best overall reproduction of the aerodynamic shapes over the required range.

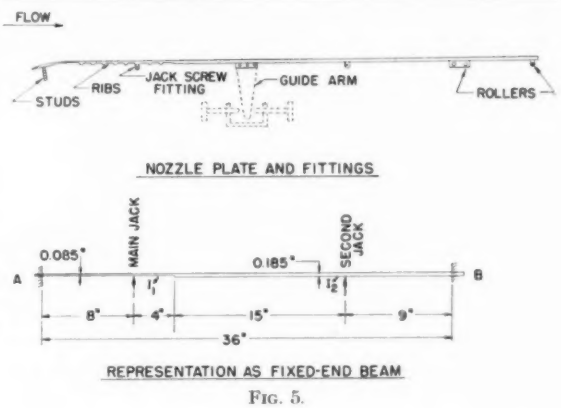

Fig. 5.

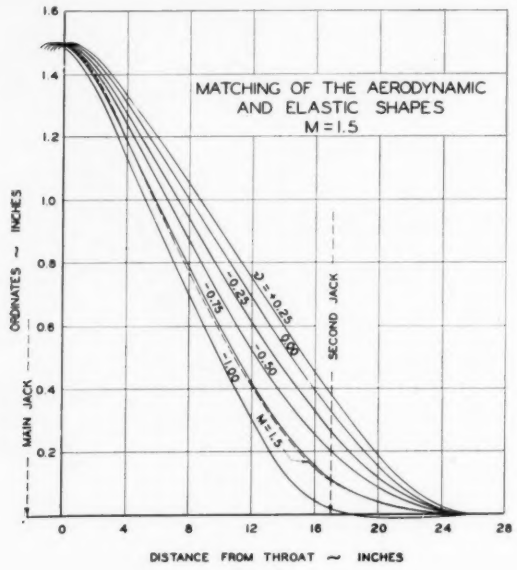

FIG. 6.

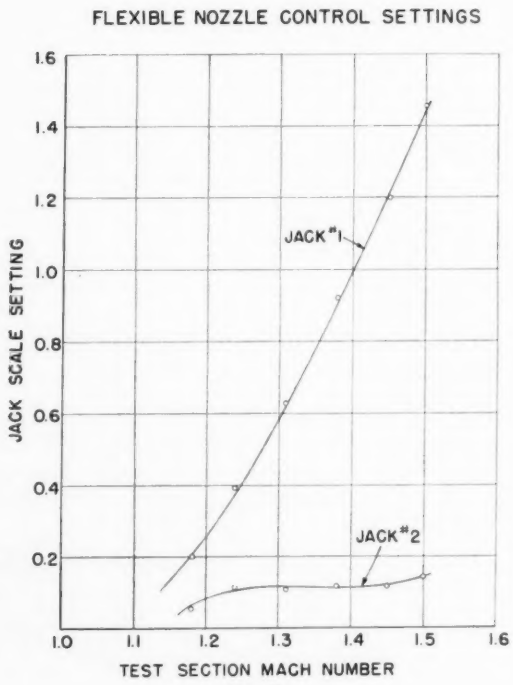

FIG. 7.

(3) *Determination of Control Settings*

The restriction on the deflection curve of the plate when it is required to reproduce an aerodynamic shape is that it must have a prescribed maximum deflection. This is given by the unique height ratio h/h^* associated with a desired supercritical flow in the test section. Here, h is the height of the two-dimensional test section, and h^* is the height at the throat. Knowing the dimensions, end conditions, and type of loading on the plate, the elastic influence curves of the configuration can be calculated. These permit a determination of all the possible plate shapes (Fig. 6) with a given maximum deflection in terms of the load ratio $\nu = W_2/W_1$, where W_1 = load in pounds on the main jackscrew and W_2 = load on the second jackscrew. A superposition of the required aerodynamic shape and the corresponding plate curves serves then to determine the optimum value of ν, and the control settings are computed from the deflection influence functions of the plate. A representative case of matching of the aerodynamic and elastic curves for $M = 1.5$ is shown in Fig. 6, the vertical scale being exaggerated to increase the accuracy of matching. Fig. 7 shows the final curves from which control settings for any Mach Number within the design range may be obtained. It will be observed that over almost the entire range of operation only the main jack setting is required to be altered.

FABRICATION OF THE NOZZLE PLATE

The problem in fabrication was to obtain a relatively thin, high-strength plate free from local deformation, particularly local deformations near the attachment fittings.

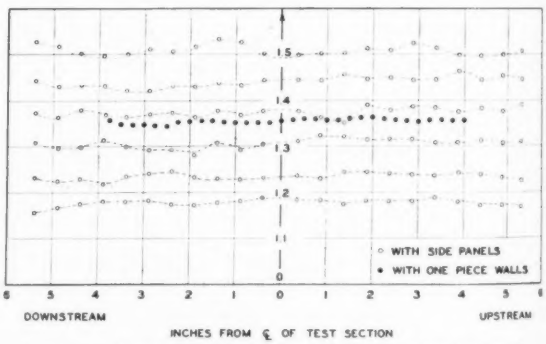

FIG. 8a. Horizontal Mach Number distribution in tunnel.

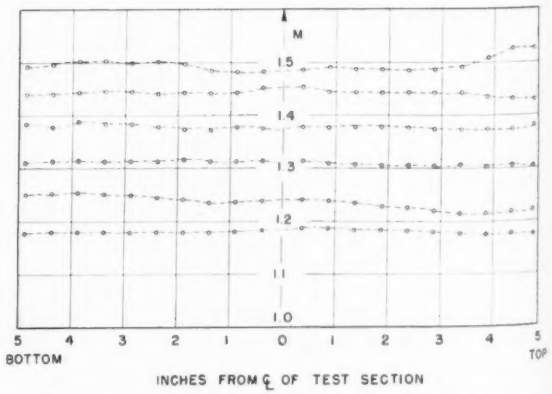

FIG. 8b. Vertical Mach Number distribution in tunnel

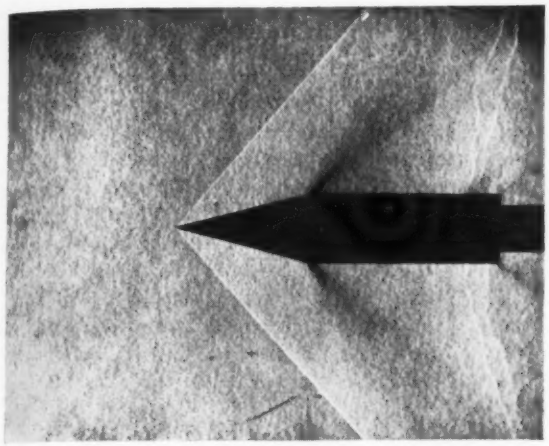

FIG. 9. Schlieren of flow past a cone. Cone half angle = 15°. $M = 1.38$.

(1) *Choice of Material*

From simple beam theory for a beam with fixed ends and given deflection curve and thickness distribution,

$$\text{stress } \sigma \sim Et$$
$$\text{deflection load } W \sim Et^3$$

where

E = modulus of elasticity of the beam material
t = some reference thickness of beam

For the plate to be stable during operation, W and t must be kept as high as possible. A typical comparison between iron and copper alloys shows that, for a given factor of safety,

$$t_{\text{steel}}/t_{\text{bronze}} \doteq 1.5$$

and

$$W_{\text{steel}}/W_{\text{bronze}} \doteq 7$$

These considerations and problems of welding and heat-treatment dictated the choice of steel. SAE 6150, an alloy spring steel, was found to meet the requirements.

(2) *Machining of Plate*

The plate with "step" and stiffening ribs was machined from a $^3/_8$- by 5-in. piece of annealed SAE 6150, the studs and fittings also being machined from the same material. About 0.05 in. of extra material was left on the upper surface of the plate for final surface grinding.

(3) *Attachment of Fittings*

This was done by copper brazing in a hydrogen atmosphere furnace at 2,000°F. (above the heat-treatment temperature). During this operation the plate was clamped in a steel jig.

(4) *Heat-Treatment*

The plate was heat-treated to give a Rockwell hardness of C-38, corresponding to a yield of 154,000 lbs. per sq.in. During the normalizing, quenching, and tempering processes, the plate was clamped in a jig. The results obtained were extremely satisfactory. There are no local distortions in the plate.

(5) *Surface Grinding*

The working surface of the plate was ground to a polish finish, eliminating all surface irregularities.

(6) *Stress Test*

Since the nozzle plate was to carry extremely high stresses in its fully deflected state, a strain-gage test was made to ensure safe operation. The maximum stress produced in the plate when set for $M = 1.5$ was found to be 110,000 lbs. per sq.in. This gives a factor of safety of 1.4.

Evaluation and Calibration

Figs. 8a and 8b show the results of pressure surveys of the test section made at the various design Mach Numbers. The vertical distributions, Fig. 8b, reveal the effect of waves originating at the nozzle and indicate uniform flow with negligible gradients over the entire operating range. Fig. 9 is a schlieren photo-

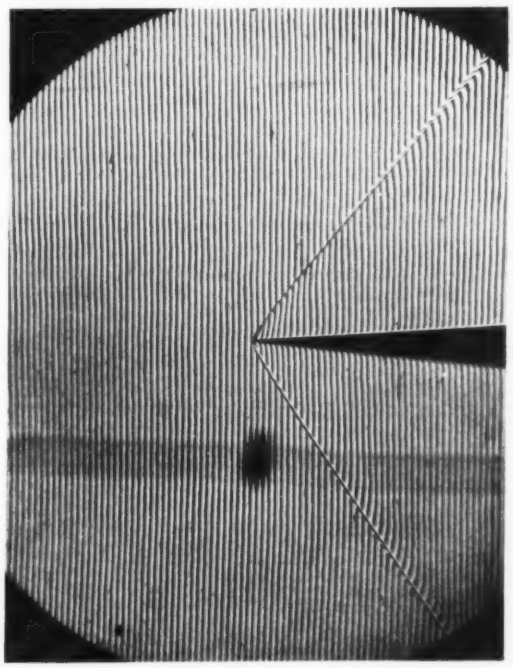

FIG. 10. Interferogram of flow past a wedge. Wedge half-angle = 4.5°. $M = 1.37$.

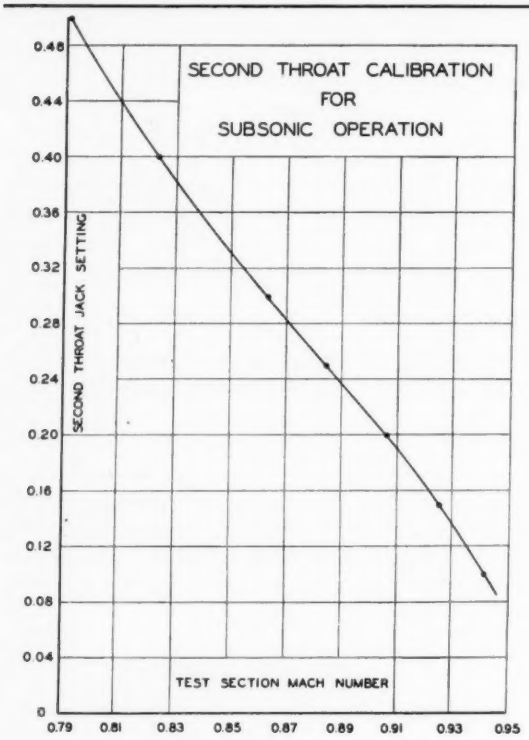

FIG. 11.

graph, and Fig. 10 is an interferogram of the flow in the test section. The straight head wave in Fig. 9 and the straight interference fringes in Fig. 10 confirm the uniform wave free flow indicated by the pressure surveys. The somewhat greater variations in the horizontal surveys (Fig. 8a) are due to the small disturbances introduced at the joints in the sectioned sidewalls. The use of continuous panels for the sidewalls reduces the variations in the horizontal direction to the same order as in the vertical surveys (see Fig. 8a). Figs. 7 and 11, respectively, show the calibration curves for the controls over the supersonic and subsonic range of operation of the tunnel. The change from supersonic to subsonic flow or vice versa can be accomplished without shutting down the tunnel.

CONCLUSION

A flexible relatively high-strength plate free from local distortions has been successfully designed and used for the production of uniform shock-free flow over the range $M = 1.1$ to 1.5. The plate is vibrationally stable during operation, and the repeatability of flows is excellent.

REFERENCE

[1] Puckett, A. E., *Supersonic Nozzle Design*, J. Appl. Mech., December, 1946.

Notice to Contributors

Manuscripts submitted for publication *must* be double- or triple-spaced originals. There should be wide margins on both sides of the sheets and triple spacing around formulas to allow for the marking of directions for the printer.

Original drawings (jet black India ink on white paper or tracing cloth) should accompany the manuscript. *(Blueprints are not acceptable.)* Photographs *must* be on glossy white paper. The smallest lettering on 8- by 10-in. figures should be no less than 1/4 in. high.

Only the simplest formulas should be typewritten; all others should be carefully written in pen and ink. The difference between capital and lower-case letters and Greek symbols should be clearly distinguished.

See Inside Back Cover of this issue for further details.

Sphere Drag Data at Supersonic Speeds and Low Reynolds Numbers*

E. D. KANE†

University of California at Berkeley

SUMMARY

Drag forces on spheres have been measured in a low-density supersonic wind tunnel. Mach Numbers were from 2.1 to 2.8, and the Reynolds Number (based on free-stream properties and sphere diameter) ranged from 15 to 800. Available experimental data for the same Mach Numbers as the present tests, but with Reynolds Numbers in the order of magnitude 10^5, showed that the drag coefficients could be correlated as a function of Mach Number alone and were not altered by a sixfold change in Reynolds Number. The present data showed an increase of drag coefficient by a factor of $2^1/_2$ over the test range. Flow visualization photographs indicated a possibility that interaction occurred between the sphere boundary layer and shock wave at low Reynolds Numbers.

Additional experimental data are required before the relative importance of viscous, molecular flow, and shock-wave effects can be evaluated completely.

SYMBOLS

R	=	Reynolds Number = $Vd\rho/\mu$ (dimensionless)
R_G	=	gas constant, defined by $R_G = p/\rho T$
V	=	velocity (consistent units)
d	=	sphere diameter (in.)
ρ	=	gas density (consistent units)
μ	=	gas viscosity (lbs. per sec. ft.)
$\bar{c}$	=	average gas molecule speed (consistent units)
p	=	gas pressure (microns Hg)
γ	=	ratio of specific heats = 1.40 for air (dimensionless)
a	=	local sound speed in the gas (consistent units)
M	=	Mach Number = V/a (dimensionless)
l	=	molecular mean free path [defined by Eq. (1)] (in.)
A	=	an area, defined by Eq. (4), = $\pi d^2/4$ for a sphere (sq.in.)
K_D	=	drag coefficient for a sphere [defined by Eq. (5)] (dimensionless)
D	=	drag force on sphere (Gm.)
T	=	gas temperature (°F. abs.)
δ	=	boundary-layer displacement thickness (in.)
α, β	=	constants (dimensionless)

Subscripts

c	=	compressible, nonviscous fluid [Eq. (12)]
i	=	impact (pressure)
s	=	static (pressure)
1	=	conditions behind normal shock wave
2	=	quantity measured at surface of cone (Probe No. 15)

INTRODUCTION

MEASUREMENTS OF DRAG FORCES on spheres by many workers have served to clarify certain aspects of the general problem of resistance of bodies to uniform motion in a fluid. Most of the available information for sphere drag forces at subsonic speeds has been summarized in reference 1. The data are correlated as a function of Reynolds Number over the range from approximately 0.04 to 10^5. The lowest Reynolds Numbers were obtained for spheres immersed in liquids. Also available are the data of reference 2 for low Reynolds Numbers in air, under conditions that resulted in molecular flow effects. For supersonic speeds, the only published data appear to be those of Charters and Thomas[3] obtained by firing spheres through still air. The Mach Number range was approximately from 0.3 to 4.0. The Reynolds Number variation, for Mach Numbers greater than 1, was from 2×10^5 to 1.3×10^6. The supersonic data were correlated by the Mach Number within the accuracy of experimental measurements, and there was no Reynolds Number effect.

The theory for the drag force on a sphere in uniform motion is incomplete. For incompressible fluids and low speeds, the analysis of Stokes,[4] obtained by neglecting inertia terms in the flow equations, is applicable. Comparison with experiment indicates that the analysis is valid for $R < 0.5$ and gives values too low at higher R. Oseen[5] obtained a second approximation by considering the effect of some of the inertia terms, and Goldstein[6] computed a result from Oseen's equations which everywhere lies above the experimental data. This latter solution is within 5 per cent of experiment at $R = 1.0$ and deviates by more than 20 per cent at $R = 10$. Stokes's equation can also be applied for spheres moving in a gas at sufficiently low speeds to give $R < 0.5$, provided the molecular mean free path of the gas is small compared to the sphere diameter. In Millikan's[2] experiments, for example, the data did not depart from Stokes's equation until the ratio of gas molecular mean free path to characteristic body dimension—in this case, the sphere diameter—exceeded approximately 0.001.

It is convenient to discuss the various results in terms of the dimensionless combinations of variables used in fluid mechanics. von Kármán[7] pointed out that the Reynolds Number could be written

$$R = (V/\bar{c})\ (d/l)\ (\text{constant})$$

The first ratio is proportional to the Mach Number $M = V/a$, since

Presented at the 1950 Heat Transfer and Fluid Mechanics Institute, Los Angeles, June 28–30, 1950.

* This investigation was aided by funds supplied under a contract from the Office of Naval Research.

† Associate Professor of Engineering Design.

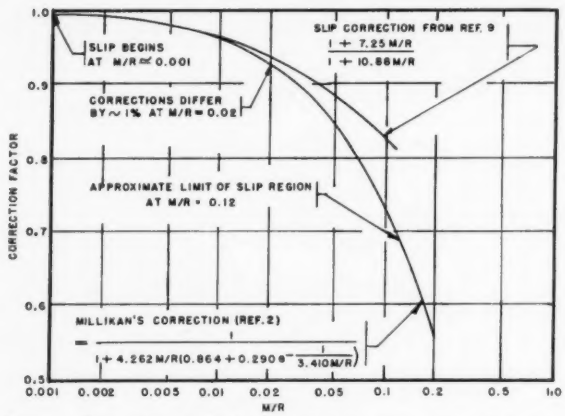

FIG. 1. Corrections to Stokes equation for sphere drag, $R << 1$.

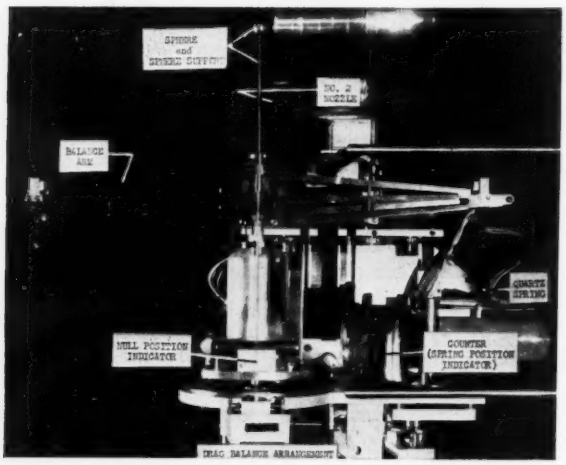

FIG. 2. Drag balance arrangement.

$$\bar{c} = \sqrt{(8/\pi)\ (p/\rho)} = \sqrt{8/\pi\gamma}\ a$$

A result available from kinetic theory[8] is

$$\mu = 0.499\ \rho\bar{c}l \qquad (1)$$

It follows that (for air with $\gamma = 1.40$)

$$l/d = 1.49\ (M/R) \qquad (2)$$

Eq. (2) relates the parameter l/d to the M and R commonly used in fluid mechanics.

Stokes's law was extended by Basset,[9] who used a modified boundary condition to account for "slip" and thus obtained a correction term involving M/R. The resulting expression is plotted in Fig. 1. For comparison, an empirical equation that fits Millikan's experimental data is included [the constants have been adjusted to conform with the value of l given in Eq. (1)]. It appears from Fig. 1 that Stokes's equation modified for "slip" begins to deviate from the data at $M/R \simeq 0.02$, while Millikan's formula indicates that a slip correction of the form

$$1/(1 + \text{Const. } M/R)$$

fits the data for values of M/R up to about 0.12.

For spheres moving in a gas under large mean free path conditions—i.e., $l >> d$—theoretical expressions for the drag have been deduced by using the concepts of kinetic theory. Tsien[10] has reviewed the work available up to 1945, and some later papers[11–13] have extended the calculations.

Tsien[10] discussed the general problem of the effects to be expected at low gas densities and suggested criteria for estimating the boundaries of continuum, large mean free path, and transition flows. The present investigation was concerned with measurement of sphere drag forces at supersonic speeds, over a Reynolds Number range that was expected to produce flows in the continuum and transition regions.

Description of Experimental Equipment and Procedure

No. 3 Wind Tunnel

The required low density supersonic gas stream was provided by the No. 3 Wind Tunnel at Berkeley.[14] A single nozzle, designated the No. 2 nozzle, was employed in these experiments and gave a Mach Number range of approximately 2.1 to 2.8 and a static pressure range from 30 to 128 microns Hg. The free-stream temperature (220° to 300°F. abs.) corresponded to assumed adiabatic expansion from an approximate stagnation condition at room temperature (70°–80°F.) to the indi-

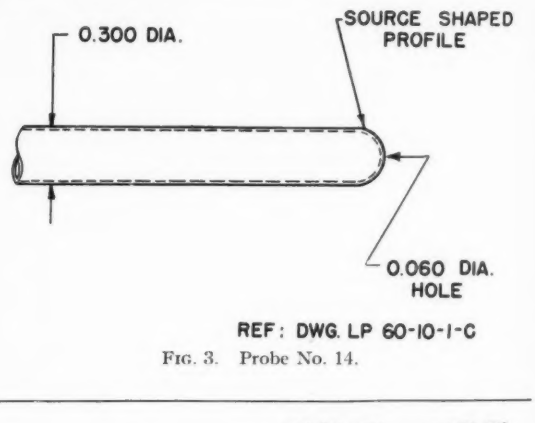

FIG. 3. Probe No. 14.

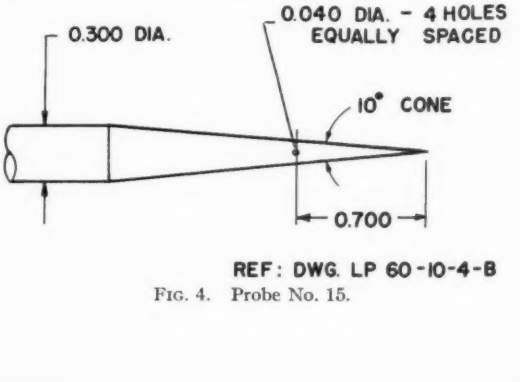

FIG. 4. Probe No. 15.

cated Mach Number at the test section. The dimensions of the No. 2 nozzle are tabulated in reference 15; a photograph of the nozzle installed in the wind tunnel is shown in Fig. 2.

The properties of the gas flow at the test section (where the drag forces were measured) were determined by traversing with two probes, Nos. 14 and 15, in the test region and measuring the pressure associated with each probe (Figs. 3 and 4). The probes were connected by tubing to a Pirani gage and an oil manometer. The Pirani gage was a commercial type with platinum-nickel-alloy filaments and was inserted in an aluminum block that had been wound with resistance wire and covered with insulation. A copper constantan thermocouple was inserted alongside the Pirani tube in the aluminum block and connected to a potentiometer. By controlling the power to the resistance winding, the Pirani-tube wall temperature could be kept constant, as indicated by the thermocouple, within $\pm 2°F$. The power supply for the Pirani gage and the details of an arrangement for recording the Pirani-gage output on a Leeds and Northrup recorder are described in reference 16. The oil manometer is a standard unit employed for low-pressure measurements at Berkeley. One leg of a U-tube manometer filled with butyl phthalate was evacuated by a diffusion pump backed by a mechanical pump. The pressure to be measured was connected to the other leg of the U-tube, and the difference in elevation between the menisci in the two legs was measured with a micrometer screw arrangement. Both the manometer and Pirani gage were calibrated frequently against a McLeod gage.

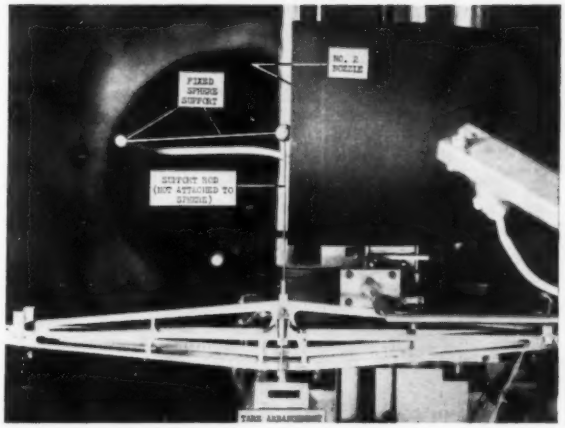

FIG. 5. Tare arrangement.

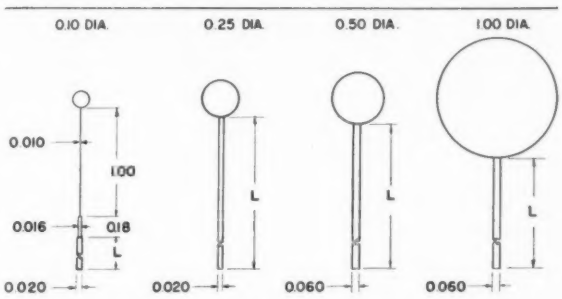

FIG. 6. Sphere and support rod sizes.

Drag Balance

The arrangement used for measuring drag forces is shown in Figs. 2 and 5. The sphere was mounted on a support rod of the size indicated on Fig. 6, the support rod standing vertically in the wind tunnel. The support rod in turn was attached to the beam of an analytical balance. The brass support column of the original balance was changed to a plastic in order to insulate the upper part of the balance, and a motor drive was added so that the mechanism for raising and lowering the beam on its knife edges could be remotely controlled. With the balance located at the test section, with only the support rod and sphere extending into the flow region, the combined drag force on the sphere and support rod resulted in a moment about the main balance knife edge (Fig. 7). This moment was resisted by a quartz spring with one end hooked to one side of the balance beam and the other end hooked to a rod whose vertical position could be changed by turning a micrometer screw. The motion of this rod was also motorized for remote control, and the angular movement of the micrometer screw was geared to a counter that could be read at a distance. The gearing was

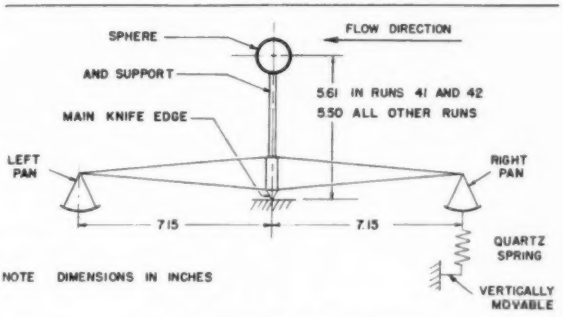

FIG. 7. Schematic of drag balance.

arranged so that the counter indicated the vertical position of the bar directly in thousandths of an inch. In operation, the quartz spring could thus be extended a known amount until the moment due to drag on the sphere and support was balanced by the moment introduced by the spring force, and the balance beam thus returned to a null position. The null position was indicated by the original balance pointer and scale, viewed at a distance through a small telescope. In operation, the balance arm was frequently raised and

TABLE 1
Summary of Experimental Results

Run	Sphere Diameter (In.)	Flow Rator (Scale Reading)	Axial Position (In.) (+)	p_s (Microns Hg)	M	Pan Force (Milligrams) Total	Tare	Net	K_D	R
42	1.0 S	80	0.10	93	2.40	2,812	...	2,488	0.480	464
41	1.0 T	79	0.10	98	2.31	...	324	...	0.494	448
42	1.0 S	139.5	0.10	128	2.56	4,280	...	3,759	0.474	753
41	1.0 T	140	0.10	126	2.53	...	521	...	0.482	768
44-5	0.25 S	80	0.10	106	2.30	337	...	180	0.545	120
47	0.25 T	80	0.10	86	2.55	...	157	...	0.547	126
47	0.25 T	80	0.10	100	2.33	...	157	...	0.564	116
44-5	0.25 S	80	0.40	106	2.30	340	...	182	0.550	120
47	0.25 T	80	0.40	86	2.55	...	158	...	0.551	126
45	0.25 S	30	0.10	42	2.57	179	...	107	0.645	63
47	0.25 T	30	0.10	56	2.24	...	72	...	0.648	59
47	0.25 T	30	0.10	63	2.10	...	72	...	0.650	57
45	0.25 S	30	0.40	42	2.57	181	...	108	0.663	62
47	0.25 T	30	0.40	56	2.24	...	73	...	0.656	58
46	0.25 S	18	0.10	31	2.45	121	...	76	0.695	41
47	0.25 T	18	0.10	31	2.46	...	45	...	0.689	41
47	0.25 T	18	0.10	44	2.08	...	45	...	0.680	39
46	0.25 S	18	0.40	31	2.45	120	...	75	0.688	41
47	0.25 T	18	0.40	31	2.46	...	45	...	0.682	41
47	0.25 T	18	0.40	45	2.05	...	45	...	0.677	38
49	0.10 S	18	0.10	46	2.12	49.0	...	19.4	0.995	17
51	0.10 T	18	0.10	36	2.23	...	29.6	...	1.111	15
49	0.10 S	18	0.40	33	2.50	48.8	...	18.8	0.967	18
51	0.10 T	18	0.40	38	2.17	...	30.0	...	1.113	14
50	0.10 S	80	0.40	77	2.65	153	...	36	0.698	50
51	0.10 T	80	0.10	94	2.34	...	117	...	0.739	45
50	0.10 S	80	0.40	94	2.40	154	...	36	0.702	47
51	0.10 T	80	0.40	93	2.37	...	118	...	0.726	45
50	0.10 S	30	0.10	51	2.37	74.3	...	23.6	0.873	25
51	0.10 T	30	0.10	56	2.20	...	50.7	...	0.927	22
50	0.10 S	30	0.40	50	2.42	74.7	...	23.7	0.857	26
51	0.10 T	30	0.40	56	2.20	...	51.0	...	0.926	22
53	0.25 S	140	0.10	107	2.81	496	...	255	0.514	204
54	0.25 T	140	0.10	113	2.71	...	241	...	0.522	194
53	0.25 S	140	0.40	112	2.74	497	...	255	0.513	199
54	0.25 T	139.5	0.40	117	2.67	...	242	...	0.517	194
53	0.25 S	120	0.10	109	2.61	466	...	246	0.561	170
54	0.25 T	120	0.10	113	2.54	...	220	...	0.572	163
53	0.25 S	120	0.40	109	2.61	470	...	256	0.583	169
54	0.25 T	120	0.40	111	2.57	...	214	...	0.591	164
53	0.25 S	100	0.10	99	2.54	403	...	218	0.575	143
54	0.25 T	100	0.10	97	2.56	...	185	...	0.581	143
53	0.25 S	100	0.40	101	2.51	414	...	229	0.608	141
54	0.25 T	100	0.40	102	2.50	...	185	...	0.607	142
55	0.50 S	70	0.10	77	2.53	917	...	590	0.509	221
56	0.50 T	68	0.10	85	2.39	...	327	...	0.516	210
55	0.50 S	70	0.40	78	2.52	921	...	595	0.511	221
56	0.50 T	68	0.40	...	...	...	326	...	...	...
55	0.50 S	80	0.10	88	2.49	1,011	...	640	0.499	243
56	0.50 T	80	0.10	92	2.43	...	371	...	0.499	242
55	0.50 S	80	0.40	94	2.42	1,025	...	652	0.500	238
56	0.50 T	80	0.40	...	...	...	373	...	...	...
55	0.50 S	120	0.10	112	2.60	1,380	...	858	0.482	342
56	0.50 T	120	0.10	104	2.69	...	522	...	0.483	354
55	0.50 S	120	0.40	111	2.61	1,383	...	858	0.482	344
56	0.50 T	120	0.40	...	...	...	525	...	...	...
55	0.50 S	21.5 (L.F.)	0.10	133	2.72	1,764	...	1,082	0.465	461
56	0.50 T	21.5 (L.F.)	0.10	131	2.74	...	682	...	0.465	465
55	0.50 S	21.5 (L.F.)	0.40	131	2.74	1,761	...	1,074	0.462	466
56	0.50 T	21.5 (L.F.)	0.40	...	...	...	687	...	...	...
55	0.50 S	140	0.10	113*	2.71*	1,554	...	962	0.494	387
56	0.50 T	140	0.10	...	...	...	592	...	...	...
55	0.50 S	140	0.40	117*	2.67*	1,559	...	963	0.488	387
56	0.50 T	140	0.40	...	...	...	596	...	...	...

* Estimated from Run 54.

lowered from the knife edge during a reading so that possible movement of the arm on the agate surface could be corrected.

In order to obtain a tare correction for the drag force on the support rod, every run was repeated with the arrangement shown in Fig. 5. The sphere was supported by a rod extending downstream along the nozzle axis and connected to a stationary support arm. A dummy support rod, of the same exposed length and diameter as the original sphere support rod, was attached to the drag balance and placed in the same position as the original support rod. The clearance between the top of the dummy support rod and the bottom of the sphere surface varied from approximately 0.010 to

0.030 in. in the worst case, as compared to an exposed length of the support rod in the nozzle ranging from 2.26 to 2.71 in. The tunnel was then operated with the same flow conditions used for the original sphere plus support arm drag measurements, and the dummy support arm drag was measured with the balance under these conditions. Simple subtraction then gave the net drag force on the sphere alone, which was subsequently used in reducing the data. Reference to Table 1 shows that the tare correction—i.e., the drag on the support rod alone—varied from 13 to 330 per cent of the sphere drag force (Runs 42, 41 and 50, 51, respectively).

Balance Calibration Procedure

The balance was calibrated by adding weights to the left pan of the balance arm (see Fig. 7) and then extending the quartz spring to bring the unit back to a null position. The counter reading indicating the spring extension and the corresponding calibration weight were then recorded. Three different spring sizes were used to maintain the desired accuracy over the whole range of drag forces. The calibration procedure was checked generally before and after each run and, in every case, was also checked for ascending and descending values of the calibration weights in order to detect any hysteresis or creep effects.

Reduction of Experimental Data

The experimental results for each run are tabulated in Table 1. Pressure readings with the two probes were obtained at a number of points in the region to be occupied by each sphere in order to detect any variations in stream conditions over the volume occupied by the sphere and to allow determination of suitable average values of the flow properties for purposes of data reduction. For Probe No. 15, it was assumed that the analysis summarized in reference 17, which was derived on the basis of a compressible nonviscous gas, was applicable. This reference gives, in tabulated form, the relationship between the cone half-angle (5° in the case of Probe No. 15), the undisturbed stream static pressure p_s, the undisturbed Mach Number M, and the measured pressure at the surface of the cone, p_2. By a similar compressible nonviscous flow analysis, the pressure obtained with Probe No. 14, p_i, is related to the stream static pressure p_s and the Mach Number M by the Rayleigh formula.[18] With these assumptions, the two unknowns M and p_s could be obtained from the measured values of p_2 and p_i.

Additional quantities recorded included the room temperature, the stagnation temperature and pressure in the settling chamber of the wind tunnel, and the arbitrary scale indication of a flow-rate meter. In the case of the drag balance readings, the centerline of the sphere and support rod always coincided with the centerline of the nozzle exit plane and was located various distances downstream (along the nozzle axis) from this plane. The values of M and p_s recorded in Table 1 correspond to the indicated axial positions.

In order to put drag data on a nondimensional basis, it is customary to write the drag force as

$$\text{drag} = C_D \cdot (1/2)\ (\rho V^2 A) \tag{4}$$

where C_D is a dimensionless coefficient and the other quantities are in consistent units. In the case of a spherical shape, this type of equation can be further reduced to

$$D = K_D \cdot \rho\ V^2 d^2 \tag{5}$$

where K_D is then defined by

$$K_D = (\pi/8)\ C_D \tag{6}$$

The quantity K_D will be referred to as the drag coefficient, and the experimental data were reduced to give the values of this drag coefficient in the present case. For convenience in the matter of units, the above equations can be transformed, by using the perfect gas law and the definitions of the quantities involved, into

$$D = 1.23 \times 10^{-2}\ K_D \cdot p_s M^2 d^2 \tag{7}$$

where the units are given in the nomenclature list. Calculation of the quantity K_D from the experimental data is summarized in Table 1.

As a final step, the Reynolds Number corresponding to the conditions of the experiments was computed. The magnitude of the viscosity coefficient μ was determined from Sutherland's equation[19]

$$\mu = \mu_0 \left(\frac{T_0 + C}{T + C}\right) \left(\frac{T}{T_0}\right)^{3/2} \tag{8}$$

where $\mu_0 = 10.0 \times 10^{-6}$ lb. per sec. ft. at 450°F. abs.[20] and $C = 202$°F. abs.[19]

It was assumed that the flow in the wind-tunnel nozzle from the settling chamber to the test section, where the drag forces were measured, was adiabatic. If it is further assumed that the perfect gas law is applicable, then the free-stream temperature can be determined in terms of the measured settling chamber or stagnation temperature T_0 by the relation[21]

$$T/T_0 = 1 + [(\gamma - 1)/2]\ M^2 \tag{9}$$

The numerator of the Reynolds Number $Vd\rho$ can be expressed in terms of M and p_s by the following manipulation, using the perfect gas law and the definition of M:

$$\rho = p_s/R_G T$$
$$M^2 = (V/a)^2 = V^2/\gamma R_G T$$
$$R = \sqrt{\gamma/R_G T}\ (M p_s d/\mu) \tag{10}$$

Finally, the Reynolds Number (for air) can be expressed in a convenient system of units as

$$R = 2.14 \times 10^{-4}\ (M p_s d/\mu\sqrt{T}) \tag{11}$$

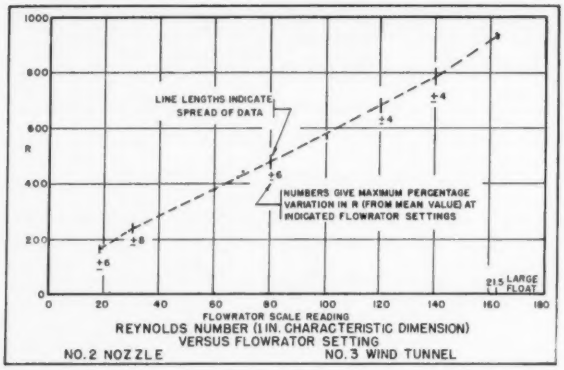

FIG. 8.

The free-stream Reynolds Numbers calculated by this equation for each experimental run are tabulated in Table 1.

SOURCES OF EXPERIMENTAL ERROR

Drag Balance

Forces in still air were measurable within ±2 per cent maximum deviation, with the mean deviation less than ±1 per cent. These figures include creep or hysteresis effects, since calibrations were taken both before and after a run. During a run, the drag balance counter was read at least twice for each condition, the unit being balanced once, then moved well out of balance, then balanced again. The readings were consistent within ±1 per cent. For Runs 50 and 51, where the tare correction was approximately 330 per cent of the sphere drag force, the mean deviation in the balance calibration data was less than ±0.5 milligram. This would result in a maximum error of approximately ±3 per cent in the measured sphere drag force for these runs. The error in measuring the drag force was less than this figure in all other runs.

Pressure Readings

The maximum shift in calibration constant for the oil manometer corresponded to ±5 per cent variation about a mean value, and this figure may be taken as representing the accuracy of the impact-tube readings. The pressures associated with the cone probe were, in some cases, as low as 40 microns Hg, and in this range a variation in "zero" settings was the most serious source of error. Since the individual errors are difficult to separate, Run 47 was carried out with pressures indicated by both the manometer and the Pirani gage. This run covered flow rator readings at 18, 30, and 80, where the manometer zero shift errors should be most serious. K_D and R were computed using both sets of pressure readings. In the worst case (Run 47, FR = 80, d = 0.25 in., axial position = +0.10), the manometer and Pirani gave, respectively, R = 126 and 116, K_D = 0.547 and 0.564—or variations of about 8 per cent in R and 3 per cent in K_D.

Tare Procedure

Obtaining a tare correction for the drag of the sphere support required resetting tunnel conditions to correspond to those existing when the sphere plus support rod readings were obtained. This was accomplished by setting the flow rator to the same scale reading and by independently reading the indicated stagnation pressure. The least count of the flow rator scale was 1 unit (in 18, 30, 80, 140—see Fig. 8). The room temperature variation over all the runs was under 10°F., or less than 2 per cent change in temperature on the absolute scale.

The small variations in adjusting the flowmeter, room temperature changes, and possible small distortions of the plastic nozzle would cause changes in the test-section flow conditions. One method of indicating the cumulative effect of these errors, plus the pressure gage calibration errors, was to determine the Reynolds Number (per 1-in. characteristic dimension) variation obtained at each flow rator setting. This could be done readily from the tabulated values of Table 1, and the results are plotted on Fig. 8. This graph shows that the maximum variation in R at a given flow rator setting was from ±4 to ±8 per cent about a mean value. The resulting uncertainty in K_D does not exceed ±5 per cent.

Interpretation of Probe Readings

In addition to experimental errors, there was a systematic error involved in interpreting probe pressure readings to obtain the Mach Number and static pressure of the gas stream. As described previously, the probe readings were analyzed using theory applicable to a compressible, nonviscous gas, with standard boundary conditions for a continuum fluid. This procedure may lead to errors in the present case because of viscous and molecular flow effects.

TABLE 2

(Reynolds Numbers R and R_1 Based on 0.3-in. Diameter Dimension of Probe No. 14)

M	M_1	R	R_1	(p_i/p_s) Eq. (3)	(p_i/p_s) Eq. (13)	Per Cent Difference
2.8	0.50	1,000	475	9.86	9.88	0.2
2.8	0.50	100	48	9.86	10.02	1.6
2.8	0.50	40	19	9.86	10.25	4.0
2.1	0.56	1,000	605	6.17	6.18	0.2
2.1	0.56	100	60	6.17	6.27	1.5
2.1	0.56	40	24	6.17	6.40	3.7

The viscous effects have been analyzed for an impact tube in subsonic flow and take the form,[22] for a spherical shape,

$$p_i = p_c + \frac{\mu V}{d} \frac{[3 - (83/110)M^2]}{1 + (0.457/\sqrt{R})} \qquad (12)$$

p_c is the impact pressure that would exist for a compressible nonviscous fluid. Eq. (12) shows that the measured impact pressure will be higher than the "ideal" value. For supersonic flow, reference 22 suggests use of Eq. (12), with p_c being the stagnation pressure that would occur in a compressible nonviscous fluid after passage through a normal shock wave. The complete equation then becomes (for a spherical shape)

$$p_i = p_s \left\{ \frac{[(\gamma + 1)/2\ M^2]^{\gamma/(\gamma-1)}}{\{[2\gamma/(\gamma+1)]M^2 - [(\gamma-1)/(\gamma+1)]\}^{1/(\gamma-1)}} + \left(\frac{2\gamma}{\gamma+1} M^2 - \frac{\gamma-1}{\gamma+1}\right) \frac{\gamma M_1^2}{R_1} \frac{[3 - (83/110)M_1^2]}{1 + (0.457/\sqrt{R_1})} \right\} \qquad (13)$$

The actual impact tube (Probe No. 14) was source-shaped rather than spherical. However, Eq. (13) would be expected to give approximately correct results for the actual probe. More significant than this possible discrepancy is the fact that Eq. (13) has never been checked experimentally, and the assumptions on which it is based may be in error.

Only the first term of Eq. (13) has been used in reducing the experimental data. To estimate the magnitude and effect of the possible error in this procedure, the correction of Eq. (13) has been computed for the range of values of M and R covered in the tests and is summarized in Table 2.

The following conclusions can be made regarding the probable effect of viscous corrections on interpretation of the impact tube pressure:

(1) The correction is important only for the lowest values of R encountered in this investigation. For $R = 40$, the smallest value encountered in any run (Run 51), the correction on p_i/p_s was less than 4 per cent. The corresponding error in M would be approximately 2 per cent; that in K_D, about 2 per cent; and that in R, about 4 per cent. At $R = 100$, the indicated error is less than 1 per cent and decreases rapidly for higher R.

(2) The correction *always* consists of an additional term. This results in a value of M which is too high if the correction is neglected by utilizing Eq. (3) in reducing the experimental data, as was done here. Carrying through a sample calculation shows that the use of a value of M which is too high gives a value of K_D which is too low. This means that the rapid increase in K_D for decreasing R (see discussion of results) would be accentuated rather than reduced if the correction of Eq. (13) had been utilized in reducing the data.

This discussion has been concerned entirely with viscous effects on an impact tube, and the problem of interpretation of the readings of Probe No. 15 remains. Probe No. 15 is a 5° half-angle cone, for which the nonviscous theory gives ratios of probe pressure, p_2, to static pressure, p_s, ranging from 1.10 to 1.16, for M from 2.1 to 2.8. While viscous effects undoubtedly occur, probably in the form of a boundary layer that changes the pressure distribution from the "ideal" values, they would not be expected to have a large effect; a 50 per cent change in the pressure increment on the cone surface would result in less than 8 per cent change in the static pressure deduced from the experimental probe pressure. No experimental or additional theoretical conclusions are available at the present time for the problem of viscous compressible flow over a cone.

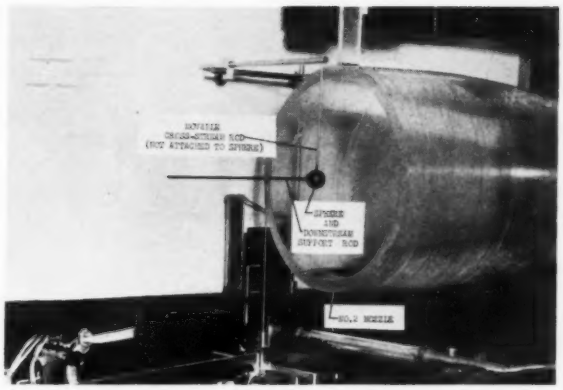

FIG. 9. Test arrangement to determine effect of cross-stream support.

Finally, the effect of slip or other molecular flow phenomenon on either probe has not been evaluated. The largest M_1/R_1 value (based on a 0.3-in. characteristic dimension) was approximately 0.03. From the indications of Millikan's data (see Introduction), it would be expected that the molecular flow effects would be small, even for this condition. For most of the experimental range, the small values of M_1/R_1 would indicate a negligible correction.

Method of Sphere Support

Support of the sphere by a rod of finite size will disturb the flow and cause an error in the drag coefficient which is not completely eliminated by the method of tare correction outlined earlier. Support from the rear, by a rod aligned in the flow direction, is the recommended procedure. The cross-stream support in these tests can cause serious discrepancies in the results when the Reynolds Numbers are in a critical region that is of the order of magnitude of $R = 10^5$.[23] The effect has been traced to a transition from laminar to turbulent boundary layer, which changes the position of the boundary-layer separation point and alters the pressure distribution on the sphere. In the present case, however, the Reynolds Numbers are low enough so that the boundary layer remains laminar,[24] and the marked effect apparent at higher Reynolds Numbers would not be expected.

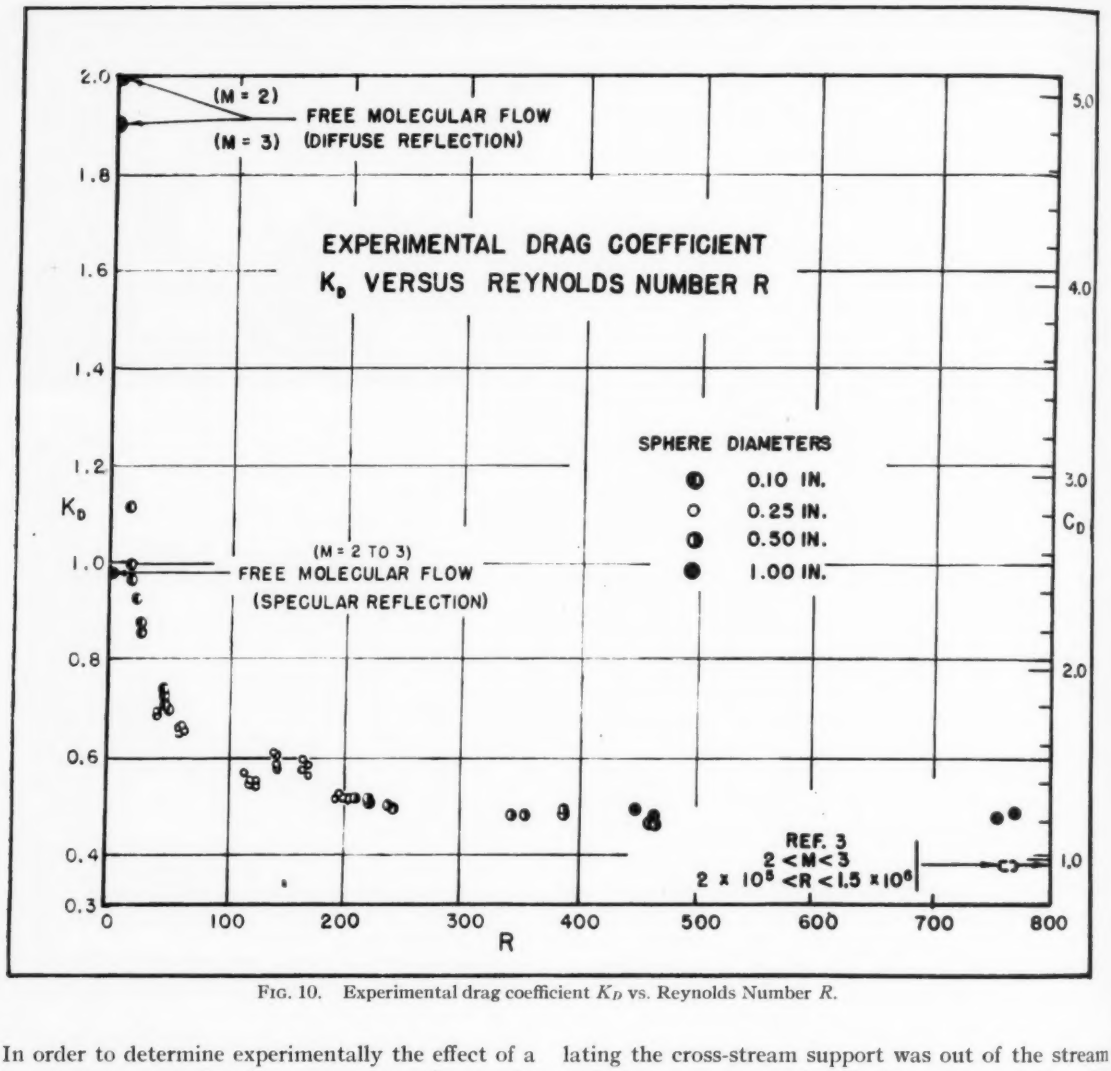

FIG. 10. Experimental drag coefficient K_D vs. Reynolds Number R.

In order to determine experimentally the effect of a cross-stream support for the present operating conditions, the 0.5-in. sphere and support rod were remounted on the drag balance as indicated on Fig. 9. A rod, equal in diameter to the original 0.060-in. support rod, was arranged so that it could be moved either out of the nozzle flow or directly against the top side of the sphere (with approximately 0.010-in. clearance). Drag measurements were obtained when the rod simulating the cross-stream support was out of the stream and then were repeated with the rod moved into the position indicated on Fig. 9. The experimental values of f_1 (the ratio of total drag force without cross-stream rod to total drag force with cross-stream rod in position) are shown in the second column of Table 3. By comparing the total drag force obtained for the same flow conditions during the original runs (Table 1) with the force obtained for the arrangement of Fig. 9, the tare force for the downstream sphere support of Fig. 9 was determined. The ratio of tare force to total force with cross-stream rod in position is entered in the third column of Table 3 (as f_2). The net effect of the cross-stream rod on the sphere drag force then was computed and is entered in the fourth column of Table 3. The quantity f is the ratio of sphere drag force without a cross-stream rod to that with a cross-stream rod in position.

TABLE 3
(Data from Runs 71 and 72)

Flow Rator Scale Reading	f_1	f_2	f
68	1.020	0.424	1.04
	1.011	0.412	1.02
100	1.017	0.42*	1.03
120	1.034	0.417	1.06
140	1.032	0.416	1.06
	1.021	0.414	1.04

* Estimated.

The effect of the cross-stream support was to give values of the sphere drag coefficients *lower* than those determined with a downstream support or sting. As-

suming that the sting support gives more nearly correct values of the drag coefficient, the drag coefficients in Table 1 should be *increased* by approximately 4 per cent. The experimental correction ranged from 2 to 6 per cent, based on the results with a 0.5-in. diameter sphere tabulated in Table 3.

The 0.5-in. diameter sphere and 0.060-in. diameter support rod represented the largest ratio of support rod diameter to sphere diameter used in this investigation (Fig. 6). Evidence that the experience with the 0.5-in. sphere is representative of the behavior to be expected from the other test configurations is gained from Fig. 10, which shows that drag coefficients obtained for spheres of different sizes at the same Reynolds Numbers gave the same measured drag coefficients. This was verified at three different Reynolds Numbers, where the 0.1- and 0.25-in., the 0.25- and 0.50-in., and the 0.50- and 1-in. sphere diameter data overlapped.

Discussion of Experimental Results

The values of the drag coefficient K_D are plotted as a function of the Reynolds Number R on Fig. 10, and the experimental points are seen to define a single curve with a scatter that is the same order of magnitude as the experimental errors. Reference to Table 1 shows that the Mach Number range was small in these tests, M varying from 2.1 to 2.8. This change is not sufficient to permit conclusions regarding the Mach Number effect; the change in K_D at normal pressures over the same Mach Number range was less than 3 per cent.[3] The striking fact is the significant variation in drag coefficient with Reynolds Numbers less than approximately 10^3.

The cumulative effect of the various sources of error discussed in the section on "Sources of Experimental Error" can be estimated from Fig. 10. The standard deviation in K_D for all the data is approximately ± 5 per cent. The largest variation from a faired curve through the experimental points occurred at $R \simeq 140$ and $R \simeq 165$, for Runs 53 and 54 (0.25-in. diameter sphere) at flow rator settings equal to 100 and 200, respectively. These values are approximately 9 per cent higher than the faired curve. The reason for the large scatter at these points is not clear. Data obtained during the same runs, at $R = 200$, check well with the points obtained at the same R with the 0.50-in. diameter sphere, so that some gross error in calibration or in the drag balance adjustment is unlikely.

In analyzing the drag forces obtained with aerodynamic shapes, experience has shown that the total drag force can be separated into two components. The first component is called wave drag and is the net drag force that results from integration of the pressure distribution over a body, the pressures being measured normal to the body surface. The second component is a skin friction drag, which is the integrated effect of the tangential shearing stress components over the surface. The latter component often can be estimated from boundary-layer theory. In general, this estimate requires knowledge of the type of boundary layer—whether laminar or turbulent—and the location of points where the boundary layer may separate from the body.

A common procedure is to obtain experimentally a pressure distribution for a particular aerodynamic shape under given flow conditions, integrate the resulting distribution to obtain the wave drag, and then add skin-friction drag computed from boundary-layer theory. This procedure, apparently, is satisfactory for subsonic speeds with streamlined bodies at high Reynolds Numbers, where the skin-friction component is a small part of the total drag and where separation of the boundary layer is present for only a small percentage of the body surface. In the case of a sphere, the problem is complicated by the fact that separation inevitably occurs (unless the Reynolds Number is so low that the flow is in the Stokes region), and the wave drag is greatly affected by the behavior of the boundary layer. However, this procedure—separating drag into two components—may be utilized to give a rough estimate of the nature of the aerodynamic phenomena underlying the results shown in Fig. 10.

For the low Reynolds Numbers of the present investigation, the boundary layer is assumed to remain laminar up to the point of separation. This assumption implies that the shock wave associated with the sphere at supersonic speeds is sufficiently far upstream so as not to affect the boundary layer. The flow behind the shock wave then may be characterized by a Reynolds Number R_1, which is related to the free-stream R by the known process occurring in a normal shock wave. R_1 was calculated, for known values of M and R, by determining the ratios V_1/V, ρ_1/ρ, and T_1/T from reference 25 and μ_1/μ from Eq. (8). The R_1 derived in this way actually would be expected to give the correct value only on the stagnation line immediately behind the shock wave, since the shock has different curvatures at other points of the flow; but this single value is a plausible one for characterizing the subsonic region behind the shock wave, particularly for the limited Mach Number range covered in these experiments.

With this hypothetical picture of the flow process, an explanation of the trend of the experimental values can be attempted. The drag coefficient is known at high Reynolds Numbers, where the boundary-layer thickness is negligibly small compared to the sphere radius. It will be assumed that the drag coefficient at low R can be determined by using the known coefficient at high R for a sphere that has an effective diameter $(d + 2\delta)$. δ is some value, averaged over the sphere surface, of the boundary-layer displacement thickness. The product of the drag coefficient by d^2 [see Eq. (5)] is then replaced by

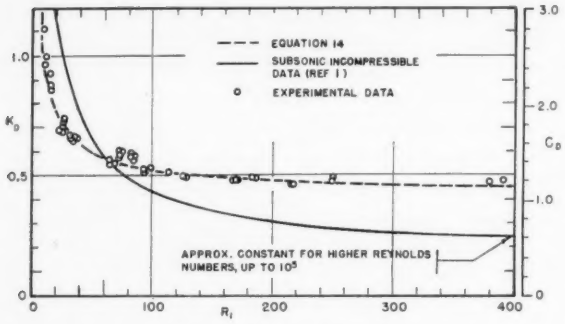

FIG. 11. Drag coefficient as a function of Reynolds Number R_1 computed behind a normal shock wave.

(drag coefficient) $(d + 2\delta)^2$ = (drag coefficient) $\times$ $[1 + (2\delta/d)]^2 d^2$

so that the effective drag coefficient K_D is

$$K_D = K_D' [1 + (2\delta/d)]^2$$

where K_D' is evaluated for $\delta/d \simeq 0$. From reference 3,

$$K_D' \simeq 0.38, \quad 2.1 < M < 2.8, \quad R \simeq 10^5$$

Separating K_D' into wave-drag and skin-friction components and assuming that the skin-friction component varies like

$$\alpha/\sqrt{R_1}, \quad \alpha = \text{constant}$$

then K_D can be written

$$K_D = [0.38 + (\alpha/\sqrt{R_1})] [1 + 2(\delta/d)]^2$$

Finally, from the results of reference 24, $2\delta/d$ is taken in the form

$$2(\delta/d) = \beta/\sqrt{R_1}, \quad \beta = \text{constant}$$

and

$$K_D = [0.38 + (\alpha/\sqrt{R_1})] [1 + (\beta/\sqrt{R_1})]^2 \quad (14)$$

The two assumed constants, α and β, can be evaluated from the experimental data. Taking the values, determined by successive approximations, $\alpha = 0.52$ and $\beta = 1.0$ gave a curve that fitted the experimental data as indicated on Fig. 11.

The equation naturally checks the known experimental value of K_D for large R_1 ($\sim 10^5$), because it was derived as an extrapolation from this value. Moreover, the assigned numerical values of the constants α and β are the order of magnitude that would be expected from boundary-layer theory. For example, the value of β is given in reference 24* as ranging from 0.45 at the stagnation line to 3.2 at a point about 81° downstream (measured between the flow direction and a line passing through the sphere center and the separation point). The value of β is nearly constant for the first 45° of the sphere and then increases rapidly, so that $\beta = 1.0$ seems a reasonable value to characterize an average displacement thickness. The analysis of reference 24 also provides enough information to permit calculation of the approximate magnitude of α. This factor varies from zero at the stagnation point to approximately 1.8 at the 45° point, with a zero pressure gradient (and therefore decreasing local skin friction) at 75°, and, finally, a zero value again at 81° where separation occurs. While it is concluded from the boundary-layer analysis of reference 24 that the value $\alpha = 0.52$ is correct in order of magnitude, a slightly higher value (say, approximately 2.0) would be expected. This suggests possible molecular flow effects, with "slip" reducing the skin-friction coefficient.

Further evidence of molecular flow effects is obtained by comparing these data with drag coefficients obtained in subsonic flow in liquids for the same Reynolds Number range. It was argued previously that the total drag can be separated into wave-drag and skin-friction components. At high R, where the skin-friction effects are small, the wave-drag components are different for supersonic versus subsonic Mach Numbers. If the energy loss in the shock wave at supersonic speeds remains essentially constant as R decreases (M being approximately constant), then one would expect the supersonic and subsonic drag coefficients to follow the same trend when compared on the basis of the same Reynolds Number (R_1 in the supersonic case), provided there were no molecular flow effects. The data would be displaced because of the different wave drags in the two cases but should define essentially parallel curves. This statement neglects compressibility effects, but these are small for cases where $M_1 < 0.5$. The subsonic, incompressible drag data summarized in reference 1 have been plotted on Fig. 11. Examination of this figure shows that the present data do not increase so fast as the subsonic curve and, in fact, cross this curve. A possible explanation is that "slip" effects are decreasing the skin-friction drag in air.

If molecular flow effects are present, it follows that Eq. (14) should break down as R decreases below the limit of the present experimental data, since the equation contains no function of M/R. Moreover, Eq. (14) gives a drag coefficient increasing without limit as R tends to zero, and it is known from kinetic theory that the drag coefficient becomes independent of R in the large mean free path region ($M/R > 10$). The values of K_D computed for this region[11] are included on Fig. 10 for $M = 2$ and 3 (these values are based on assumed equal temperatures of impinging and reflected molecules).

The assumption that the shock wave does not affect the boundary layer is particularly suspected. Fig. 12 shows a typical photograph of the shock wave for a 0.7-in. sphere obtained by a glow method.[26, 27] Similar photographs obtained with air and a 1-in. diameter sphere indicate that the beginning of the shock wave is

* Actually only the boundary-layer thickness is given explicitly in this reference. The displacement thickness was calculated from its definition in terms of the boundary-layer thickness.

approximately 0.1 in. in front of the sphere under conditions where the molecular mean free path is approximately 0.006 in. in the undisturbed flow (Run 43, $M = 2.6$, $R = 700$). The thickness of a laminar boundary layer at the stagnation line (computed from the results of reference 24) would be 0.07 in. If the shock-wave thickness were of the order of magnitude of 10 molecular mean free paths, or 0.06 in., an interaction between the shock zone and the boundary layer might occur.

It will be apparent from the preceding discussion that the available data do not permit separation of viscous, molecular flow, and shock-wave effects. The simplified assumptions made in deducing the form of Eq. (14) imply that only changes in viscous effects are occurring, and this explanation seems to fit the data satisfactorily, at least for $R > 40$. According to the estimates of Tsien,[10] molecular flow effects should be present in this region (since $M/\sqrt{R} \simeq 0.4$). A complete understanding of the relative importance of these various factors requires additional experimental work.

Measurement of drag forces in air at low subsonic speeds ($M < 0.3$) and with R varied over a wide range from a maximum of approximately 400 would permit direct comparison with incompressible flow data. Since there would be no shock wave, deviations from the incompressible flow results would indicate the magnitude of molecular flow effects. By comparing the results of Fig. 11 with these new subsonic data, conclusions regarding interaction between the shock wave and boundary layer might be possible. Measured pressure distributions over the sphere surface would be valuable, but the experimental difficulties are formidable for small models.

Conclusions

(1) Drag coefficients have been measured for spheres in supersonic air streams at low Reynolds Numbers. These previously unavailable data cover a Reynolds Number range (based on the sphere diameter) from approximately 800 to 15, at Mach Numbers from 2.1 to 2.8. The data show a marked increase (by a factor of approximately $2^1/_2$ over the test range) of drag coefficient with decreasing Reynolds Number, whereas available information at supersonic speeds, for $R \simeq 10^5$, could be correlated as a function of Mach Number alone and was independent of Reynolds Number variations.

(2) The precision of the experimental values of the drag coefficient K_D is estimated to be ± 5 per cent. This is the standard deviation of all experimental points from an average curve drawn through them. The use of a cross-stream support has been shown experimentally to give drag coefficients that are approximately 4 per cent lower than the correct values. The effect of systematic errors introduced in the interpretation of probe pressure readings cannot be completely evaluated at this time.

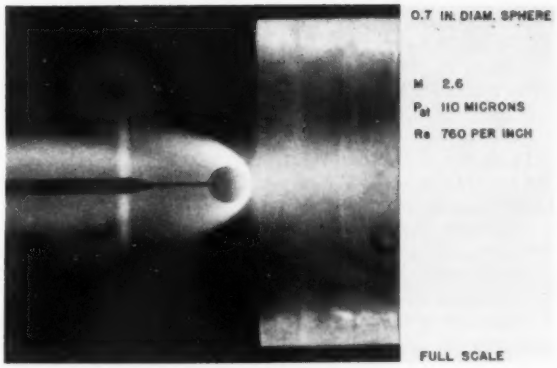

FIG. 12. Flow visualization photograph by glow method.

(3) The data have been correlated, within the limits of the experimental errors, over the entire R range covered in these tests by an equation based on the concept of separation of the total drag into wave-drag and skin-friction components, with the form of the skin-friction component corresponding to an assumed laminar boundary layer up to the separation point. This formulation resulted in a function with two constants, which were determined to give the best fit with the experimental data. Comparison with an available boundary-layer analysis for a sphere indicated that the values of the constants are the same order of magnitude as indicated by the theory. The equation fails for the limiting case of free molecular flow. The limited Mach Number range in the present investigation did not permit conclusions regarding the effect of variable M.

(4) A photograph of the shock wave associated with a sphere indicates that the shock zone may interact with the boundary layer in the vicinity of the stagnation line of the sphere. If such an interaction occurred, the assumptions made in deducing the form of the proposed correlation equation would be incorrect.

(5) Comparison of the data with available drag coefficients for subsonic incompressible flow indicates that molecular flow effects "slip" may have been present for the lower part of the Reynolds Number range. Additional experimental data are required before the relative importance of viscous, molecular flow, and shock-wave effects can be evaluated completely.

References

[1] Goldstein, S., *Modern Developments in Fluid Dynamics*, Vol. 1, Fig. 2, p. 16; also Vol. 2, Fig. 200, p. 493; Oxford, 1938.

[2] Millikan, R. A., *The General Law of Fall of a Small Spherical Body Through a Gas, and Its Bearing upon the Nature of Molecular Reflection from Surfaces*, The Physical Review, Vol. 22, No. 1, July, 1923.

[3] Charters, A. C., and Thomas, R. W., *The Aerodynamic Performance of Small Spheres from Subsonic to High Supersonic*

Velocities, Journal of the Aeronautical Sciences, Vol. 12, No. 4, pp. 468–475, October, 1945.

[4] Lamb, H., *Hydrodynamics*, 6th Ed., pp. 594–617; Cambridge University Press, London, 1932.

[5] Goldstein, S., loc. cit., Vol. 2, pp. 491–499.

[6] Goldstein, S., loc. cit., Vol. 2, p. 492.

[7] Goldstein, S., loc. cit., Vol. 1, p. 17.

[8] Loeb, L. B., *Kinetic Theory of Gases*, p. 214; McGraw-Hill Book Company, Inc., 1934.

[9] Lamb, H., loc. cit., pp. 601–602.

[10] Tsien, H. S., *Superaerodynamics, Mechanics of Rarefied Gases*, Journal of the Aeronautical Sciences, Vol. 13, No. 12, p. 653, December, 1946.

[11] Heineman, M., *Theory of Drag in Highly Rarefied Gases*, Communications on Applied Mathematics, Vol. 1, No. 3, September, 1948.

[12] Stalder, J. R., and Jukoff, D., *Heat Transfer to Bodies Travelling at High Speed in the Upper Atmosphere*, N.A.C.A. T.N. No. 1682, August, 1948.

[13] Ashley, H., *Applications of the Theory of Free Molecule Flow to Aeronautics*, Journal of the Aeronautical Sciences, Vol. 16, No. 2, p. 95, February, 1949.

[14] Schaaf, S. A., Horning, D. O., and Kane, E. D., *Design and Initial Operation of a Low Density Supersonic Wind Tunnel*, presented at Heat Transfer and Fluid Mechanics Institute, Berkeley, June, 1949; published by the American Society of Mechanical Engineers, New York, May, 1949.

[15] Emerson, D. E., *Boundary Layer Corrections in an Axially Symmetric Low Density Supersonic Nozzle*, Master of Science Thesis, University of California, August, 1950.

[16] Cyr, R. R., *A 16-Point Pirani Gage Recorder*, University of California Engineering Research Report HE-150-53, February, 1949.

[17] Kopal, Z., *Tables of Flow of Air Around Cones*, Massachusetts Institute of Technology, Cambridge, 1947.

[18] Liepmann, H. W., and Puckett, A. E., *Aerodynamics of a Compressible Fluid*, p. 77; John Wiley and Sons, Inc., New York, 1947.

[19] *International Critical Tables*, McGraw-Hill Book Company, Inc., New York, 1929.

[20] Keenan, J. H., and Kaye, J., *Thermodynamic Properties of Air*, p. 36; John Wiley and Sons, Inc., New York, 1945.

[21] Liepmann, H. W., and Puckett, A. E., loc. cit., p. 25.

[22] Chambré, P. L., *The Theory of the Impact Tube in a Viscous Compressible Gas*, University of California Engineering Research Report HE-150-50, November, 1948.

[23] Goldstein, S., loc. cit., Vol. 2, pp. 493–496.

[24] Tomotika, S., *The Laminar Boundary Layer on the Surface of a Sphere in a Uniform Stream*, Reports and Memoranda No. 1678, Great Britain, Aeronautical Research Committee, July 12, 1935.

[25] Emmons, H. W., *Gas Dynamics Tables for Air;* Dover Publications, Inc., New York, 1947.

[26] Williams, T. W., and Benson, J. M., *Preliminary Investigation of the Use of Afterglow for Visualizing Low Density Compressible Flows*, N.A.C.A. T.N. No. 1900, June, 1949.

[27] Kane, E. D., *Preliminary Report on an Electrical Discharge Method for Flow Visualization in a Low Density Supersonic Wind Tunnel*, University of California Engineering Research Report HE-150-51, February, 1949.

The Interaction of Shock Waves with Boundary Layers on a Flat Surface

(*Continued from page 238*)

[6] Liepmann, H. W., Roshko, A., and Dhawan, S., *On the Reflection of Shock Waves from Boundary Layers*, N.A.C.A., in press, July, 1949.

[7] Tsien, H. S., and Finston, M., *Interaction Between Parallel Streams of Subsonic and Supersonic Velocities*, Journal of the Aeronautical Sciences, Vol. 16, No. 9, pp. 515–528, September, 1949.

[8] Lees, L., *Interaction Between the Laminar Boundary Layer over a Plane Surface and an Incident Oblique Shock*, Princeton University Aeronautical Engineering Laboratory Report No. 143, January 24, 1949.

[9] Bailey, D. Z., *Design and Operation of a Schlieren System*, Gas Turbine Laboratory, M.I.T., unpublished report.

[10] DeFrate, L. A., Barry, F. W., and Bailey, D. Z., *A Portable Mach-Zehnder Interferometer*, Project Meteor Report No. 51, February, 1950.

[11] Liepmann, H. W., *Investigations of the Interaction of Boundary Layer and Shock Waves in Transonic Flow*, U.S.A.F. Technical Report 5668, Air Materiel Command, February 9, 1948.

The Secondary Flow in a Cascade of Airfoils in a Nonuniform Stream*

H. B. SQUIRE† AND K. G. WINTER

Royal Aircraft Establishment, Farnborough, England

SUMMARY

A method is given of calculating the secondary flow in a cascade of airfoils in a stream with a variation of approach velocity along the span of the airfoils. The results are compared with measurements of the secondary flow at a cascade at a corner in a return-circuit wind tunnel, where the velocity gradient is obtained as a normal consequence of flow through a diffuser. The agreement between theory and experiment is satisfactory and indicates that the theory is sound.

LIST OF SYMBOLS

x, y	= Cartesian coordinates in plane normal to span of cascade
α, β	= orthogonal curvilinear coordinates in (x, y) plane
z	= distance measured along span from one end wall
h	= the following: elements of length in (α, β) coordinates are $h\delta\alpha$ and $h\delta\beta$
r	= radius at any point of passage between two vanes
r_0	= mean radius of passage
$2b$	= width of passage at exit
$2l$	= height of passage at exit
θ	= angle of deflection at corner up to point α
ϵ	= total angle of deflection at corner
$\boldsymbol{v}$	= velocity vector with components u, v, w in directions $\alpha, \beta, z\ (=\gamma)$
U	= velocity of approach to corner
v_1, w_1	= values of v, w downstream of corner
$\boldsymbol{w}$	= vorticity vector with components ξ, η, ζ in directions $\alpha, \beta, z\ (=\gamma)$
ψ	= stream function such that $v_1 = \partial\psi/\partial z, w_1 = -\partial\psi/\partial\beta$
p	= static pressure
ρ	= density

(1) INTRODUCTION

THE EXISTENCE OF SECONDARY FLOW downstream of a cascade of airfoils, in a stream of nonuniform velocity, is well known. It consists usually of a pair of vortices in each passage through the cascade with the character shown in Fig. 1. The extent of the secondary flow depends on the degree of nonuniformity of the approaching stream, and two types of secondary flow can be distinguished. In the first type, the stream is uniform except for a thin boundary layer at the walls. The secondary flow is then limited to layers near the end walls and in the wakes of the cascades. This type of motion has been investigated by Carter and Cohen.[1] In the second type of flow, the stream is nonuniform over a large part of the span of the vanes, as will occur if the cascade is placed at the end of a diffuser in a wind tunnel. The vortices shown in Fig. 1 thus extend over a large part of the cross section and eventually combine to form a pair of large vortices far downstream.

This note deals only with the second type of flow, in which the region of nonuniformity is large compared with the gap between the vanes. In this case, although the nonuniformity of the stream may have been created by frictional effects, the development of the secondary flow system can be considered as being independent of friction and can be calculated from the equations of motion of an ideal fluid.

There is an analogy between the secondary flow and the motion of a gyroscope. If a disc, which is rotating about its axis of symmetry, is turned about an axis in its plane, it develops an angular velocity about a third axis perpendicular to the first two. The analogy with the present problem is obtained by supposing the disc to lie originally in the plane containing the stream direction and the spanwise direction of the cascades. Its original rotation is associated with the velocity gradient along the spanwise direction of the cascades. The disc and the stream are then turned, on passage through the cascade, about an axis along the cascade span. The rotation of the disc about its third axis corresponds to the secondary flow of the character indicated in Fig. 1.

(2) THEORY

(2.1) *General*

For steady flow of an inviscid incompressible fluid, we have the equation[2]

$$\text{curl}\ (\boldsymbol{v} \times \boldsymbol{w}) = 0 \qquad (1)$$

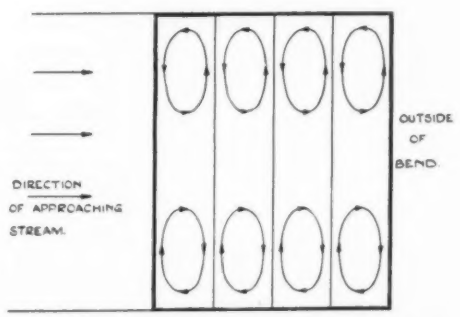

FIG. 1. CHARACTER OF SECONDARY FLOW AT OUTLET OF A CASCADE IN A DUCT.

Received August 14, 1950.

* Published by permission of the Chief Scientist, Ministry of Supply. British Crown Copyright reserved.

† Now at the National Physical Laboratory.

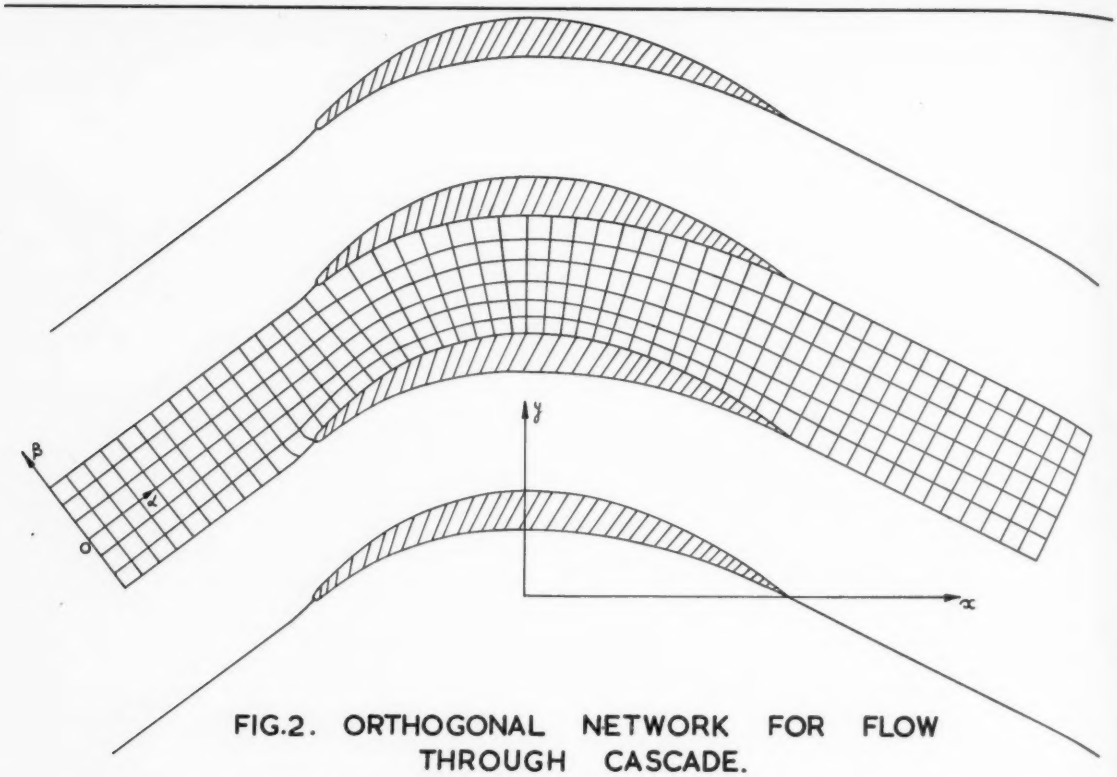

FIG.2. ORTHOGONAL NETWORK FOR FLOW THROUGH CASCADE.

where $\boldsymbol{v}$ is the velocity and $\boldsymbol{w}$ is the vorticity. With orthogonal curvilinear coordinates (α, β, γ), for which the elements of arc are h^1, $\delta\alpha$, $h_2\delta\beta$, $h_3\delta\gamma$, the component velocities are (u, v, w) and the component vorticities are (ξ, η, ζ); the first component of Eq. (1) is

$$\frac{\partial}{\partial\beta}\,[h_3(u\eta - v\xi)] = \frac{\partial}{\partial y}\,[h_2(w\xi - u\zeta)] \qquad (2)$$

Also

$$\text{div } \boldsymbol{v} = 0, \qquad \text{div } \boldsymbol{w} = 0$$

which become, in (α, β, γ) coordinates,

$$\frac{\partial}{\partial\alpha}\,(h_2h_3u) + \frac{\partial}{\partial\beta}\,(h_3h_1v) + \frac{\partial}{\partial\gamma}\,(h_1h_2w) = 0 \qquad (3)$$

$$\frac{\partial}{\partial\alpha}\,(h_2h_3\xi) + \frac{\partial}{\partial\beta}\,(h_3h_1\eta) + \frac{\partial}{\partial\gamma}\,(h_1h_2\zeta) = 0 \qquad (4)$$

From Eq. (2), making use of Eqs. (3) and (4), we obtain

$$\left(\frac{u}{h_1}\frac{\partial}{\partial\alpha} + \frac{v}{h_2}\frac{\partial}{\partial\beta} + \frac{w}{h_3}\frac{\partial}{\partial\gamma}\right)\left(\frac{\xi}{h_1}\right) = \left(\frac{\xi}{h_1}\frac{\partial}{\partial\alpha} + \frac{\eta}{h_2}\frac{\partial}{\partial\beta} + \frac{\zeta}{h_3}\frac{\partial}{\partial\gamma}\right)\left(\frac{u}{h_1}\right) \qquad (5)$$

This equation and two similar ones are Helmholtz's equations in curvilinear coordinates. If the motion is not steady, we have to add a term $(\partial/\partial t)\,(\xi/h_1)$ to the left-hand side of Eq. (5).

We now suppose that the curvilinear coordinates are $\alpha(x, y)$, $\beta(x, y)$, and z, where x and y are Cartesian coordinates in the plane normal to the span of the cascade and z is measured along the span. α is the velocity potential and β is the stream function of the two-dimensional motion that would be present if the approaching stream were uniform (Fig. 2). The flow in one of the passages between the airfoils and its extensions ahead of and behind the airfoils lies between two stream lines β = constant, and we shall restrict consideration to a single passage bounded in this way. Then, for these particular coordinates, α, β, and z $(= \gamma)$, we may put

$$h_1 = h_2 = h, \qquad h_3 = 1 \qquad (6)$$

and the equation of continuity [Eq. (3)] becomes

$$\frac{\partial}{\partial\alpha}\,(hu) + \frac{\partial}{\partial\beta}\,(hv) + \frac{\partial w}{\partial z} = 0 \qquad (7)$$

The quantity h can be regarded as proportional to the reciprocal of the velocity of the two-dimensional flow at any point in the field. We choose the scale of α and β so that h is equal to unity far ahead of the cascade; h will also be equal to unity far behind a cascade that gives a deflection without expansion or contraction.

The vorticity components are[2]

$$\xi = \frac{1}{h_2h_3}\left[\frac{\partial}{\partial\beta}\,(h_3w) - \frac{\partial}{\partial\gamma}\,(h_2v)\right] = \frac{1}{h}\frac{\partial w}{\partial\beta} - \frac{\partial v}{\partial z} \qquad (8)$$

$$\eta = \frac{1}{h_3 h_1}\left[\frac{\partial}{\partial\gamma}(h_1 u) - \frac{\partial}{\partial\alpha}(h_3 w)\right] = \frac{\partial u}{\partial z} - \frac{1}{h}\frac{\partial w}{\partial\alpha} \qquad (9)$$

$$\zeta = \frac{1}{h_1 h_2}\left[\frac{\partial}{\partial\alpha}(h_2 v) - \frac{\partial}{\partial\beta}(h_1 u)\right] = \frac{1}{h^2}\left[\frac{\partial}{\partial\alpha}(hv) - \frac{\partial}{\partial\beta}(hu)\right]$$

We now consider the flow past a cascade for which the approach velocity distribution is nonuniform. Then, if the degree of nonuniformity is not large, the two-dimensional flow referred to above can be regarded as a first approximation to the actual flow. We assume that this is so and shall calculate the actual flow by treating it as a linear perturbation from the two-dimensional flow.

If the approaching stream has velocity U (where U is, in general, a function of β and z, such that the velocity variation is not large), then the vorticity components η and ζ are small quantities of the first order and ξ is zero in the approaching stream. It will be assumed that, on passing through the cascade, the vorticity component ξ becomes a small quantity of the first order.

For the two-dimensional basic motion, we should have

$$hu = U, \qquad v = w = 0 \qquad (10)$$

and, since we are only considering small perturbations on this basic motion, we can regard v and w as small quantities of the first order; also $(\partial/\partial\alpha)\,(hu)$ is a small quantity of the first order, since it is zero for the basic motion [Eq. (7)]. We shall neglect all quantities of the second order in Eq. (5), which becomes, on making use of Eq. (7),

$$\frac{u}{h}\frac{\partial}{\partial\alpha}\left(\frac{\xi}{h}\right) = \frac{\xi}{h}\frac{\partial}{\partial\alpha}\left(\frac{u}{h}\right) + \frac{\eta}{h}\frac{\partial}{\partial\beta}\left(\frac{u}{h}\right)$$

or

$$\frac{\partial}{\partial\alpha}\left(\frac{\xi}{u}\right) = \frac{\eta h}{u^2}\frac{\partial}{\partial\beta}\left(\frac{u}{h}\right) \qquad (11)$$

The second Helmholtz equation gives, to the same order of approximation,

$$(\partial/\partial\alpha)\,(\eta/h) = 0$$

Hence, from Eq. (9),

$$\eta/h = \partial U/\partial z \qquad (12)$$

which is its value in the approaching stream. Substituting from Eqs. (10) and (12) in Eq. (11), we get

$$\frac{\partial}{\partial\alpha}(h\xi) = -2h^2\frac{\partial U}{\partial z}\frac{\partial}{\partial\beta}(\log h)$$

The neglect of the term depending on $\partial U/\partial\beta$ is in accordance with the approximations introduced above.

We now integrate Eq. (11) with respect to α from far upstream to far downstream, obtaining

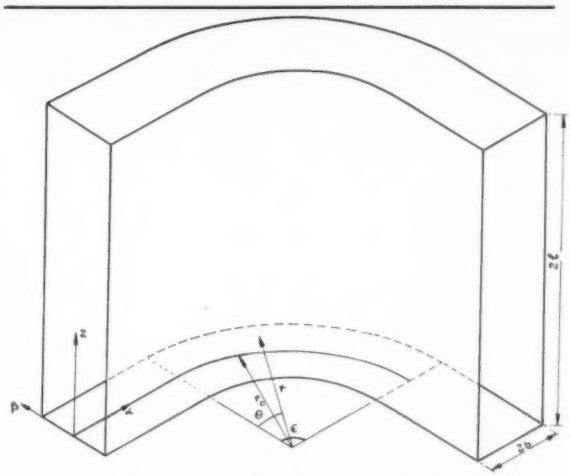

FIG. 3. SKETCH ILLUSTRATING CHANNEL USED TO REPRESENT ONE PASSAGE OF CASCADE.

$$(h\xi)_1 = -2\frac{\partial U}{\partial z}\int_{-\infty}^{\infty} h^2\frac{\partial}{\partial\beta}(\log h)\,d\alpha \qquad (13)$$

where the suffix 1 denotes the value far downstream. This formula enables us to calculate the component vorticity along the stream direction downstream of the cascade.

Since the integration in Eq. (13) is along the stream lines of the basic flow, we can use a crude representation of the basic flow for the calculation of the integral. For this purpose the motion is assumed to be uniform in front of and behind the cascade, with $h = 1$ there; within the passage we assume that the basic motion is the irrotational flow in a circle about a vortex at the center of the circle. For this latter motion,

$$\alpha = r_0\theta + \text{const.}, \quad \beta = r_0 \log (r/r_0), \quad h = r/r_0$$

where r, r_0, and θ are defined as in Fig. 3. Hence,

$$(\partial/\partial\beta)\,(\log h) = 1/r_0$$

and

$$d\alpha = r_0\,d\theta$$

in the passage, and thus

$$\int h^2(\partial/\partial\beta)\,(\log h)\,d\alpha = (r/r_0)^2\theta$$

As a further approximation we shall assume that the width of the passage is small compared with the radius, so that r does not differ greatly from r_0 across the passage. We may then put $r/r_0 = 1$ in the above expression, which becomes

$$\int h^2(\partial/\partial\beta)\,(\log h)\,d\alpha = \theta \qquad (14)$$

For the complete basic motion represented approximately by uniform approach flow, curved flow in the passage bounded by two circular arcs, and uniform flow downstream, we find that the value of ξ in the outflow is, from Eqs. (13) and (14),

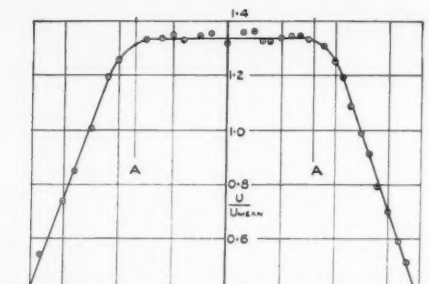

FIG. 4. VELOCITY DISTRIBUTION, APPROACHING FIRST CORNER OF 4'x3' WINDTUNNEL.

$$\xi_1 = \frac{\partial w_1}{\partial \beta} - \frac{\partial v_1}{\partial z} = -2\epsilon \frac{\partial U}{\partial z} \tag{15}$$

where ϵ (Fig. 3) is the total angle of deflection of the stream; we have put $h = 1$ downstream of the bend, and v_1, w_1 are the β, z components of velocity far downstream. *Thus, the axial vorticity in the stream leaving the cascade is equal to the velocity gradient in the approaching stream multiplied by twice the angle of deflection.*

If the motion settles down to a steady secondary flow far downstream superposed on the general stream, we shall have $\partial u/\partial \alpha = 0$ in Eq. (7), so that the equation of continuity becomes

$$(\partial v_1/\partial \beta) + (\partial w_1/\partial z) = 0 \tag{16}$$

Introducing a stream function of the secondary motion defined by $v_1 = \partial \psi/\partial z$ and $w_1 = -\partial \psi/\partial \beta$, Eq. (16) is satisfied and Eq. (15) becomes

$$(\partial^2 \psi/\partial \beta^2) + (\partial^2 \psi/\partial z^2) = 2\epsilon(\partial U/\partial z) \tag{17}$$

It is assumed that there is no flow across the extensions of the cascades denoted by $\beta = \pm b$ (Fig. 3) or at the end walls $z = 0$, $z = 2l$, so that the boundary conditions may be taken to be $\psi = 0$ for $\beta = \pm b$ and for $z = 0, z = 2l$.

The theory given above is a development of the theory of von Kármán and Tsien for small deflections;[3] there are differences between the two theories with regard to the retention of some second-order terms.

(2.2) *Solution for a Bend of High Aspect Ratio*

If the width of the passage is small compared with the height, the secondary flow will be mainly parallel to the span of the airfoils except near the end walls. The solution of Eq. (17) corresponding to this type of flow is

$$\left.\begin{aligned} \psi &= (\beta^2 - b^2)\epsilon(\partial U/\partial z) \\ v_1 &= (\beta^2 - b^2)\,\epsilon\,(\partial^2 U/\partial z^2) \\ w_1 &= -2\beta\epsilon\,(\partial U/\partial z) \end{aligned}\right\} \tag{18}$$

provided that $b^2(\partial^3 U/\partial z^3)$ is negligible in comparison with $\partial U/\partial z$; for the velocity distribution considered below, this condition is satisfied except near the stations marked A in Fig. 4.

The expression (18) may be regarded as a particular integral of Eq. (17) and is the required solution away from the end walls and from A (Fig. 4). Near the end wall $z = 0$, we have to add a complementary function to this particular integral to satisfy the boundary condition there. This complementary function is the well-known "surface-wave" type of solution of Laplace's equation, and the complete integral is

$$\psi = (\beta^2 - b^2)\epsilon \frac{\partial U}{\partial z} + \sum_{n=0}^{\infty} B_n \exp\left[-\frac{(2n+1)\pi z}{2b}\right] \cos\left[\frac{(2n+1)\pi \beta}{2b}\right] \tag{19}$$

This form satisfies the condition $\psi = 0$ for $\beta = \pm b$, and the coefficients B_n are determined by the condition $\psi = 0$ for $z = 0$. Putting $z = 0$, $\psi = 0$ in Eq. (19), we obtain

$$(\beta^2 - b^2)\epsilon \left(\frac{\partial U}{\partial z}\right)_{z=0} + \sum_{n=0}^{\infty} B_n \cos\left[\frac{(2n+1)\pi\beta}{2b}\right] = 0$$

Hence,

$$B_n = \frac{32\,(-)^n b^2 \epsilon}{(2n+1)^3\,\pi^3} \left(\frac{\partial U}{\partial z}\right)_{z=0}$$

so that the coefficients decrease rapidly with increase of n.

We may thus, to the order of accuracy with which we are concerned, neglect all except the first term in the series, in which case we may replace the form (19) by the expression

$$\psi = (\beta^2 - b^2)\epsilon \frac{\partial U}{\partial z}\left[1 - \exp\left(-\frac{\pi z}{2b}\right)\right] \tag{20}$$

The values of the two component velocities are, then,

$$v_1 = \frac{\pi}{2b}(\beta^2 - b^2)\epsilon \frac{\partial U}{\partial z} \exp\left(-\frac{\pi z}{2b}\right) + (\beta^2 - b^2)\epsilon \frac{\partial^2 U}{\partial z^2}\left[1 - \exp\left(-\frac{\pi z}{2b}\right)\right] \tag{21}$$

$$w_1 = -2\beta\epsilon \frac{\partial U}{\alpha z}\left[1 - \exp\left(-\frac{\pi z}{2b}\right)\right] \tag{22}$$

Eqs. (20), (21), (22) are valid for the upper half of the channel.

(3) Experiments

An experimental check of the theory was made at the first bend of the R.A.E. 4- by 3-ft. Wind Tunnel. The velocity distribution approaching the corner

(Fig. 4) is such as to give an almost linear variation of velocity for the first 15 in. away from the wall. The center passage of the cascade, which has a span of 6 ft. and a width $2b = 4.8$ in., was used. The experiments consisted of measurements with a yawmeter of the angles of deflection of the stream in the β and z directions. The traverses covered the upper part of the span of the turning vanes over which the approach velocity variation was appreciable. Because of the uncertainty of the main stream velocity, the angles were obtained by reading the pressure difference between the two tubes of the yawmeter for several angular settings and interpolating for zero difference. The slopes of the curves then also give the local velocity.

To avoid interference from neighboring passages, the trailing edge of the outer of the two turning vanes enclosing the center passage was extended as shown in Fig. 5. The heads of the yawmeter were inserted about $^1/_4$ in. into this passage.

(4) Comparison of Experiments with Theory

A direct comparison of the measured secondary velocities with the theoretically predicted values is given in Figs. 6 and 7. Fig. 6 shows the velocities in the spanwise direction; Fig. 7 shows those normal to the span. In both cases the velocities are made nondimensional by dividing by the mean speed U_M across the tunnel section approaching the corner.

The theoretical values of v_1 and w_1 are given by Eqs. (21) and (22), using the velocity distribution given in Fig. 4.

It will be seen in Fig. 6 that agreement between theory and experiment is good. In Fig. 7, the agreement in the nonlinear region is not so good, though one might say that the experimental curve is a smoothed-

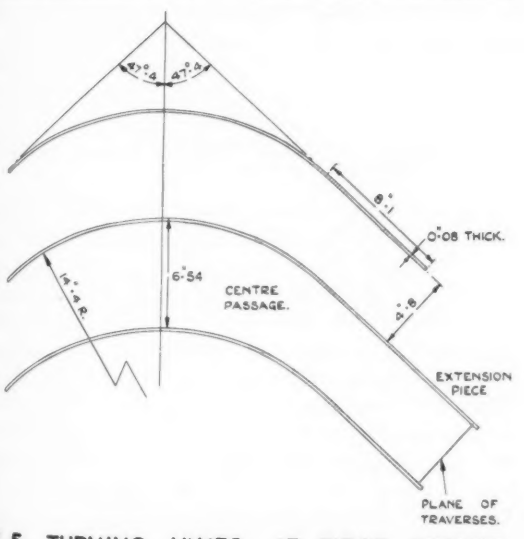

FIG. 5. TURNING VANES AT FIRST CORNER OF 4′×3′ WIND TUNNEL.

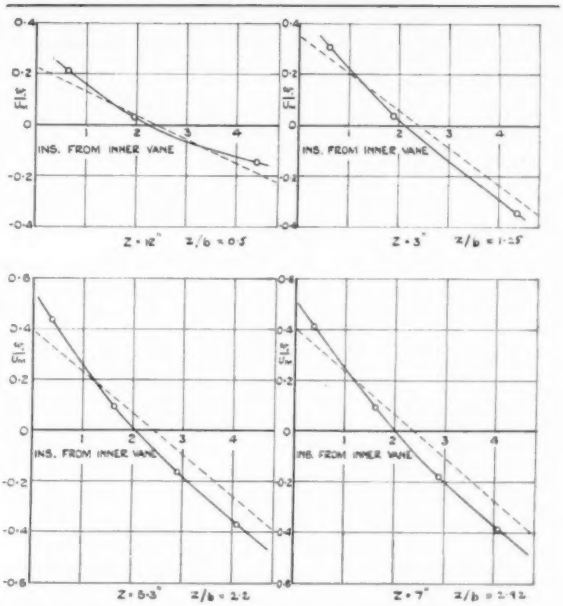

Z = CO-ORDINATE ALONG SPAN OF TURNING VANES MEASURED FROM TUNNEL ROOF.
w_1 = VELOCITY IN Z DIRECTION.
U_m = MEAN VELOCITY OF FLOW APPROACHING BEND.
—— MEASUREMENTS
---- THEORY.

FIG. 6. SECONDARY FLOW IN SPANWISE DIRECTION COMPARISON OF THEORY & EXPERIMENTS.

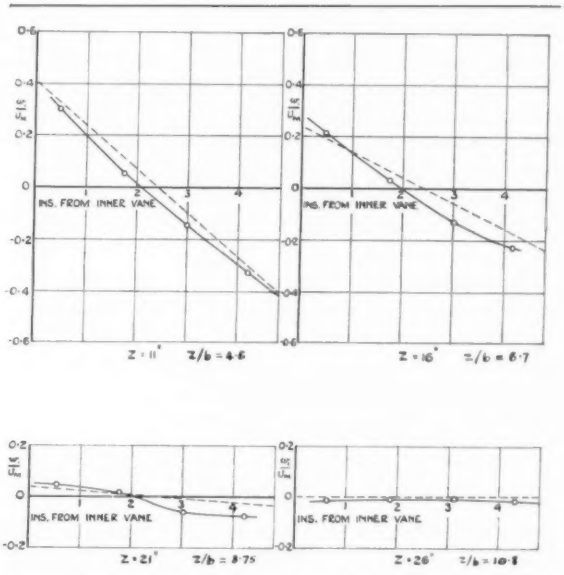

Z = CO-ORDINATE ALONG SPAN OF TURNING VANES MEASURED FROM TUNNEL ROOF.
w_1 = VELOCITY IN Z DIRECTION.
U_m = MEAN VELOCITY OF FLOW APPROACHING BEND.
—— MEASUREMENTS.
---- THEORY.

FIG. 6 (CONT.) SECONDARY FLOW IN SPANWISE DIRECTION — COMPARISON OF THEORY & EXPERIMENTS.

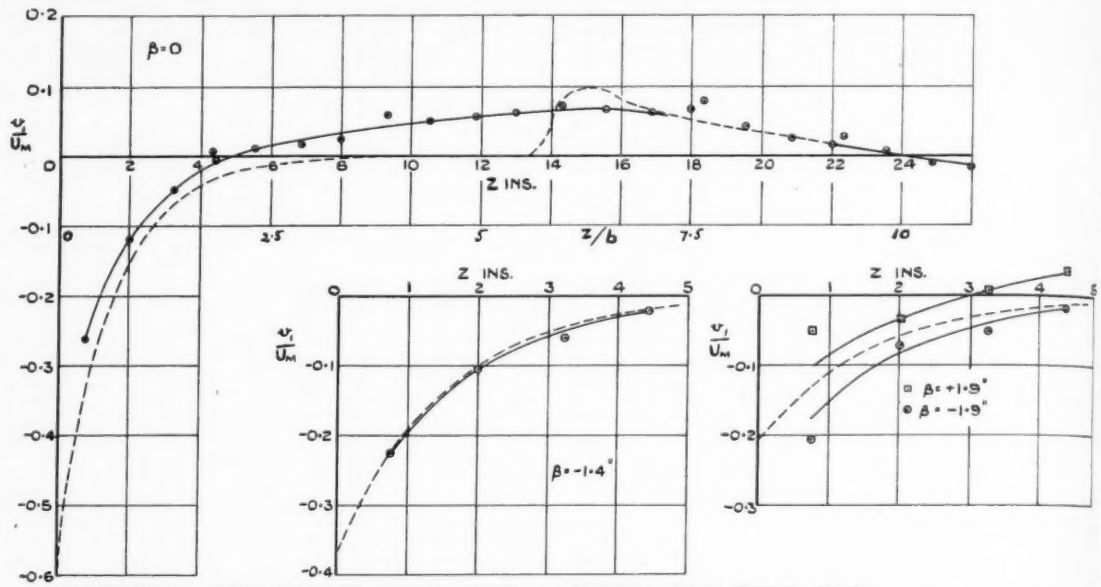

Z= CO-ORDINATE ALONG SPAN OF TURNING VANES MEASURED FROM TUNNEL ROOF
β= CO-ORDINATE NORMAL TO SPAN OF TURNING VANES. ZERO AT CENTRE OF GAP & POSITIVE TOWARDS OUTSIDE OF BEND.
v_1 = SECONDARY VELOCITY IN β DIRECTION.
U_M = MEAN VELOCITY OF FLOW APPROACHING BEND
——— MEASUREMENTS. ------ THEORY.

FIG. 7. SECONDARY FLOW NORMAL TO SPAN — COMPARISON OF THEORY & EXPERIMENTS.

out version of the theoretical curve. This really means that second-order effects are coming into play. The exponential decay law predicted near the end wall is followed closely.

In Fig. 8, a complete comparison of experiment with theory over the whole region considered is given by plotting the stream lines of the lateral motion—i.e., the lines ψ = constant. The values of ψ appropriate to each stream line have been made nondimensional by dividing up $U_M b$. The theoretical stream lines are given by Eq. (20) using the velocity distribution of Fig. 4.

The experimental stream lines have been obtained by integration of the secondary flow velocities. Except in the region near the end wall, the steps in the process are as follows: We choose the stream line along the boundaries of each passage as $\psi = 0$. Then, the value of ψ at any point (β, z) is given by

$$\psi = -\int_{-b}^{\beta} w_1 \, d\beta$$

where the integration is performed at z = constant. In order that both vanes bounding a passage shall be stream lines, it is necessary that

$$\int_{-b}^{b} w_1 \, d\beta = 0$$

for z = constant, and this condition was satisfied by adjusting the zero of the measurements. The maximum adjustment required was a change of the zero of w_1/U_M of 0.04.

Near the end wall the stream lines were obtained from the integral $\int_0^z v_1 \, dz$. To join the stream lines the values of ψ given by the w_1 measurements were plotted against z and the value of z taken, for which ψ is a maximum. Call these values z_0, ψ_0. At z_0 since $\partial\psi/\partial z = 0$, the value of v_1 must be adjusted to zero and ψ will then be given by

$$\psi = \psi_0 + \int_{z_0}^{z} v_1 \, dz$$

The maximum adjustment required was a change of zero of v_1/U_M of 0.04.

The differences between theory and experiment are more apparent in Fig. 8, the maximum value of $-\psi/U_M b$ being 0.255 from the measurements and 0.204 from the calculations. However, the general characteristics of the flow are the same and the experiments confirm that the physical basis of the theory is sound. The discrepancies can be attributed to the second-order effects, which have been neglected in the theory. For example, consider an angular deflection of the flow of 25° at the end of a passage. Assuming this deflection to grow linearly round the curved part of a passage, then the lateral deviation of a stream line through the passage is about 8 in. This deviation is sufficient to modify the velocity gradient appreciably, and, in fact, the

measurements show that the velocity gradient along the centerline of the passage becomes reversed for the first 5 in. away from the wall.

(5) Induced Drag

The power loss associated with the secondary flow is given by

$$\frac{\rho}{2}\int_0^{2l}\int_{-b}^{b} U(v_1^2 + w_1^2)\, d\beta\, dz$$

We may therefore define an induced drag pressure drop coefficient

$$C_{pi} = \frac{1}{4bl}\int_0^{2l}\int_{-b}^{b}\frac{U}{U_M}\left[\left(\frac{v_1}{U_M}\right)^2 + \left(\frac{w_1}{U_M}\right)^2\right] d\beta\, dz$$

C_{pi} has been calculated both by integration of the measured secondary flow and from the theoretical distributions. The respective values are 0.032 and 0.019. The measured value is thus of the order of half the profile drag pressure drop coefficient and should be taken into account in estimating corner loss.

It is possible that there is some recovery of the energy in the secondary flow when mixing between the flows from adjacent passages takes place, and in the case of a wind tunnel there may be some recovery at subsequent corners. However, it is unlikely that this recovery would exceed 50 per cent.

(6) Conclusion

The experiments show that the theory gives a good approximation to the secondary flow in a cascade with a 90° corner and a large variation of approach velocity.

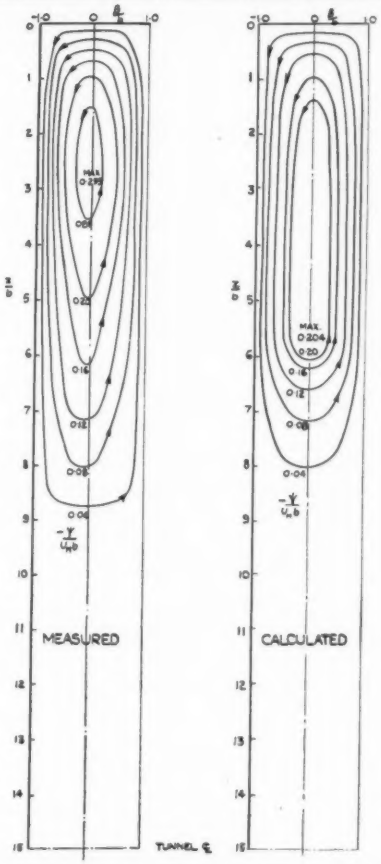

FIG. 8. COMPARISON OF MEASURED & CALCULATED SECONDARY FLOW STREAMLINES IN PASSAGE BETWEEN TWO TURNING VANES.

References

[1] Carter and Cohen, *Preliminary Investigation into the Three-Dimensional Flow Through a Cascade of Aerofoils*, Aero. Res. Council, R. & M. 2336, 1946.

[2] Goldstein (Ed.), *Modern Developments in Fluid Dynamics;* Oxford, 1938.

[3] von Kármán and Tsien, *Lifting-Line Theory for a Wing in Non-Uniform Flow*, Quart. Appl. Math., Vol. III, p. 1, April, 1945.

Free and Forced Vibrations of Rotating Blades

ROBERT PLUNKETT*

The Rice Institute

SUMMARY

The matrix equations governing transverse vibration of a rotating twisted cantilever beam, such as an airplane propeller or turbine blade, are developed. From these equations the variation in natural frequency with rotational speed may be found, and some simplified methods for finding these curves are shown. The same approach is used for the case of forced vibrations of a blade due to oscillating loading, and the case of vibration in an airplane propeller due to yaw is considered as an example. It is shown that this approach can be expected to give results within about 10 per cent of experimentally measured ones if a rather simplified determination of the aerodynamic forces is permissible, as it is in normal flight.

INTRODUCTION

THE VARIATION OF NATURAL FREQUENCY of lateral vibration of a propeller or turbine blade with rotating speed is of evident interest in design. This relationship is both complicated and extremely tedious to calculate. The methods in present use are the Rayleigh or energy method[1, 2] and the Myklestad method.[3] The first of these suffers from being only an approximation to the frequency and from the necessity of guessing a mode shape. The second may well be compared with the proposed approach. However, insofar as is known to the author, this is the first attempt to analyze an arbitrary blade[4] with due regard to rotating speed, twist, and blade angle at the same time, although either of the two methods named above could be modified to take these factors into account. The principal drawback of the Myklestad method is that it inherently loses significant figures—that is, it is necessary to carry more than six significant figures in the untwisted case and more than twelve in the twisted one[5] to get two-figure accuracy in the answer.

The Southwell approach leads to the relationship

$$\omega^2 = \omega_0^2 + a\Omega^2$$

where ω is the natural frequency of vibration, ω_0 is the natural frequency at standstill, and Ω is the rotational speed in rad. per sec.; a is sometimes taken to be a constant[6, 7] but should be considered as a function of Ω. Fortunately, this turns out to be practically the same relationship for all similar blades, so that once the curves are drawn for one blade the results may be easily applied to all blades of that family. It should be recognized, however, that a, the Southwell factor, may vary within wide limits even under present-day operating conditions, and, as blades become more limber and are rotated at faster speeds, this will become of more importance.

Received April 29, 1950. Revised and received July 28, 1950.

* Assistant Professor of Mechanical Engineering.

EQUATIONS

In a recent paper,[5] the author has derived a set of matrix equations that closely describe the deflection of a rotating blade caused by a known transverse force. By a well-known application of D'Alembert's principle, these may be used to find the equations governing the behavior of a rotating blade vibrating transversely. Since the vibration, to the first order, is sinusoidal, the maximum deflection, ignoring damping, is one that would be caused by transverse forces equal to the mass times the square of the vibration frequency times the local amplitude of vibration.[8]

In the ensuing paper, the same notation as that of the author's previous paper will be used, and the equations will be numbered consecutively with it; all equations numbered less than 10 or X appear in the first paper. In accordance with the above, the transverse force in the x-direction [Eq. (4f)] is

$$F_{xj}\delta = \omega^2 u_{xj} m_j \tag{10a}$$

Where u_{xj} is the amplitude of vibration in the x-direction at the point j, ω is the frequency of vibration in radians per unit time, and m_j is the mass per length δ. The transverse force in the y-direction is, similarly,

$$F_{yj}\delta = \omega^2 u_{yj} m_j \tag{10b}$$

From this it is found from Eq. (4f) that the column vector of bending moments due to inertia forces causing vibration is

$$M_0 = \omega^2\delta \begin{Vmatrix} m_x - m_y & 0 \\ 0 & m_x - m_y \end{Vmatrix} u \tag{10c}$$

where m_x and m_y are defined by Eqs. (4e). Now from this and Eq. (IV), it may be seen that

$$M = \Omega^2\delta \begin{Vmatrix} m_x & 0 \\ 0 & m_y \end{Vmatrix} u + \omega^2\delta \begin{Vmatrix} m_x - m_y & 0 \\ 0 & m_x - m_y \end{Vmatrix} u = \delta(\Omega^2 m_\Omega + \omega^2 m_\omega)\, u \tag{10d}$$

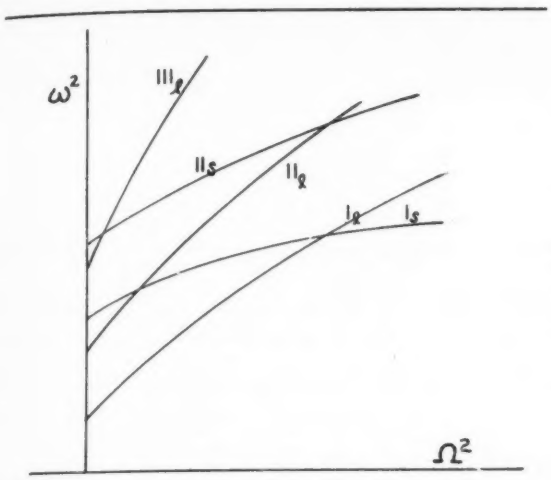

FIG. 1. Variation of natural frequency with rotating speed.

where m_Ω of this paper corresponds to m of the previous paper. By the same process as was used in finding Eq. (V),

$$M_p = \frac{\delta^3}{E}\theta[(\Omega^2 m_\Omega + \omega^2 m_\omega)\Delta]\theta^{-1}I_p{}^{-1}M_p \qquad (X)$$

$$M_p = (\omega^2 C + \Omega^2 D)M_p \qquad (XA)$$

which defines the $2n \times 2n$ square matrices C and D. In using Eq. (X) to find the natural frequencies, given numerical values of Ω, it will be found that the calculations for those vibrations that involve displacement primarily in the limber direction are made simpler by the fact that the coefficients for the stiff directions are so small as to be negligible. Thus, for these cases, the effective matrices reduce to n by n in size, reducing the work by a factor of 4.[5]

As a practical matter, only the smallest values of ω^2 are of interest; to find these, it is simpler to divide Eq. (X) through by ω^2.

$$(1/\omega_r{}^2)M_{pr} = [C + (\Omega^2/\omega_s{}^2)D]M_{pr} \qquad (XB)$$

where for a given value of Ω, ω_r is one of the natural frequencies and M_{pr} is the corresponding column vector of moments.

Then, for any value of the ratio Ω^2/ω^2, iteration will lead to the largest values of $1/\omega^2$ or the smallest of ω^2. Some of these values may be negative, and these are of no physical significance; they may be eliminated by the usual trick of adding a corresponding constant to the main diagonal terms of $[C + (\Omega^2/\omega^2)D]$. If

$$Qu = \lambda u$$
$$(Q + \mathcal{I}k)u = (\lambda + k)u$$

and all negative roots may be made smaller in absolute value than any positive roots by a suitable choice of k. To find the next lower value of $1/\omega^2$, it is necessary to use the orthogonality condition

$$\chi_{ps}M_{pr} = M_{ps}{}'I^{-1}M_{pr} = 0$$

which will be proved later, Eq. (XIIB).[9, 11]

$\omega^2 - \Omega^2$ contours

In certain cases it is sufficient to know the natural frequencies at a given rotational speed, in which case the above analysis is sufficient; but often it is desired to know the functional relationship between ω^2 and Ω^2.[6] From physical considerations it is possible to show that this relationship is a series of curves or contours such as are shown in Fig. 1. It should be emphasized that these curves are purely qualitative.

The requirement for a solution of Eq. (XA) is that the determinant be zero or

$$|\omega^2 C + \Omega^2 D - \mathcal{I}| = 0 \qquad (11a)$$

where $\mathcal{I}$ is the appropriate unit matrix. This is a $(2n)$th order polynomial in ω^2 and Ω^2 and their cross-products. It is not difficult to show that Eq. (11a) or, alternatively, Eq. (XA) is a positive definite form, so that for any positive value of Ω^2 this must have $2n$ positive roots of ω^2, where one or more of the roots may be multiple. The multiple roots correspond to the points where the curves of Fig. 1 cross; thus, there are a total of $2n$ such curves. Physical reasoning shows that I_l, II_l, and III_l are the curves for the first three modes of vibration in the limber direction and I_s and II_s are the first two modes in the stiff direction.

While it would be possible to calculate the values of ω^2 for a series of values of Ω^2 and thus plot the curves, there are ways of making this process a little easier. A more accurate curve may be drawn through a given number of points if the slopes are also known at these points. This slope is $\partial\omega^2/\partial\Omega^2$; in finding it, it is necessary to deal with the row vector, as well as the column vector, M_p—i.e.,

$$M_{pr} = (\omega_r{}^2 C + \Omega^2 D)M_{pr} \qquad (11b)$$

defines the column vector and

$$\chi_{pr} = \chi_{pr}(\omega_r{}^2 C + \Omega^2 D) \qquad (11c)$$

defines the row vector corresponding to a certain natural frequency ω_r for a given Ω^2. Differentiating Eq. (11b) with respect to Ω^2,

$$\frac{\partial M_{pr}}{\partial\Omega^2} = \left(\frac{\partial\omega_r{}^2}{\partial\Omega^2}C + D\right)M_{pr} + (\omega_r{}^2 C + \Omega^2 D)\frac{\partial M_{pr}}{\partial\Omega^2} \qquad (11d)$$

Premultiplying by χ_{pr},

$$[\chi_{pr} - \chi_{pr}(\omega_r{}^2 C + \Omega^2 D)]\frac{\partial M_{pr}}{\partial\Omega^2} = \chi_{pr}\left(\frac{\partial\omega_r{}^2}{\partial\Omega^2}C + D\right)M_{pr} \qquad (11e)$$

The left-hand side is zero by Eq. (11c) and

$$\partial\omega_r{}^2/\partial\Omega^2 = \chi_{pr}DM_{pr}/\chi_{pr}CM_{pr} \qquad (XI)$$

The numerator and denominator of the right-hand side are both scalors.

χ_p may be found directly from M_p. Forming the transposed of Eq. (11b),

$$M_{pr}' = M_{pr}'(\omega_r{}^2C + \Omega^2D)' \tag{12a}$$

But, Eqs. (X) and (XA),

$$(\omega^2C + \Omega^2D) = (\delta^3/E)\theta(\omega^2m_\omega + \Omega^2m_\Omega)\,\Delta\theta^{-1}I^{-1}$$

or

$$(\omega^2C + \Omega^2D)' = (\delta^3/E)I^{-1}{}'\theta^{-1}{}'[(\omega^2m_\omega + \Omega^2m_\Omega)\,\Delta]'\theta' \tag{12b}$$

however,

$$I^{-1}{}' = I^{-1} \tag{12c}$$

thus,

$$[(\omega^2m_\omega + \Omega^2m_\Omega)\,\Delta]' = [(\omega^2m_\omega + \Omega^2m_\Omega)\,\Delta] \tag{12d}$$

since these are symmetrical matrices; and, Eq. (3c),

$$\theta^{-1}{}' = \theta$$

or

$$(\omega^2C + \Omega^2D)' = (\delta^3/E)I^{-1}\theta \times [(\omega^2m_\omega + \Omega^2m_\Omega)\,\Delta]\theta^{-1} = I^{-1}(\omega^2C + \Omega^2D)I \tag{12e}$$

Substituting from Eq. (12e) into Eq. (12a)

$$M_{pr}'I^{-1} = M_{pr}'I^{-1}(\omega^2C + \Omega^2D) \tag{12f}$$

By a comparison of Eq. (10f) with Eq. (9c),

$$\chi_{pr} = M_{pr}'I^{-1}, \qquad M_{pr}' = \chi_{pr}I \tag{XIIA}$$

It may be shown that [reference 10, p. 77, Eq. (11)]

$$\chi_{ps}M_{pr} = 0 \quad (r \neq s) \tag{12g}$$

where χ_{ps} is the row vector corresponding to the natural frequency $\omega_s{}^2$ and M_{pr} is the column vector corresponding to $\omega_r{}^2$; or

$$M_{ps}I^{-1}M_{pr} = 0 \tag{XIIB}$$

Asymptotes

Since the equation for ω^2 vs. Ω^2 is a $(2n)$th order polynomial leading to $2n$ curves, these curves must be asymptotic to straight lines for large values of Ω^2. Since these asymptotes are rather easily found, they make the plotting of the curves simpler. It may be shown that the curves of the actual propeller will be asymptotic to lines that have the same slope as our finite solution but somewhat different intercepts; however, this does not lessen their value for practical plotting purposes. It would be possible to find the slopes of these asymptotes by evaluating Eq. (XI) for large values of Ω^2, but there is an easier way. The asymptotes have the equations

$$\omega_r{}^2 = b_r\Omega^2 + k_r \tag{13a}$$

From the definition of an asymptote, these equations must be approached by the polynomial as $\Omega^2 \to \infty$. Substituting this expression into Eq. (11c),

$$\chi_{pr} = \chi_{pr}[\Omega^2(b_rC + D) + k_rC] \tag{13b}$$

As $\Omega^2 \to \infty$, this becomes

$$\chi_{pr}(b_rC + D) \to 0 \tag{13c}$$

$$-\chi_{pr}b_rC = \chi_{pr}D$$

$$-\chi_{pr}CD^{-1} = (1/b_r)\chi_{pr} \qquad (\Omega^2 \to \infty) \tag{13d}$$

Letting [Eq. (IIIA)]

$$\chi_p = \chi\theta^{-1}, \qquad \chi = \chi_p\theta \tag{13e}$$

Then, from Eqs. (11c), (X), and (XA),

$$\chi_r = \chi_r(\delta^3/E)(\omega_r{}^2m_\omega + \Omega^2m_\Omega)\,\Delta\theta^{-1}I^{-1}\theta \tag{13f}$$

So that Eq. (13d) becomes

$$-\chi_rm_\omega m_\Omega{}^{-1} = (1/b_r)\chi_r \tag{XIIIA}$$

$m_\omega m_\Omega{}^{-1}$ is rather easily found since m_x is a triangular matrix, Eq. (4e). Since

$$m_\Omega{}^{-1} = \begin{Vmatrix} m_x{}^{-1} & 0 \\ 0 & m_y{}^{-1} \end{Vmatrix}$$

then

$$m_\omega m_\Omega{}^{-1} = \begin{Vmatrix} (\mathcal{I} - m_ym_x{}^{-1}) & 0 \\ 0 & (m_xm_y{}^{-1} - \mathcal{I}) \end{Vmatrix}$$

$m_y{}^{-1}$ may be found from Eq. (4e) by normal methods and gives

$$\left.\begin{aligned} (m_y{}^{-1})_{ij} &= 0 && (j < i) \\ &= + \frac{1}{\sum_{j+i}^{n} km_k} && (j = i) \\ &= \frac{-1}{\sum_{j}^{n} km_k} + \frac{1}{\sum_{j+i}^{n} km_k} && (j > i) \\ & && (i,j = 0,1,2,\ldots,n-1) \end{aligned}\right\} \tag{13g}$$

and $m_\omega m_\Omega{}^{-1}$ is found by the usual matrix multiplication. An additional advantage of using χ_r instead of χ_{pr} arises from the fact that, since these refer only to large values of Ω^2 and the beam stiffness is inoperative, the only possible directions of vibration are in the plane of rotation or out of the plane of rotation. Thus, letting

$$\chi_r = \{\chi_{xr}, \chi_{yr}\}$$

then either $\chi_{xr} = 0$ or $\chi_{yr} = 0$, and Eq. (XIIIA) becomes

$$\left.\begin{aligned} -\chi_{xr}(\mathcal{I} - m_ym_x{}^{-1}) &= (1/b_{xr})\chi_{xr} \\ -\chi_{yr}(m_xm_y{}^{-1} - \mathcal{I}) &= (1/b_{yr})\chi_{yr} \end{aligned}\right\} \tag{XIIIB}$$

It may be seen that since

$$-(g - m_y m_x^{-1})^{-1} + g = -(m_x m_y^{-1} - g)$$

then

$$\chi_{xr} = \chi_{yr}$$

and

$$b_{yr} = b_{xr} + 1 \tag{13h}$$

χ_{yr} is found from Eq. (XIIIB), χ_{pr} may be found from Eq. (13e), and M_{pr} may be found from Eq. (XIIA).

The above give the values of b_r, χ_{pr}, and M_{pr} which are used to find the k_r. The determinant of the square matrix in Eq. (13b) must be zero, or

$$|\Omega^2(b_r C + D) + k_r C - g| = 0 \tag{14a}$$

Expanding this in powers of Ω^2,

$$H_n\Omega^{2n} + H_{n-1}\Omega^{2(n-1)} + H_{n-2}\Omega^{2(n-2)} + \ldots + H_0 = 0 \tag{14b}$$

It is easily seen that

$$H_n = |m_r C + D|$$

But this is zero by Eq. (12c) for the selected values b_r. Thus, Eq. (14b) may be written

$$H_{n-1} + 0(\Omega^{-2}) = 0$$

or

$$H_{n-1} = 0, \quad \Omega^2 \to \infty \tag{14c}$$

But

$$H_{n-1} = -\sum_{i=0}^{n-1} G_{ii} + k_r \sum_{i=0}^{n-1}\sum_{j=0}^{n-1} C_{ij} G_{ji} = 0 \tag{14d}$$

where G_{ji} is the element in the jth row of the ith column of the adjoint of $(b_r C + D)$ as defined in reference 10, page 21. However,

$$G_{ij} = M_{pi}\chi_{pj} \tag{14e}$$

[reference 10, page 61, Eq. (3.5D)]. Thus, substituting from Eq. (14c) into Eq. (14d),

$$k_r = \chi_{pr} M_{pr} / \chi_{pr} C M_{pr} \tag{XIV}$$

Arnoldi[12] has worked out a similar method to find the effect of small changes in blade angle on the natural frequency. The final equation is

$$\partial\omega_r^2/\partial\beta = -2\chi_{pr} J M_{pr} / \chi_{pr} C M_{pr} \tag{XIVA}$$

where β is the pitch angle and

$$J = \begin{Vmatrix} 0 & g \\ -g & 0 \end{Vmatrix}$$

It will be noted that the denominator is already used in Eq. (XIV) and that the numerator involves the scalor product of rows and columns only. To be explicit,

$$\{\chi_{xr}, \chi_{yr}\} J = \{-\chi_{yr}, \chi_{xr}\}$$

Forced Vibrations

Another important problem is to find the response of a rotating blade to aerodynamic forces that vary sinusoidally with time. If the intensity of these forces per unit length of blade is known, it is not difficult to calculate the variable bending moments in the x and y directions. Letting

$$\left.\begin{aligned} M_{x0}(z, t) &= M_{x0}(z) \cos \omega t \\ M_{y0}(z, t) &= M_{y0}(z) \cos \omega t \end{aligned}\right\} \tag{15a}$$

then, in matrix notation, as before,

$$M_0 = \begin{Bmatrix} M_{x0} \\ M_{y0} \end{Bmatrix} \tag{15b}$$

where M_0 is the bending moment due to the amplitude of the applied vibratory forces only. Then it may be seen that [Eq. (XA)]

$$M_p = (\omega^2 C + \Omega^2 D) M_p + \theta M_0 \tag{XV}$$

where ω is now the frequency of the applied forces. This may be solved by iteration—i.e., assume a value of M_p, substitute in the right hand side, and take this solution as a new assumption for M_p. Unfortunately, this simple process will not always converge but may be made to converge by an averaging technique.[14] Eq. (XV) gives only the vibratory moments; the steady-state values may be found by a similar technique.[5]

A practical example of the above is given by an airplane whose propeller axis makes an angle of yaw with the direction of the wind velocity. Because of this angle, the lift on the propeller varies with a frequency equal to the frequency of rotation; the most difficult job is to find M_0. An extensive discussion of how to find the variable lift on the propeller due to the yaw angle above is found in reference 13, but it may be simply stated as finding the lift, assuming a succession of steady-state lift conditions. It is necessary to consider the change in lift caused by twist of the blade, since the aerodynamic forces act at approximately the quarter chord point and not at the elastic axis; this twist effect can change the total vibratory lift by as much as 25 per cent for a normal propeller in use today. A method of analyzing this condition is demonstrated in reference 13, and a numerical solution to the forced vibration problem is also worked out and compared with experimentally determined values. The difference between the calculated value and the experimental value is 6 per cent. A total of nine cases calculated from these principles by a slightly different procedure shows an error of less than 20 per cent in six of them and errors between 20 per cent and 31 per cent in three cases where the aerodynamic analysis, assuming steady-state conditions in a free airflow, is open to considerable question.

ACKNOWLEDGMENT

This paper and the preceding one[5] are a development of the more important parts of a doctoral thesis written at the Massachusetts Institute of Technology in the spring of 1948.[13] Publication has been considerably delayed in the hope that a typical set of curves, as in Fig. 1, could be calculated, but it has not yet been possible to carry through this project.

The thesis was based on work done for Hamilton Standard Propellers in the years 1946–1948, and the author wishes to express his gratitude to Charles M. Kearns of that organization both for permission to use this material and for his helpful counsel and guidance. Several people have been associated with the computations involved, of whom the principals are Seymour Parsons, of Hamilton, and Dr. George R. Stibitz, of the University of Vermont.

So many of the ideas of this paper are due to collaboration between the author and Walter E. Arnoldi, of Hamilton, that it is impossible to mention every one, but the author would like to express his extreme gratitude to Mr. Arnoldi, since without his aid the above analysis would not have been completed.

REFERENCES

[1] White, W. T., *Integral Equations for Vibrating Beams*, Jour. Frank. Inst., Vol. 245, pp. 25 and 117, January and February, 1948.

[2] Southwell, R. V., *Theory of Elasticity*, para. 521–3; Oxford Press, London, 1941.

[3] Myklestad, N. O., *Vibration Analysis*, Sec. VI-3; McGraw-Hill Book Company, Inc., New York, 1944.

[4] Dunholter, R. J., *Static Displacement and Coupled Frequency of a Twisted Bar*, Journal of the Aeronautical Sciences, Vol. 13, No. 4, p. 214, April, 1946.

[5] Plunkett, R., *Propeller Blade Moments and Deflections*, Jour. Appl. Mech., p. 361, December, 1949.

[6] Den Hartog, J. P., *Mechanical Vibrations*, 3rd. Ed., Sect. 53; McGraw-Hill Book Company, Inc., New York, 1947.

[7] Sutherland, R. L., *Bending Vibration of a Rotating Blade*, Jour. Appl. Mech., p. 361, December, 1949.

[8] Thomson, W. T., *Mechanical Vibrations*, p. 63; Prentice-Hall, New York, 1948.

[9] Kincaid, W. M., *Finding the Roots of Matrices*, Quart. of Appl. Math., p. 320, October, 1947.

[10] Frazer, R. A., Duncan, W. J., and Collar, A. R., *Elementary Matrices;* Cambridge Press, 1938.

[11] Flomenhoft, H. I., *Frequencies Above the Fundamental by Iteration*, Jour. Appl. Mech., p. 249, September, 1950.

[12] Arnoldi, W. E., Hamilton Standard Propellers, Report No. HSP-613, Project No. 709, 203, December, 1947.

[13] Plunkett, R., *Forced Vibrations of a Rotating Propeller*, ScD. Thesis, M.I.T., June, 1948.

[14] Plunkett, R., *On the Convergence of Matrix Iteration Processes*, Quart. Appl. Math., Vol. VII, No. 4, January, 1950.

Changes of Address

Since the Post Office Department does not as a rule forward magazines to forwarding addresses, it is important that the Institute be notified of changes in address 30 days in advance of publishing date to ensure receipt of every issue of the JOURNAL and REVIEW.

Notices should be sent directly to:

Institute of the Aeronautical Sciences, Inc.
2 East 64th Street, New York 21, New York

Readers' Forum

BRIEF REPORTS of investigations in the aeronautical sciences and discussions of papers published in the JOURNAL are presented in this special department. The publication will be completed approximately 8 to 10 weeks after receipt of the material. The Editorial Committee does not hold itself responsible for the opinions expressed by the correspondents. Contributions should not exceed 800 words in length.

On the Theory of Heat Transfer Through a Laminar Boundary Layer

Arthur N. Tifford
Department of Aeronautical Engineering, The Ohio State University, Columbus
January 9, 1951

Introduction

WE HAVE BEEN VERY MUCH INTERESTED in M. J. Lighthill's recent paper,[1] because of its close connection with some of the work supported here at The Ohio State University by the Office of Air Research of the Air Materiel Command, U.S.A.F. The present note is concerned with a relatively simple alteration of a portion of the analysis bringing about remarkable agreement with more exact analyses of the rate of heat transfer in the presence of a surface pressure gradient.

By way of review: in the analysis referenced, Lighthill assumes, in addition to the usual assumptions, a linear velocity profile, $u = [\tau_0(x)/\mu]y$. After an interesting application of operational calculus, he arrives at the following:

$$Q_0(x) = -k\left(\frac{\rho}{9\mu^2}\right)^{1/3} \frac{\sqrt{\sigma\tau_0(x)}}{(1/3)!} \times \int_0^x \left[\int_{x_1}^x \sqrt{\sigma\tau_0(z)}\, dz\right]^{-1/3} dT_0(x_1) \quad (29)$$

and

$$\int_0^l Q_0(x)\, dx = -\frac{k/2}{(1/3)!}\left(\frac{3\rho}{\mu^2}\right)^{1/3} \times \int_0^l \left[\int_x^l \sqrt{\sigma\tau_0(z)}\, dz\right]^{2/3} dT_0(x) \quad (30)$$

which simplifies, for isothermal surfaces, to

$$\frac{hl}{k} = 0.807\left(\frac{\rho}{\mu^2}\right)^{1/3}\left[\int_0^l \sqrt{\sigma\tau_0(x)}\, dx\right]^{2/3} \quad (34)$$

The comparison of the results obtained by means of Eq. (34) in the case of isothermal wedges, with the values determined by detailed numerical integration of the differential equations, has been given in his Table I for $\sigma = 0.7$.

Analysis

The error percentages shown in Table I arise from two distinct sources: the distortions of the boundary-layer temperature field close to the surface caused by (1) the presence of a surface pressure gradient and (2) the neglected boundary-layer velocity profile at some distance from the surface. Both distortions may be expected to vary with the Prandtl Number.

The larger discrepancies tabulated are primarily caused by the presence of a surface pressure gradient. We shall therefore first try to include its effect in the analysis.

The velocity profile in any laminar boundary layer is given by Eq. (1),

$$u = \frac{\tau_0}{\mu}y + \frac{dp}{dx}\frac{y^2}{2\mu} + \frac{\rho}{\mu^3}\tau_0\frac{d\tau_0}{dx}y^4 + \ldots \quad (1)$$

To accomplish our purpose, we must retain the second, as well as the first, term of the infinite series in the approximate representation of the velocity profile. Unfortunately, however, the analysis under these circumstances is extremely difficult, except in the case of the flat plate—i.e., $dp/dx = 0$—and in the case of the separating boundary layer—i.e., $\tau_0 = 0$. For the present, therefore, let us seek an effective distance, δ, which will convert the parabolic velocity profile into the particular linear velocity profile having the same rate of heat transfer.

$$\text{effective } u = (y/\mu)[\tau_0 + (dp/dx)\delta] \quad (2)$$

The effective distance is found to be approximately four-thirds of the momentum thickness of the boundary layer [$\delta = (4/3)\delta^{**}$].

As matters stand at this point, the rate of heat transfer would be proportional to $\sigma^{1/3}$ regardless of the pressure gradient. However, as has been shown in reference 2, although a one-third power law is appropriate to a linear boundary-layer velocity profile, a one-fourth power law is appropriate to a y^2 velocity profile. In order to cover all cases, the product, $\sigma\tau_0$, should be replaced throughout Lighthill's results by its effective value given by Eq. (3).

$$\text{effective } (\sigma\tau_0) = \text{actual } (\sigma\tau_0) + (4/3)\delta^{**}(dp/dx)\sigma^{3/4} \quad (3)$$

As for the second source of error, it has been found that in both the case of the flat plate and the case of the separating boundary layer,† percentage errors of +3 per cent ($\sigma = 0.7$) are caused. This error may be separated into two parts—namely, a +2 per cent error occurring when the Prandtl Number is unity and a slight Prandtl Number correction associated with the magnitude of the Prandtl Numbers of gases (their values lie between 0.5 and 2). The error may be eliminated by multiplying the results obtained after use of Eq. (3) by the factor, $0.98\sigma^{0.02}$.

Table II shows the result of the application of the revised analysis to the isothermal wedges considered in Table I.

As can be seen, almost exact agreement with the "correct" values is obtained. Table III demonstrates that this agreement extends to the full range of Prandtl Numbers associated with gases in the two cases in the literature[2] in which the Prandtl Number effect has been studied in detail.

† Analyzed by Research Associate, John Wolansky.

TABLE I. $(hl/k)(\nu/u_1 l)^{1/2}$

m	−0.0904	−0.0654	0	1/9	1/3	1	4
Lighthill's values	0	0.497	0.601	0.648	0.653	0.587	0.398
"Correct" values	0.438	0.541	0.585	0.596	0.576	0.495	0.325
Error, per cent	−100	−8	+3	+9	+13	+18½	+22½

TABLE II. $(hl/k)(\nu/u_1 l)^{1/2}$. [$\sigma = 0.7$]

m	−0.0904	−0.0654	0	1/9	1/3	1	4
Values from revised analysis	0.437	0.548	0.585	0.591	0.571	0.495	0.329
"Correct" values	0.438	0.541	0.585	0.596	0.576	0.495	0.325
Error, per cent	−0.2	+1.3	0	−0.8	−0.8	0	+1.3

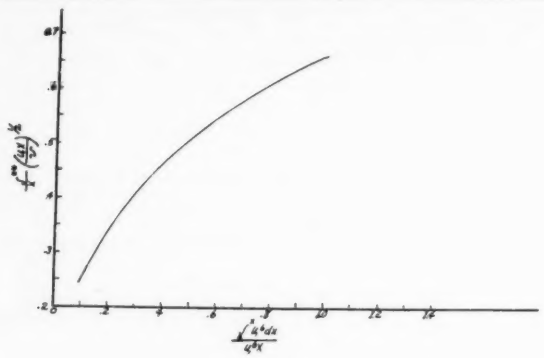

FIG. 1.

TABLE III. $(hl/k)(\nu/u_1 l)^{1/2}$

	Flat Plate		Forward Stagnation Region	
σ	Values from revised analysis	Pohlhausen's values	Values from revised analysis	Squire's values
0.6	0.554	0.552	0.466	0.466
0.7	0.585	0.585	0.495	0.495
0.8	0.613	0.614	0.522	0.521
0.9	0.639	0.640	0.547	0.546
1.0	0.664	0.664	0.570	0.570
1.1	0.686	0.687	0.592	0.592

It is recommended that the revised analysis presented here be put to general use. To facilitate its application, attention is called to the graph of Fig. 1, developed by Falkner in reference 4. This curve enables one to readily determine the approximate momentum thickness of the laminar boundary layer at any point.

SYMBOLS

- h = average heat transfer coefficient
- k = thermal conductivity of fluid
- l = total distance along surface from forward stagnation point
- m = constant exponent ($u_1 \alpha x^m$)
- p = static pressure
- Q_0 = local rate of heat transfer per unit area at the surface
- T_0 = local temperature difference between the wall and the local free stream
- u = fluid velocity along surface
- u_1 = local free stream fluid velocity along surface
- x = distance along surface
- y = distance perpendicular to surface
- z = dummy variable
- δ = effective distance
- δ^{**} = momentum thickness of boundary layer
- μ = absolute viscosity of fluid
- ν = kinematic viscosity of fluid
- ρ = density of fluid
- σ = Prandtl Number of fluid
- τ_0 = local surface shearing stress

REFERENCES

[1] Lighthill, M. J., *Contributions to the Theory of Heat Transfer Through a Laminar Boundary Layer*, Proceedings of the Royal Society, Series A, Vol. 202, No. 1070, pp. 359–377, August, 1950.

[2] Tifford, A. N., *Some Prandtl Number Effects on the Transfer of Heat*, Sixth International Congress for Applied Mechanics, Paris, 1946. (See Engineering Experiment Station News, The Ohio State University, Vol. XXII, No. 1, pp. 11, 12, 30–34, February, 1950.)

[3] Goldstein, S., et al., *Modern Developments in Fluid Dynamics;* Oxford University Press, 1938.

[4] Falkner, V. M., *Simplified Calculation of the Laminar Boundary Layer*, British Air Ministry, R. & M. 1895, July, 1941.

Calculation of Deflections in Indeterminate Structures

H. F. Michielsen

Chief of Structural Research, Royal Aircraft Factory Fokker, Amsterdam, Nederland

February 1, 1951

READING OF THE CONSIDERATIONS from Boley and Moore (Readers' Forum, JOURNAL OF THE AERONAUTICAL SCIENCES, Vol. 17, No. 8, p. 526, August, 1950) and from Cox and Sopwith (Readers' Forum, JOURNAL OF THE AERONAUTICAL SCIENCES, Vol. 17, No. 12, p. 815, December, 1950) gives rise to the impression that there must be some confusion regarding the essential features of both procedures under consideration. It is hoped that the following developments may somewhat clarify the situation.

The internal loads L (stresses, bending moments, etc.) acting on the elements of a structure, can be written

$$L = L_0 + FL_F \tag{1}$$

where L_0 balances the known external loads, L_F is self-equilibrating (without external loads), and F is a statically indeterminate factor. If dS denotes the inverse stiffness of a structural element, F can be determined from Castigliano's Theorem of Least Work, yielding

$$(\partial/\partial F) \int (L^2/2) dS = 0 \tag{2}$$

hence

$$\int LL_F \, dS = \int L_0 L_F \, dS + F \int L_F^2 \, dS = 0 \tag{3}$$

From Eq. (3) the redundant quantity F is determined.

Now, if the component of the deflection at a given point in a given direction is to be determined, the dummy load $P' = 1$ is assumed to work in that point and in that direction. The dummy load would yield internal loads

$$L' = L_0' + F'L_F \tag{4}$$

where again

$$\int L_0' L_F \, dS + F' \int L_F^2 \, dS = 0 \tag{5}$$

Making use of the principle of virtual displacements, the deflection δ is then calculated from

$$\delta = \int LL' \, dS \tag{6}$$

The purpose of the note of Boley and Moore now seems to be to draw attention to the fact that Eq. (6) can be written as

$$\delta = \int LL_0' \, dS \tag{7}$$

which equation obviates the computation of F' from Eq. (5) and the determination of the integrals $\int LL' \, dS$, as far as structural elements not stressed by L_0' are concerned. Especially in the case of highly redundant and complicated structures (for instance, wings and fuselages), this seems to be an extremely important advantage. The load L_0' can be chosen in any suitable way (involving the least number of elements) able to equilibrate the dummy load.

Eq. (7) can be derived from Eq. (6), making use of the consideration that, according to Eq. (4) and the outer members of Eq. (3),

$$\int LL' \, dS - \int LL_0' \, dS = F' \int LL_F \, dS = 0 \tag{8}$$

In exactly the same way it can be proved that

$$\delta = \int L_0 L' \, dS \tag{9}$$

which equation obviates the computation of F from Eq. (3) and can be important if, in a structure of known cross-sectional dimensions, the deflection in a single point at several different loadings L_0 is to be determined.

Cox and Sopwith, on the other hand, set up the general expression for the strain energy U, which can be written, with the notations used here,

$$2U = \int L_0^2\,dS + 2P'\int L_0L_0'\,dS + 2F\int L_0L_F\,dS + P'^2\int L_0'^2\,dS + 2P'F\int L_0'L_F\,dS + F^2\int L_F^2\,dS \quad (10)$$

Equating $\partial U/\partial F$ to zero with $P' = 0$ leads to

$$\int L_0L_F\,dS + F\int L_F^2\,dS = 0 \quad (11)$$

in accordance with Eq. (3).

The deflection is then determined from $\delta = \partial U/\partial P'$, with $P' = 0$,

$$\delta = \int L_0L_0'\,dS + F\int L_0'L_F\,dS \quad (12)$$

and, because of Eq. (1), Eqs. (12) and (7) are identical. Nevertheless, Eq. (7) seems to be preferable to Eq. (12) for practical computation. Its form is extremely simple and easy to keep in mind, and it attacks more directly the problem involved—for instance, if stresses are known but no complete analysis is available.

Unfortunately Messrs. Cox and Sopwith do not mention the texts in which the procedure, outlined in their note, can be found. Some well-known textbooks deal with deflections of determinate structures and analysis of redundant structures but without drawing special attention to deflection of redundant structures.

Although the method, described by Messrs. Boley and Moore, has been practiced in our stress offices for many years, our experience is that, in its simple form as expressed in Eqs. (7) and (9), it is not as well known as it ought to be. We therefore certainly agree with the purport of the first paragraph of their note.

The Calculation of Deflections of Indeterminate Structures

Bruno A. Boley and Roland H. Moore
The Ohio State University, Columbus, and Goodyear Aircraft Corporation, Akron, Respectively
January 30, 1951

A METHOD OF CALCULATING DEFLECTIONS of indeterminate structures was recently discussed in reference 1; some questions on it have been brought up by H. L. Cox and D. G. Sopwith in reference 2. The treatment of reference 2 differs from that of reference 1 principally in that it makes use of Castigliano's theorem rather than of the principle of virtual displacements. For any linearly elastic structure, the two methods are equivalent; the main difference is one of procedure. When Castigliano's theorem is used, it is customary to include the dummy loads with the actual loading and the redundant quantities at the outset in calculating the strain energy U; the desired deflection is then the partial derivative of U with respect to the appropriate load. When the principle of virtual displacements is employed, the redundant quantities are first evaluated in terms of the actual loading; then, as a separate step, the dummy system is applied to the structure, the internal stresses due to it are found, and the deflection is obtained by the equation of reference 1.

It was stated in reference 1 that in the calculation of the internal stresses due to the dummy load, it is permissible to disregard the redundant members of the structure. This simplification is used automatically when the calculations are performed by Castigliano's theorem (because of the use of the partial derivative); not so when the principle of virtual displacements is applied as discussed above. The latter procedure is more commonly used in the United States, and for this reason a special mention of the subject was thought desirable. It might be mentioned that, if, in using the Castigliano's theorem approach, the calculations were (for convenience) to be split in two parts, in the second part (which would consist of evaluating the total energy stored due to the action of the dummy loads) the redundant members could again be neglected.

The authors appreciate the criticisms of Messrs. Cox and Sopwith. They also wish to acknowledge the comments of G. A. Starr, of Chance Vought Aircraft, who stated that reference 3 contains applications (related to beam problems) of the simplification here considered, and the remarks of Dr. N. J. Hoff, of the Polytechnic Institute of Brooklyn, who indicated that the present procedure appears in his mimeographed notes, soon to be published under the title of *Minimal Principles of Structural Analysis*.

REFERENCES

[1] Boley, Bruno A., and Moore, Roland H., *Note on the Calculation of Deflections of Indeterminate Structures*, Readers' Forum, Journal of the Aeronautical Sciences, Vol. 17, No. 8, p. 526, August, 1950.

[2] Cox, H. L., and Sopwith, D. G., *Determination of Deflections in Redundant Structures*, Readers' Forum, Journal of the Aeronautical Sciences, Vol. 17, No. 12, p. 815, December, 1950.

[3] Van den Brock, J. A., *Elastic Energy Theory*, 2nd Ed., p. 67; John Wiley & Sons, Inc., New York, 1942.

On Plastic Buckling of Plates and a Theory of Plastic Slip

P. Cicala
Instituto Aerotécnico and University of Córdoba, Argentina
January 8, 1951

IN A READER'S FORUM NOTE (JOURNAL OF THE AERONAUTICAL SCIENCES, Vol. 17, No. 6, p. 378, June, 1950), the writer showed that the predictions of a flow theory of plasticity can agree with test results on buckling of a compressed sheet if certain initial eccentricities are supposed to exist in the test specimens. In an interesting discussion (JOURNAL OF THE AERONAUTICAL SCIENCES, Vol. 17, No. 11, p. 742, November, 1950), Professor Bijlaard argued that these eccentricities are relatively large and that the tested sheets probably do not show such a degree of irregularity. If this is the case, their low buckling loads give experimental evidence against the Prandtl-Reuss theory. As other tests are in conflict with deformation theory, it may be inferred that neither theory can be confidently used in the analysis of plasticity problems involving marked changes in the direction of the stress tensor. On the contrary, a new "plastic slip" theory[1] appears to agree with known test results. Some conclusions deduced[2, 3] from this analytically rather complex theory are presented here.

If a state of uniaxial stress $\sigma_z = \sigma > \sigma_p$ (x, y, z orthogonal axes, σ_p proportional limit) is reached through a continued increase of only this component and, subsequently, a small change $\delta\Sigma$ in the stress tensor is produced, the following cases are to be distinguished:

(a) If $\delta\Sigma$ contains a sufficiently large increment $\delta\sigma$ of σ_z, the strain increments are related to the stress increments by equations of the same form as for previous theories. The coefficients appearing in these equations depend only upon the initial stress σ; it was shown[2] that they can be deduced from the simple tension test without requiring the calculation of the characteristic function F, which in this theory represents the unit plastic slip. For instance, denoting by $1/E_z$ the coefficient of $\delta\sigma_z$ in the expression of the strain increment $\delta\epsilon_z$, we find

$$1/E_z = (3/8E_i) + (1/4E_s) + (3/8\sigma)\int_0^\sigma d\sigma/E_s \quad (1)$$

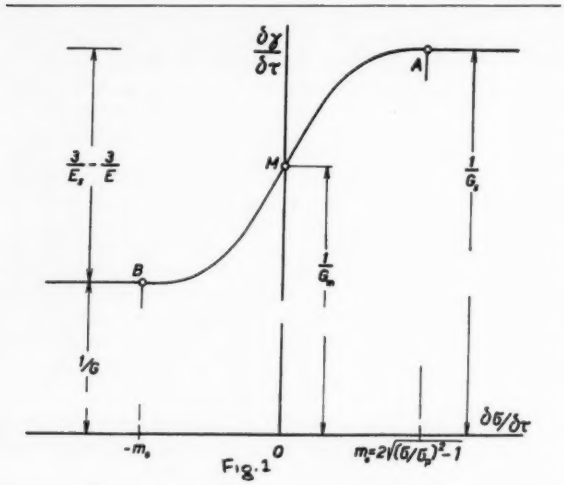

Fig. 1

where E_t and E_s are the tangent and secant moduli. If only the components σ_x and σ_z are incremented, Eq. (1) holds when $\delta\sigma/\delta\sigma_x > \sigma/\sigma_p$ if $\delta\sigma_x$ has the same sign as $\delta\sigma$ and σ or when $-\delta\sigma \div \delta\sigma_x > (\sigma/\sigma_p) - 1$ if $\delta\sigma_x$ has the opposite sign.

(b) If $\delta\Sigma$ contains a sufficiently large decrease of σ_s, all plastic strain components disappear.

(c) If $\delta\sigma$ lies between certain limits, the coefficients of the mentioned equations depend not only on the initial stress σ but also upon the ratios of stress increments; their calculation implies the function F, whereas the limiting values do not depend on F. Reversing all the signs of the stress increments which correspond to a limiting configuration between cases (a) and (c) leads to a limiting configuration between cases (b) and (c).

In the particular case that only a tangential stress $\delta\tau$ in a plane perpendicular to z is introduced, the relation between $\delta\sigma$, $\delta\tau$ and the corresponding shear strain $\delta\gamma$ may be summarized in a graph (see Fig. 1). The horizontal lines through A and B correspond to conditions (a) and (b), respectively. The curve AMB was obtained for $\sigma = 1.25\sigma_p$, assuming for F the simplest linear expression.

The buckling of a strip of thickness s, width b, length $L \gg b$, with one of its long sides free and the other simply supported, subjected to longitudinal compression σ, may be analyzed according to the above results. The case of vanishing initial eccentricities is considered. We suppose that the values of the incremental ratios (Fig. 1) calculated for the conditions at onset of buckling can be used to represent the corresponding derivatives during the whole buckling process. Suppose that the ratio τ/γ takes the same values for all the points of a transversal section; then we obtain[3]

$$\left.\begin{aligned} \sigma &= (s^2v/b^2u)\int_0^u v\,du \\ \gamma &= (su/b)^2 - \sigma(u/v)^2 \end{aligned}\right\} \qquad (2)$$

where $u = \sqrt{d\tau/d\sigma}$ and $v = \sqrt{d\tau/d\gamma}$. By means of the diagram in Fig. 1, v can be deduced as a function of u, and, thus, from Eqs. (2), the relationship between the axial load and the strain γ (which we may measure at the most stressed fiber) is obtained in a parametrical form.

For a given σ, Eqs. (2) yield the same value of γ and, hence, of the unit twist, for any section. Thus, neglecting the bending and warping stresses leads to a triangular variation of the angle of twist, the maximum being attained halfway between the supported end sections.

With fair accuracy, for $u \geq u_0$, we may write

$$v/\sqrt{G_s} = 1 + k\,(u^2 - u_0^2)^n u^{-2n} \qquad (3)$$

where $u_0 = 1/\sqrt{m_0}$ is the value corresponding to point A, G_s and G_m are the moduli defined in Fig. 1, n is a positive integer that may be given the value $n = 3$, and $k = \sqrt{G_m/G_s} - 1$.

With Eq. (3) and $v = \sqrt{G_s}$ for $u < u_0$, Eqs. (2) can be readily evaluated. For small values of γ, the solution may be expressed in the form

$$\sigma/\sigma_s = 1 + (\gamma b^2/s^2u_0^2) - [kn/(n+1)]\,(\gamma b^2/ks^2u_0^2)^{(n+1)/n} + \text{higher powers of } \gamma$$

where $\sigma_s = G_s s^2/b^2$ is the stress at which buckling starts, coinciding with the known critical stress deduced on the basis of deformation theories of plasticity.

By increasing γ, the stress σ tends to the value $G_m s^2/b^2$, which, here, takes the same role as the reduced modulus stress in column buckling.

The approximation may be improved by taking into account the variation of τ/γ over the section. Denoting, as before, by γ the maximum shear strain and by defining τ as the ratio of the twisting moment to $bs^2/3$, Eqs. (2) hold unchanged, whereas a new relation $v(u)$ must be found. According to calculations carried out for $s \ll b$ and $k \ll 1$, the same Eq. (3) with $n = 4$ may be used with sufficient accuracy.

The above results evidently need experimental checks. If differential relations between twist, torque, and axial load similar to the one between γ, τ, and σ plotted in Fig. 1 are obtained experimentally, the torsional buckling in the elastoplastic range can be described by the above equations in cases where the effect of warping stresses is negligible.

The solution presented, though roughly approximate, gives a qualitative outlook of the buckling process of plates, evidencing its analogy to the Shanley phenomenon.

References

[1] Batdorf, S. B., and Budiansky, B., *A Mathematical Theory of Plasticity Based on the Concept of Slip*, N.A.C.A. T.N. No. 1871, 1949.

[2] Cicala, P., *Sobre la teoría de Batdorf y Budiansky de la deformación plástica*, Revista de la Universidad de Córdoba, Año XIII, No. 2, 1950.

[3] Cicala, P., *Sul carico critico di una piastra compressa oltre il limite elastico*, Rendic. Acc. Lincei, Serie VIII, Vol. IX, Fasc. 1–2, July, 1950.

The Effect of Prandtl Number on the Theoretical Shock-Wave Thickness

Paul A. Libby
Assistant Professor of Aeronautical Engineering, Polytechnic Institute of Brooklyn
January 10, 1951

In reference 1, L. Meyerhoff has presented the results of an extensive investigation of the theoretical structure of a one-dimensional shock wave according to the usual hydrodynamic approximations. Among other interesting results he has indicated that, as the Prandtl Number (N_{Pr}) is changed from 0.75 to 0.657 in the equations for constant gas properties [Eq. (8) or (8c) of reference 1], the shock-wave thickness is considerably increased. Since for air, the N_{Pr} is indeed somewhat less than $^3/_4$, this result would indicate that the hydrodynamic equations might describe the structure of a shock wave in air with more accuracy than is usually attributed to them on the basis of Becker's exact solution for $N_{Pr} = {}^3/_4$. However, this accuracy is usually gaged by comparing the shock-wave thickness as defined by Prandtl or by Taylor and Maccoll with the mean free path of the gas molecules. The comparison in reference 1 between the structure with $N_{Pr} = 0.657$ and $N_{Pr} = {}^3/_4$ has been made with different conditions upstream of the wave and, therefore, with different mean free paths. It is of interest, therefore, to replot Fig. 2 of reference 1 in terms of the mean free path of the gas molecules.

For convenience, the mean free path of the gas molecules far ahead of the wave is used as the reference mean free path. For the initial conditions given in Fig. 2 of reference 1, one finds, for the $N_{Pr} = 0.657$ solution, in the usual notation

$$\left.\begin{aligned} \rho_0 &= 0.457 \times 10^{-3}\ \text{Gm./cm.}^3 \\ T_0 &= 500°\text{C.} \\ \mu_0 &= 3.56 \times 10^{-4}\ \text{Gm./cm.-sec.}^* \end{aligned}\right\} \quad (1)$$

where the subscript zero denotes conditions far ahead of the wave. The mean free path λ is defined by the equation

$$\lambda = \mu/\delta\rho\bar{c} \quad (2)$$

where δ = a constant depending on the accuracy of the theoretical analysis ($1/3 \leq \delta \leq 0.499$) (the value 0.35 due to Tait is used here) and where $\bar{c}$ = mean molecular velocity, $\sqrt{(8/\pi)RT}$.

From the values given in Eq. (1),

$$\lambda_0 = 2.96 \times 10^{-5}\ \text{cm.} \quad (3)$$

For the Becker solution ($N_{Pr} = 3/4$) as shown in Fig. 2 of reference 1, one finds that

$$\left.\begin{aligned} \rho_0 &= 0.752 \times 10^{-3}\ \text{Gm./cm.}^3 \\ T_0 &= 0°\text{C.} \\ \mu_0 &= 1.72 \times 10^{-4}\ \text{Gm./cm.-sec.}^* \end{aligned}\right\} \quad (4)$$

and that

$$\lambda_0 = 1.46 \times 10^{-5}\ \text{cm.} \quad (5)$$

If the two curves are plotted in terms of $\xi = x/\lambda_0$, one obtains the result shown in Fig. 1 herein. It will be seen that, except for the region downstream of the wave where the computational instability discussed by Meyerhoff causes his numerical solution to deviate from the Rankine-Hugoniot asymptote, the computed points fall on a single curve. From this result (which, of course, could not be obtained without the solution for $N_{Pr} = 0.657$), it may be concluded: (1) that the increase in shock-wave thickness with N_{Pr} shown in reference 1 is really due to the change in initial conditions; (2) that the analyses based on $N_{Pr} = 3/4$ are valid for other values of N_{Pr} of interest for air; and (3) that the doubts that arise concerning the accuracy of the hydrodynamic equations for the description of the structure of a shock wave at high Mach Numbers and which are based on the exact analysis with $N_{Pr} = 3/4$ should be considered to remain for the actual N_{Pr} values exhibited by air. The discussion here is based on the solution for constant gas properties, but it can be expected to apply for the case of variable gas properties, variable N_{Pr}, as well.

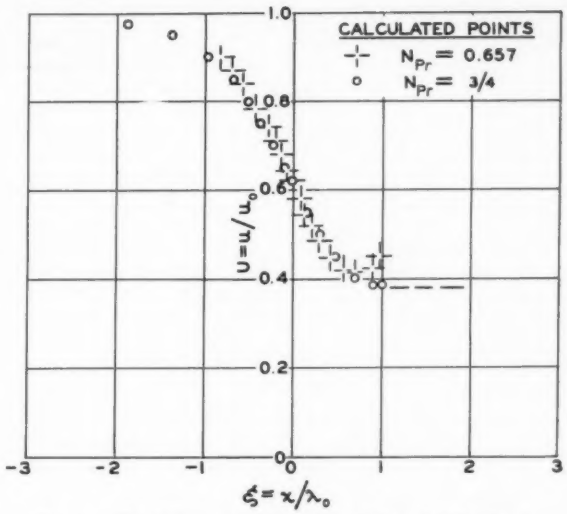

FIG. 1. Shock-wave structure for two Prandtl Numbers.

* The values of μ have been taken from the source listed in reference 1.

REFERENCE

[1] Meyerhoff, L., *An Extension of the Theory of the One-Dimensional Shock-Wave Structure*, Journal of the Aeronautical Sciences, Vol. 17, No. 12, p. 775, December, 1950.

Services of the Libraries of the Institute of the Aeronautical Sciences

The services of the Libraries are available to all members of the Institute, to Corporate Members, to advertisers in the AERONAUTICAL ENGINEERING REVIEW and AERONAUTICAL ENGINEERING CATALOG, and, under usual library limitations, to the public. Four specialized services are available.

The Paul Kollsman Lending Library

This lending library service makes available, *without charge*, the latest and more important aeronautical books.

Members may request the loan of any aeronautical or technical book they wish to borrow. Through an exchange agreement with the Engineering Societies Library, any book on general engineering may be borrowed from its great collection of over 160,000 volumes.

A photostating service is available at usual library rates.

Applications for membership in the library and further information will be sent on request.

The W. A. M. Burden Reference Library

This reference library contains over 12,000 aeronautical books, magazines, pamphlets, and reports gathered from world-wide sources and is one of the most complete aeronautical libraries in the world. Material from this library is not available for loan but may be used for reference purposes.

The Pacific Aeronautical Library

7660 Beverly Boulevard
Los Angeles 36, California

Established in cooperation with the aircraft companies the library serves. The leading aircraft companies in or near Los Angeles participate in its support and operation.

This service library for aeronautical research is available to the public for reading privileges. Source material includes aerodynamic and structural research reports, as well as books on drafting, production methods, history, and allied sciences. It furnishes books, periodicals, and pamphlet material to the participating aircraft companies to supplement their engineering libraries.

Technical Information Service

This service has experienced personnel under the supervision of trained aeronautical engineers to compile any information desired. The services range from listing specialized reference books to the preparation of exhaustive bibliographies, digesting of reports, and general surveys of any aeronautical subject. Some of the available services are:

Bibliographies on any aeronautical subject.
Reports on any aeronautical subject.
Digests of aeronautical books, papers, periodicals, and references.
Translations.
Engineering investigations of special aeronautical subjects.
Biographies of individuals engaged in aeronautics.
Photostats of any aeronautical or general engineering material.
Microfilms made on special order.
Photographs made from the Institute's photographic collection.
Drawings and tracings made.

In addition to the services mentioned any commission which comes within the scope of the Service will be accepted. Special arrangements may be made for work requiring several weeks or months.

Translators are available for accurate transcriptions of all foreign language data. Translations are carefully edited by trained engineers.

Reproductions of any material in the collections of the Institute may be ordered at standard photostat rates.

INSTITUTE OF THE AERONAUTICAL SCIENCES, INC.
2 EAST 64th STREET, NEW YORK 21, N.Y.